



UNIVERSITÀ DI NAPOLI "FEDERICO II"
SCUOLA POLITECNICA E DELLE SCIENZE DI BASE

Dipartimento di Ingegneria Industriale

Doctorate in Industrial Engineering, XXXII Cycle
PhD Dissertation

**Combined numerical and experimental investigation
on the interaction of synthetic jets and crossflow**

Andrea Palumbo

Supervisors

Prof. Luigi DE LUCA

Dr. Matteo CHIATTO

Coordinator

Prof. Michele GRASSI

JANUARY 2020

Contact information:

Andrea Palumbo

Università di Napoli “Federico II”

Dipartimento di Ingegneria Industriale

P.le Tecchio 80, 80125, Napoli

Italy

email: andrea.palumbo@unina.it

Abstract

The fluid dynamics research has been recently focused on the development of passive and active flow control technologies for drag reduction. As a matter of fact, the aerodynamic drag generated by the airplane has been widely recognized as one of the most significant causes of its high environmental impact. Therefore, a great effort has been paid in minimizing the pollutant emissions produced by civil transport aircrafts during the last decades. In particular, a huge number of numerical and experimental investigations has been made, to properly understand the effect of such techniques on laminar/turbulent transition and separation control on the lifting surfaces of the airplanes (mainly wings and tails).

Among other techniques, synthetic jet (SJ) actuators overwhelmingly came out in the last years, due to their simplicity, wide velocity and frequency ranges and low weights. The application of a synthetic jet to control an incoming crossflow has been widely investigated in the last twenty years, often relying on database information of the crossflow frequency spectra and/or trial-and-error techniques for the optimized design of the actuator. The present thesis concerns the application of a SJ actuator in a boundary layer, a mandatory step to build a stability-based framework for the design of the actuator. It is worth noting that the present work has been carried out with special reference to piezo-driven and plasma synthetic jet actuators, but in principle the results can be extended to other types of active flow control techniques.

The objective of the current research has been to innovate the procedure for the optimized implementation of synthetic jet actuators in crossflow conditions. For this reason, during the doctoral period each step of the design workflow, from the device manufacturing and characterization in quiescent conditions up to its operation, has been critically examined.

The main original results of the work are listed below:

- Experimental and numerical investigations on the flow field generated by unconventional actuators in a quiescent environment have been carried out. These actuators are characterized by more cavities and/or orifices, and are generally preferred to the baseline configuration in many engineering situations. A deep understanding of the external velocity field created by such devices is necessary to properly calibrate reduced-order models of the actuators.
- The calibration of an existing lumped element model for the prediction of the performances of a plasma synthetic jet actuator has been made. Experimental measurements are used to tune the lumped element model, obtaining a best fit estimation of the total efficiency of the device. A fair agreement between numerical and experimental results has been achieved after the LEM calibration.
- A “design approach” for the realization of single and double-orifice synthetic jets has been developed. The design rules included in this work could be used to distinguish between favorable designs (where the jet is clearly formed and the desired velocity output is obtained) and undesired actuation behaviors. The present approach is derived for SJs in quiescent conditions.
- A series of direct numerical simulations, based on the 2004 Nasa CFD Validation of Synthetic Jets and Turbulent Separation Control, has been carried out, using two popular open-source codes, Nek5000 and OpenFOAM. Results on different mesh resolutions have been compared, in order to gain information about the best computational approach to be used for SJ simulations.
- A stability-based investigation of the receptivity of a laminar boundary layer flow to synthetic jet actuation has been performed via direct numerical simulations. Two boundary layer Reynolds numbers have been considered, whereas the choice of the actuation frequency has been made according to the linear stability analysis. The effect of the freestream turbulence (FST) on the streamwise development of the flow has been also examined. It has been observed that several flow structures, characterized by a varicose symmetry, are created by the jet-crossflow interaction, if no freestream disturbances are added; symmetry-breaking occurs in the far field for moderate values of the FST intensity. The resulting flow field perfectly resembles

the one obtained introducing a small hemispherical roughness element into a laminar boundary layer, thus a low-speed SJ actuator acts like an “user-defined” roughness, whose effect can be optimized using different values of the actuation frequency and applied voltage.

- A novel model for the instability and transition in wall-bounded flows has been developed to understand the role of the critical layer in the stability process. The classic stability analysis is reformulated by means of a pseudo two-fluid model, a central inviscid flow motion and a wall viscous one, forcing each other on their common interface streamline. A fair agreement with the results of the celebrated Orr–Sommerfeld equation is obtained if the interface is located around the elevation of the base flow average value, equal to $2/3$ times the centerline velocity. The present analysis allows to state that two important length scales are responsible of the transition behavior of the flow: indeed, while the mechanism leading to instability is located near the wall in the critical layer region, the central region around the flow average velocity is also deeply involved in the onset of the instability.

Preface

The present doctoral thesis deals with a combined numerical, experimental and theoretical analysis of synthetic jet actuators issuing in quiescent conditions and interacting with boundary layer flows. The research activity has been intended to lay a theoretical foundation for the optimized design of active flow control devices for separation control purposes. Such techniques are becoming increasingly widespread during the last years, taking also advantage from the strong impulse given by recent international workshops and research programs to tackle the climate change. Active flow control techniques are deemed to be particularly attractive for reducing the fuel consumption of the airplanes, owing to their bigger flexibility if compared with passive control systems, which guarantee good performances only in design conditions. Among other systems, synthetic jet actuators have proven to be suitable for this application.

The research activity may be split into two main subjects: design and characterization of actuators in quiescent environment and interaction with an external flow to be controlled. However, this partition is only apparent, since the main objective of the research is to develop and optimize the entire design process of the actuator, from its manufacturing and characterization in quiescent conditions up to its operation, by means of a combined approach. In the first step of the research, therefore, the behaviour of synthetic jets in quiescent conditions has been analyzed. An experimental/theoretical analysis aimed at refining existing lumped-element models for unconventional synthetic jet actuators and developing a novel design approach for the prediction of synthetic jet performances in quiescent conditions. A numerical analysis has been based on the use of two open-source codes for the computation of such flow fields, and includes an exhaustive investigation about the effect of the chosen numerical setup on the accuracy of the simulations. Besides, direct numerical simulations

of unconventional actuators, based on double-orifice actuators, have been carried out. The aim of this work was to characterize the interaction between adjacent jets, in order to fill the gap between practical configurations of the SJ devices and simple devices used for research activities. Finally, a complete characterization of a novel actuator for separation control purposes has been made: a preliminary investigation employed hot-wire measurements and direct numerical simulations in quiescent conditions. The analysis has been subsequently corroborated by a new lumped element model, suited for multi-orifice/multi-cavity configurations.

On the other hand, a second research line focused on the interaction of SJ with a boundary layer crossflow. This subject has been developed during a stage period at the DynFluid Laboratory of the Arts et Metiers ParisTech University, as detailed below. Several direct numerical simulations of synthetic jets in crossflow have been performed. Particular attention has been paid on the transition to turbulence caused by the vortical structures generated by the jet/boundary layer interaction.

The following journal articles arose from the research activities and are discussed within the thesis work:

- A.1** A. PALUMBO, M. CHIATTO, L. DE LUCA. “The role of the critical layer in the channel flow transition revisited”, *Meccanica*. Vol. 54, Issue 14, pp. 2169-2182. 2019.
- A.2** M. CHIATTO, A. PALUMBO, L. DE LUCA. “Design approach to predict synthetic jet formation and resonance amplifications”. *Experimental Thermal and Fluid Science*. Vol. 107, pp. 79-87. 2019.
- A.3** F. CAPUANO, A. PALUMBO, L. DE LUCA. “Comparative study of spectral-element and finite-volume solvers for direct numerical simulation of synthetic jets”. *Computers & Fluids*. Vol. 179, pp. 228-237. 2019.
- A.4** A. PALUMBO, M. CHIATTO, L. DE LUCA. “Measurements versus numerical simulations for slotted synthetic jet actuator”. *Actuators*. Vol. 7. Issue 3, Article No. 59. 2018.
- A.5** M. CHIATTO, A. PALUMBO, L. DE LUCA. “A Calibrated Lumped Element Model for the Prediction of PSJ Actuator Efficiency Performance”. *Actuators*. Vol. 7. Issue 1, Article No. 10. 2018.

Part of the results have been also presented in national and international conferences:

- C.1** A. PALUMBO, O. SEMERARO, J.-CH. ROBINET, L. DE LUCA, *Receptivity to synthetic jet actuation in boundary layer flows*, AIAA SciTech 2020, Orlando, 6-10 January 2020.
- C.2** A. PALUMBO, A. DELLA PIA, M. CHIATTO, L. DE LUCA, *Numerical study on the flow field generated by a double-orifice synthetic jet device*, XXIV AIMETA Conference, Roma, 15-19 September 2019.
- C.3** M. CHIATTO, A. PALUMBO, G. DE FELICE, L. DE LUCA, *Multi-slotted synthetic jet actuator for flow control of separated flows*, 15th International Conference on Fluid Control, Measurements and Visualization, Napoli, 27-30 May 2019.
- C.4** A. PALUMBO, *Global stability analysis of synthetic jet in crossflow*, Giornata dei dottorandi italiani in ingegneria aerospaziale, Pisa, 29-31 October 2018.
- C.5** A. PALUMBO, F. CAPUANO, L. DE LUCA, *Performances of two open-source codes in the numerical simulation of synthetic jets*, ECCOMAS Conference, Glasgow, 11-15 June 2018.
- C.6** M. CHIATTO, M. ARENA, A. PALUMBO, R. PECORA, L. DE LUCA, *Towards a flow control method based on PSJ actuators: a feasibility study*. Euromech Colloquium 593, Delft, 14-16 March 2018.
- C.7** M. CHIATTO, A. PALUMBO, L. DE LUCA. *Piezo-driven and Plasma Synthetic Jet Actuators. A comparative investigation*. Global Workshop on Functional Materials and Devices, Singapore, January 11-13, 2018.
- C.8** M. CHIATTO, A. PALUMBO, L. DE LUCA. *Experimental Characterization of Plasma Synthetic Jet Actuators*. XXIII AIMETA Conference. Salerno, 4-7 September 2017.

In particular, paper [A.3](#) is included in Chapter [2](#), papers [A.2](#) and [A.5](#) are discussed in Chapter [3](#), whereas the journal article [A.4](#) and the conference paper [C.2](#) constitute part of Chapter [4](#). A novel interpretation of the channel flow instability, included in paper [A.1](#), is closely related

to the contents of Chapter 1, therefore a small summary of this work has been made in Appendix A. Finally, the main results shown in the conference paper C.1 are briefly outlined in Chapter 5. Further results in Chapters 4 and 5 are under consideration for publication on peer-reviewed international journals at the time of writing the present thesis (January 2020).

The main supervisor of the project is prof. Luigi de Luca; dr. Matteo Chiatto acts as co-advisor. Part of the work has been developed during a 10-month stage period at the Arts et Metiers ParisTech University, which was funded by Compagnia di San Paolo and University of Naples “Federico II” under the STAR Program STAGES (STAbilità di un GETto Sintetico in crossflow). In particular, a strong contribution to this work have been carried out by prof. Jean-Christophe Robinet from the DynFluid Laboratory of the Arts et Metiers ParisTech University and dr. Onofrio Semeraro the Laboratoire d’Informatique pour la Mécanique et les Sciences de l’Ingénieur (LIMSI) of the CNRS. Finally, it must be acknowledged that the present thesis work took also advantage of the valuable collaboration of many researchers from the Department of Industrial Engineering of the University of Naples and the DynFluid Laboratory. In particular, the author wishes to thank Francesco Capuano, Enrico Maria de Angelis, Alessandro Della Pia, Lorenzo Russo, Fortunato De Rosa and Michele Alessandro Bucci for their help in solving theoretical and numerical issues arisen during the PhD period.

Contents

Abstract	iii
Preface	vi
1 Introduction	1
1.1 International scenario	1
1.2 Separation control techniques	3
1.3 Synthetic jets	8
1.3.1 Dimensionless parameters and data reduction	13
1.4 Towards a rational design of AFC systems	15
1.5 Aim of the work and thesis structure	20
2 Numerical tools for SJ design and characterization	23
2.1 Introduction	24
2.2 The increasing importance of open-source solvers	26
2.3 Low vs High-order numerical methods	29
2.3.1 Computational model	29
2.3.2 Results and conclusions	33
2.3.3 Final remarks	37
3 Experiment-based design of synthetic jets	39
3.1 A calibrated LEM for plasma synthetic jet actuators	39
3.1.1 The lumped element model	40
3.1.2 LEM calibration	43
3.2 LEM-based design approach for piezo-driven SJs	46
3.2.1 Experimental measurements	47
3.2.2 Linking jet formation and LEM results	51
3.3 Obtaining full-field data from LEM output	55

4	Unconventional SJ actuators in quiescent environment	59
4.1	Continuous twin jets: literature review	60
4.2	Double-orifice synthetic jet actuators	63
4.2.1	Numerical setup	64
4.2.2	Effect of orifice spacing	68
4.3	Design and characterization of a multi-slotted SJ actuator .	72
4.3.1	The SJ Device	73
4.3.2	Preliminary characterization	75
4.3.3	Frequency response and lumped element modeling .	82
5	Interaction between synthetic jets and a crossflow	87
5.1	Background and motivation	88
5.2	Numerical simulations	90
5.2.1	Numerical setup	90
5.2.2	Flow parameters	93
5.2.3	Preliminary computations	94
5.3	Analysis of the controlled flow field	95
5.3.1	Baseline case ($Re_{\delta_0^*} = 550, \omega = \omega_{ref}$)	96
5.3.2	Effect of the actuation frequency	99
5.3.3	Effect of the Reynolds number	102
5.3.4	Effect of the inlet turbulence	103
5.4	Implication for flow control	103
6	Conclusions and future work	107
A	Revisitation of critical layer role in channel flow stability	111
	Bibliography	119

List of Figures

- 1.1 Time trends of the number of flights within EU and EFTA countries between 2005 and 2017. Adapted from [1]. 2
- 1.2 Distribution of the total number of flights within EU and EFTA countries between 2005 and 2017. Adapted from [1]. 2
- 1.3 Time-averaged streamwise velocity field \bar{u}/U_1 and streamlines of the interaction between two different streams of velocities U_1 and U_2 , separated by a splitter plate of thickness h , $Re_h = (U_1 + U_2)h/(2\nu) = 600$, $\lambda_m = (U_1 - U_2)/(U_1 + U_2) = 0.2$. The white line $\bar{u} = 0$ is depicted to highlight the recirculation region. 4
- 1.4 Sketch of a piezo-driven synthetic jet device. 9
- 1.5 Near-field evolution of the vortical structures for a slotted SJ in quiescent conditions. (a): $t/T = 0$, (b): $t/T = 0.25$, (c): $t/T = 0.5$, (d): $t/T = 0.75$ 10
- 1.6 Contour map of the phase-averaged velocity and corresponding centerline velocity profile at suction peak. The red point indicates the saddle point position. 11
- 1.7 Schematic view of the operation cycle of a plasma synthetic jet actuator. (a): energy deposition stage; (b): jet discharge; (c): refill. 12
- 1.8 Time evolution of the phase-averaged centerline velocity at the orifice exit during the actuation cycle, for a slotted synthetic jet actuator. The blue area depicts the definition of stroke length L_j 14

1.9	Reproduction of the transition diagram obtained by Von Doenhoff and Braslow [32] for an array of roughness elements. The filled gray area depicts the region of the $d/h - Re_h$ plane where transition to turbulence has been experimentally detected.	15
2.1	Computational domain and boundary conditions used in the numerical simulations. The gray patches are solid walls. An enlarged view of the cavity is shown in the right part of the figure.	31
2.2	Crosswise distribution of time-averaged streamwise (left) and cross-stream (right) velocity at streamwise stations (i) $x/h = 0.5$, (ii) 1.0, (iii) 1.5, (iv) 2.0, (v) 3.0, (vi) 4.0. Lines refer to the Nek5000 (black) and OpenFOAM (red) computations on the coarse (dashed), medium (dashdotted), fine (solid) and very fine (dotted) grid levels; \circ PIV.	33
2.3	Crosswise distribution of phase-averaged streamwise velocity at maximum ejection (left) and maximum ingestion (right) phases at streamwise stations (i) $x/h = 0.5$, (ii) 1.0, (iii) 1.5, (iv) 2.0, (v) 3.0, (vi) 4.0. Lines refer to the Nek5000 (black) and OpenFOAM (red) computations on the coarse (dashed), medium (dashdotted), fine (solid) and very fine (dotted) grid levels; \circ PIV.	34
2.4	Crosswise distribution of streamwise r.m.s. velocity at maximum ejection (left) and maximum ingestion (right) phases at streamwise stations (i) $x/h = 0.5$, (ii) 1.0, (iii) 1.5, (iv) 2.0, (v) 3.0, (vi) 4.0. Lines refer to the Nek5000 (black) and OpenFOAM (red) computations on the coarse (dashed), medium (dashdotted), fine (solid) and very fine (dotted) grid levels; \circ PIV.	35
2.5	Saddle point x_{sp} and stroke length L_j as a function of grid refinement. Triangle is for Nek5000, circle for OpenFOAM.	36
2.6	Computational performances of OpenFOAM and Nek5000. (left) Elapsed CPU time per time step for the three cases of Table 2.3 on 68 processors; (right) elapsed CPU time per time step for the cases OF3 and N3 as a function of the number of processors.	37
3.1	PSJ actuator with the Pitot probe.	44

LIST OF FIGURES

3.2 Jet velocity profiles in the radial direction for different discharged energy. Red markers are the results for $E_d = 1.2$ mJ ($S = 12.36$), blue ones for $E_d = 2.1$ mJ ($S = 11.01$), and black ones for $E_d = 3.4$ mJ ($S = 9.96$). 45

3.3 Mean flow velocity as a function of the discharged energy and the actuation frequencies. Black solid line: $f = 1000$ Hz; blue dotted line: $f = 750$ Hz; red dashed line: $f = 500$ Hz; black dashed-dotted line: $f = 250$ Hz. Star markers represent experimental data. 45

3.4 Frequency response of the brass single-orifice actuator in terms of peak jet velocity at the orifice exit, for different cavity heights. Red cross represents the $H/d = 0.75$ case; blue star $H/d = 1.5$; magenta circle $H/d = 2.25$; green diamond $H/d = 3$; black square $H/d = 3.75$. The blue continuous line is the incompressible solution. 49

3.5 Comparison between the experimental data and LEM for $H/d = 1.5$ and 3.75 cases. The black dashed line and the red cross markers refer to the LEM and the experimental data, respectively, for the $H/d = 1.5$ case. The black continuous line and the red star markers are for $H/d = 3.75$ case. The blue continuous line is the incompressible solution. 50

3.6 Frequency response of the brass single-orifice actuator in the $S - St$ plane, for different cavity heights. Red cross represents the $H/d = 0.75$ case; blue star $H/d = 1.5$; magenta circle $H/d = 2.25$; green diamond $H/d = 3$; black square $H/d = 3.75$. The blue continuous line is the incompressible solution; the black dashed line indicates the formation threshold. 51

3.7 Non-dimensional saddle point position (red star markers) and stroke length (blue circle markers) as a function of the Stokes number. $H/d = 2.25$ case. 52

3.8 Comparison of instantaneous jet velocity experimental data and LEM prediction. The blue markers represent the measurements at the orifice exit, the red ones 1 diameter downstream; the black continuous line is the LEM prediction. $H/d = 3$ case, $f = 500$ Hz. 52

3.9	Frequency response of the brass single-orifice actuator in terms of peak jet velocity one diameter downstream of the orifice exit (red markers), together with the corresponding data at the orifice exit (blue markers); $H/d = 2.25$. The black dashed line indicates the formation boundaries.	53
4.1	Time-averaged streamwise velocity component of a plane continuous twinjet. RANS simulations, $k - \varepsilon$ model (OpenFOAM). Reference case: Lee & Hassan (2018) [97]. $Re = U_0 h / \nu = 4900$, $s_o/h = 2.07$	61
4.2	Description of the nomenclature and symmetry-plane slice of the three-dimensional numerical domain. Actuator walls are depicted in bold.	65
4.3	Comparison between numerical and experimental (circles) streamwise phase-averaged velocity data at the orifice exit plane: coarse grid (dotted), medium grid (dashed), fine grid (solid line).	67
4.4	Distribution of the time-averaged streamwise velocity field in the $x - y$ plane, $s_o/d = 12.5$	67
4.5	Time-averaged flow field, streamwise component \bar{u} , $z = 0$. (a) $s_o/d = 2.5$, (b) $s_o/d = 5$. A white contour line $\bar{u} = 0$ is depicted to highlight the recirculation zones.	68
4.6	(a) Distribution along the x axis of the streamwise component of the time-averaged flow field \bar{u} ; (b) Streamwise location of merging and combined points as a function of the orifice spacing.	70
4.7	Crosswise distributions of time-averaged streamwise velocity at streamwise stations (i) $x/d = 1$, (ii) 2, (iii) 4, (iv) 6, (v) 8, (vi) 10, for $s_o/d = 2.5$ (left) and $s_o/d = 3.75$ (right).	70
4.8	Phase-averaged flow fields, streamwise component $\langle u \rangle$, $z = 0$, $s_o/d = 2.5$ (panels (a)-(d)), $s_o/d = 5$ (panels (e)-(h)), $t/T = 0.25$ (first column), $t/T = 0.5$ (second column), $t/T = 0.75$ (third column), $t/T = 1$ (last column). Only the right orifice is reported, due to the symmetry of the streamwise velocity field.	71
4.9	Isosurfaces of phase-averaged Q-criterion, coloured with the streamwise phase-averaged velocity component $\langle u \rangle$: $s_o/d = 2.5$, $t/T = 0.5$, $Q = 0.05$	72

LIST OF FIGURES

4.10	Actuator bottom (left) and top (right) part views. Courtesy of CIRA.	74
4.11	Definition of the geometrical characteristics of the multi-slotted actuator and description of the reference axes.	75
4.12	Domain and boundary conditions used in the numerical simulations. Only half of the computational domain is represented in the sketch.	76
4.13	Front (left) and side (right) view of the mesh used in the numerical simulation, zoomed near the slot exit plane.	77
4.14	Time variation of the phase-averaged streamwise velocity component at the center of the 2nd slot exit; numerical (solid line), experimental (\bullet).	78
4.15	Phase-averaged streamwise velocity profiles along the spanwise y direction; slot 2, $x/h = 0.2$. (a) expulsion peak ($t/T = 0.25$); (b) suction peak ($t/T = 0.75$); numerical (solid line), experimental (\bullet).	79
4.16	Evolution of the vortical structures in the near-field for the central slots, visualized by $Q = 0.02$ isosurfaces. Ejection phase. The isosurfaces are colored with the phase-averaged streamwise velocity component U/U_0	80
4.17	Evolution of the vortical structures in the near-field for the central slots, visualized by $Q = 0.02$ isosurfaces. Suction phase. The isosurfaces are colored with the phase-averaged streamwise velocity component U/U_0	81
4.18	Saddle point position $x_{sp,i}$, during the suction phase, for different slots: continuous and dotted lines refer to outer slots; dashed and dashdotted lines to inner slots.	82
4.19	Maximum diaphragm displacement as a function of the actuation frequency.	83
4.20	Device frequency response in the $S - L$ plane, based on hot-wire measurements.	84
4.21	Comparison of theoretical LEM (continuous line) and hot-wire measurements (star symbols) frequency responses.	85
5.1	Computational domain and main geometrical parameters of the simulations.	91
5.2	Exponential decay of the turbulent intensity Tu along the streamwise direction. Case S6, $y = 20\delta_0^*$	92

5.3	Comparison between analytical (continuous line) and numerical (open circles) results of the oscillating pipe flow. $Re_j = 220$, $Wo = 26$	95
5.4	Instantaneous distribution of the skin friction coefficient C_f along the streamwise direction in the symmetry plane, SJ off. The laminar (Blasius) solution (dashed lines) and the turbulent correlation $C_f(x) = 0.455/\log^2(0.06Re_x)$ are shown for comparison.	96
5.5	Instantaneous view of the vortical structures, highlighted by $\lambda_2 = -0.1$ isosurfaces, and coloured by the instantaneous streamwise velocity. Case S3, tenth cycle, $t/T = 1$ (end of suction phase).	97
5.6	Visualization of the time-averaged vortical structures in the near field via $\lambda_2 = -0.01$ isosurfaces, coloured with streamwise time-averaged velocity.	98
5.7	Mean streamwise deviation of the controlled flow from the Blasius solution; Case S3, $y/\delta_0^* = 0.8$	98
5.8	Streamwise, time-averaged distributions of the boundary layer integral parameters $\bar{\delta}^*$ (a), $\bar{\theta}$ (b) and \bar{H} (c) in the symmetry plane for Case S3 (continuous line). The laminar solution is depicted with dashed lines for comparison; in (c) also the value $\bar{H} = 1.4$ is shown (dot-dashed line) for reference.	99
5.9	Time-averaged distribution of the skin friction coefficient \bar{C}_f along the streamwise direction in the symmetry plane for Case S3. The laminar (Blasius) solution (dashed line) and the turbulent correlation $\bar{C}_f(x) = 0.455/\log^2(0.06Re_x)$ are shown for comparison.	100
5.10	Instantaneous view of the vortical structures, highlighted by $\lambda_2 = -0.1$ isosurfaces, and coloured by the instantaneous streamwise velocity. (a) Case S2, (b) case S4, tenth cycle, $t/T = 1$ (end of suction phase).	100
5.11	Streamwise, time-averaged distribution of the boundary layer integral parameters $\bar{\delta}^*$, $\bar{\theta}$ and \bar{H} in the symmetry plane for Case S2 (red line), S3 (black), S4 (blue). The laminar solution is depicted with dashed lines for comparison; in (c) also the value $\bar{H} = 1.4$ is shown (dot-dashed line) for reference.	101

LIST OF FIGURES

5.12 Time-averaged distribution of the skin friction coefficient \overline{C}_f along the streamwise direction in the symmetry plane for Case S2 (red line), S3 (black), S4 (blue). The laminar (Blasius) solution (dashed lines) and the turbulent correlation $\overline{C}_f(x) = 0.455/\log^2(0.06Re_x)$ are shown for comparison. 101

5.13 Instantaneous view of the vortical structures, highlighted by $\lambda_2 = -0.1$ isosurfaces, and coloured by the instantaneous streamwise velocity. (a) Case S1, (b) case S3, tenth cycle, $t/T = 1$ (end of suction phase). 102

5.14 Time-averaged distribution of the skin friction coefficient \overline{C}_f along the streamwise direction in the symmetry plane for Case S1 (green line) and S3 (black). The laminar (Blasius) solutions (dashed lines) and the turbulent correlation $\overline{C}_f(x) = 0.455/\log^2(0.06Re_x)$ are shown for comparison. . . 103

5.15 Contour map of the instantaneous streamwise deviation of the controlled flow from the Blasius solution; (a) Case S5, (b) case S6, $y/\delta_0^* = 0.8$, tenth cycle, $t/T = 1$ (end of suction phase). 104

A.1 Distribution of the Stuart function S along the wall-normal z axis for the unstable eigenmode of the OS operator applied to the channel flow instability; $\alpha = 1$, $Re = 10000$. The continuous vertical line corresponds to the critical elevation, while the two dashed lines define the critical layer width. . 112

A.2 Sketch of the two-fluid perturbed channel flow, with a generic elevation z_i of the fictitious interface. Even (sinuous) perturbation. 114

A.3 Orr-Sommerfeld spectrum for channel flow, $\alpha = 1$, $\beta = 0$, $Re = 10000$. 121 Chebyshev points have been used to discretize the normal direction. The Airy (A), Pekeris (P) and Schensted (S) branches are highlighted, following Mack's work [138]. 116

A.4 Marginal stability curve for different wall models. 117

List of Tables

2.1	Review of significant CFD studies of SJs in a quiescent environment.	25
2.2	Review of significant CFD studies of synthetic jets in cross-flow.	25
2.3	Test matrix of the computational runs. The number of elements (Nek5000) and cells (OpenFOAM) along each direction refers to the external environment only. The final column reports the total number of degrees of freedom (DOF) for each case.	32
3.1	Geometrical characteristics of the tested actuators.	48
3.2	Mechanical properties of shim and piezo-electric element. Subscript (*) stands for “s” and “p”, indicating the shim and the piezo-electric element, respectively.	48
4.1	Main non-dimensional parameters for the numerical simulations.	65
4.2	Main geometrical characteristics of the analyzed actuator.	74
4.3	Main dimensional and non-dimensional parameters for the analyzed case.	78
5.1	Non-dimensional parameters used in the simulations.	94
A.1	Critical Reynolds number, and corresponding α and c_r values.	117

Chapter 1

Introduction

1.1 International scenario

The environmental impact of the aerospace and the automotive industries has been widely investigated by researchers and policy-makers during the last decades. The recent concerns about the climate change, the threat of new oil crises and the growing air pollution detected in Europe's big cities has caused an urgent demand of technology improvements to be employed in the next-generation aviation fleet. Unfortunately, recent advancements in the civil aviation industry have been only partially able to deal with these problems, also due to the simultaneous increase in the number of flights within the last 5 years. According to the 2019 European Aviation Environmental Report [1], the number of flights in EU28+EFTA states increased by 8% between 2014 and 2017, while a larger growth rate is predicted for the next years. Fig. 1.1 depicts this trend, whereas the histograms in Fig. 1.2 presents a breakdown of the total number of flights into the main aviation categories: it is worthwhile noting that the growing influence of low-cost companies strongly influenced the reported rise in the annual number of flights.

As a consequence, the European Union has recently fixed clear thresholds on the future pollutant emission and the perceived aircraft noise. On the other hand, the civil aviation is of paramount importance for the European Union itself, as it strongly contributes both to the economy and the connectivity of the region. Therefore, several initiatives have been funded within the Horizon 2020 framework, with the aim of realizing a new, sustainable framework for the European aviation. Among others,

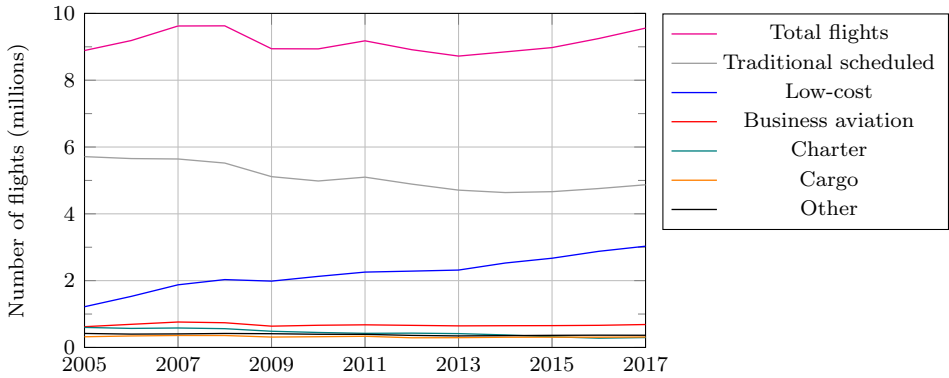


Figure 1.1: Time trends of the number of flights within EU and EFTA countries between 2005 and 2017. Adapted from [1].

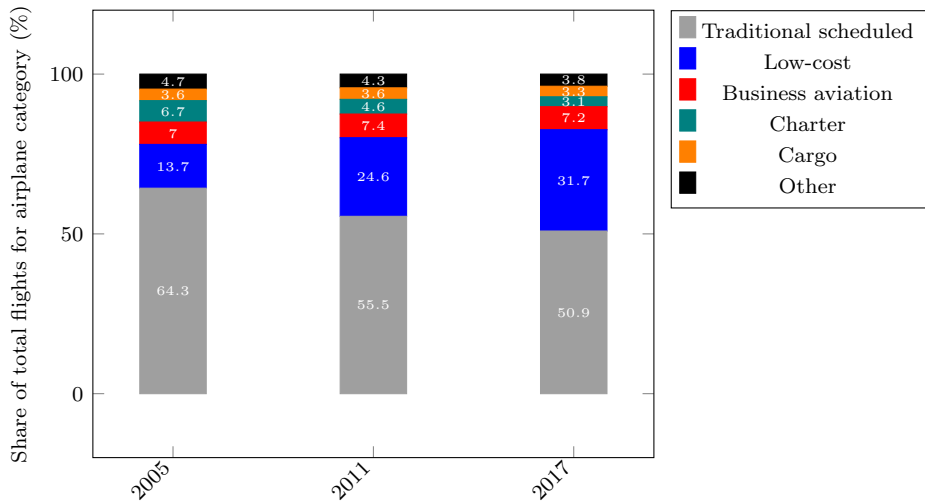


Figure 1.2: Distribution of the total number of flights within EU and EFTA countries between 2005 and 2017. Adapted from [1].

CleanSky2 [2] (and its predecessor CleanSky) research program aimed to develop innovative technologies, also pushing towards a synergic collaboration between universities and private companies. The focal point of the innovation in the aerospace industry is certainly the development of new

propulsion systems and/or alternative fuels, but a strong effort must be also paid in introducing novel concepts and innovative technologies into the aerodynamics of the airplane, optimizing its electronic systems and improving the efficiency of the airframe structures. In the aerodynamic field a great importance is related to the implementation of new techniques for drag reduction and lift increase, in order to increase the payload per flight, and therefore to reduce the environmental impact of the civil aviation (if normalized for a single traveller). This result can be achieved by means of innovative passive and active flow control (AFC) techniques, which manage to modify the behaviour of the flow about an aerodynamic surface in order to improve its performances.

The research activity carried out during this PhD period perfectly matches the purposes of this initiative. More specifically, the present doctorate project concerns the optimized design and the characterization of AFC techniques for the control of separated flows. Two recently introduced AFC systems, namely piezo-driven and plasma synthetic jet actuators, are investigated in the present work. Possible applications of such devices in the aerospace industry concern the stall delay of wings of new-generation aircrafts, and the reattachment of the flow around a vertical tail for drag reduction purposes. However, also the automotive and railway fields can take advantage of this technology: indeed, the pressure drag experienced by trains and trucks could be strongly reduced if the wake behind their body is properly controlled. Synthetic jet actuators have already proven to be useful devices in all the aforementioned fields, but a rational design of the jet in these cases is still lacking. This fact constitutes the main objective of the present work.

1.2 Separation control techniques

Separated flow regions are a common feature of many industrial fluid systems, such as flows around bluff bodies, aircraft wings and tails at high angle of attack, diffusers and ramp geometries. Flow separation in wall-bounded flows (as ducts and boundary layers) is usually caused by large regions of adverse pressure gradient, which forces the flow to detach from the wall. Such intense pressure gradients typically occur if the bounding surface is characterized by a high curvature. However, boundary layer separation in aerodynamic flows can be also created by shock-boundary layer interactions, sudden discontinuities in the surface geometry or being

intentionally created by the design employing, for instance, cylindrical or hemispherical roughness elements. On the other hand, separated flows can be also found in wakes and other free shear flows. A relevant example of industrial importance is reported in Fig. 1.3, which depicts the time-averaged velocity field of the interaction of two airstreams with different velocities U_1 and U_2 separated by a splitter plate. This figure has been obtained by a direct numerical simulation, using the popular open-source code Nek5000 [3]. The presence of a thick splitter plate, despite the relatively simple configuration, causes a rich variety of hydrodynamic phenomena both in the near field, which is dominated by the separated zone in the wake region, and in the far field, characterized by the development of a mixing layer, whose characteristics are strongly dependent on the velocity ratio between the streams. The transition from the wake behaviour to the mixing-layer one has been investigated by Braud *et al.* [4] using Proper Orthogonal Decomposition (POD), for different geometries of the splitter plate trailing-edge. The situation is even more complex if the incoming fluids have unequal densities or if heat transfer is taken into account, as in fuel and oxidizer streams in non-premixed combustors and gas-liquid atomizers.

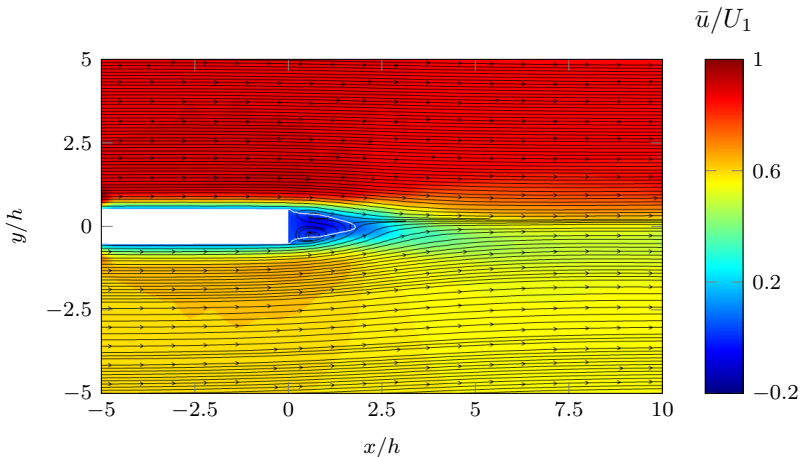


Figure 1.3: Time-averaged streamwise velocity field \bar{u}/U_1 and streamlines of the interaction between two different streams of velocities U_1 and U_2 , separated by a splitter plate of thickness h , $Re_h = (U_1 + U_2)h/(2\nu) = 600$, $\lambda_m = (U_1 - U_2)/(U_1 + U_2) = 0.2$. The white line $\bar{u} = 0$ is depicted to highlight the recirculation region.

As a general issue, complex phenomena, as Kelvin-Helmholtz instabilities on the edge of the separated zone, lead to undesired unsteady behaviours, which are often detrimental to the performance of the aerodynamic vehicle. The most harmful effect of the separation on aircrafts is the pressure drag, which is caused by a significant departure from the potential solution of the external flow field in the vicinity of the reversed flow region. This effect, indeed, modifies the pressure field around the entire aerodynamic surface, leading to an additional drag contribution, called pressure or form drag. Besides, separated flow is the main ingredient of the aerodynamic stall of wing surfaces, which strongly constrains the performance of lifting surfaces at high incidence angles. Extended region of separated flows can be found also in internal flows, as in nozzles and diffusers, still leading to unfavourable phenomena. The boundary layer thickness increases sharply downstream of the reversed flow region, thus enhancing the pressure drop between the inlet and the outlet, and it can also limit the maximum flow rate elaborated by the system. In severe conditions the blockage of the flow within the duct can be also obtained.

As regards the control of separation on boundary layers, various active and passive flow control techniques have been developed. Some devices are quite commonly employed in aircraft design, while other strategies are specifically tailored for the control of internal flows. Leading-edge and trailing-edge flaps are certainly the most common flow control techniques to mitigate the effects of separation on a lifting surface. Those devices are ubiquitous in the aerospace industry, since they have been introduced on almost every airplane since the beginning of the history of flight, in order to achieve higher values of the wing lift coefficient and delay the aerodynamic stall to higher values of the angle of attack [5]. This feature leads to smaller values of the minimum airplane velocity and, as a consequence, to reduce take-off and landing runs. The widespread diffusion of flaps within the aeronautic community paved the way to their application in other fields. Flaps, indeed, are also employed in the automotive industry to optimize the aerodynamic performances of race cars. In this context they act in an opposite way, aiming to increase the downforce generated by the wing with a reasonably small drag penalty, as explained in the review paper by Katz [6]. Finally, rigid or flexible flaps have been also employed for heat transfer enhancement, as shown in Ali *et al.*'s work [7].

Besides, several flow control strategies have been introduced to prevent separation, including morphing structures, porous surfaces, vortex gener-

ators, acoustic excitation and fluidic systems. Prandtl [8] first introduced the idea of controlled suction/blowing, in order to modify the characteristics of the streamwise velocity distribution next to the separation point. Its celebrated experiment on the boundary layer control of a circular cylinder in crossflow showed that this approach can be successfully applied to avoid separation, and its following work [9] constitutes one of the first examples of optimized design of jet-based control system. Further studies were carried out to relate the characteristics of the controlled flow field with the momentum injected by the control device, its position along the cylinder surface and the jet inclination. These studies laid the foundation for the design of pulsed jets for separation control applications. Gilarranz *et al.* [10] successfully applied synthetic jet actuators to control the flow over a NACA0015 airfoil in stall and post-stall conditions. Their flow visualization technique showed that the fluid remains attached to the wing surface in the controlled case over the entire chord span. Hlevca *et al.* [11] employed strong, pulsed jet to control the recirculation bubble past a backward facing ramp; dielectric barrier discharge (DBD) plasma actuators have been also applied for the control of separation of a backward facing step by Sujar-Garrido *et al.* [12], whose analysis mainly focused on the optimal location of the control device and its forcing. DBD actuators have been also used for separation control on aircrafts, for instance in Rethmel *et al.*'s research [13].

Another simple approach to deal with separated flows on wings and airfoils is probably to induce transition to turbulence upstream of the reversed flow region, as the higher shear stress of a turbulent boundary layer profile makes the flow more resistant to separation. This result can be achieved using roughness elements, micro-vortex generators and other tripping devices. All these devices are commonly referred to as turbulators in the context of transition-promoting devices [14]. The various routes to transition in a flat-plate boundary layer are effectively summarized by Morkovin's classification [15]. It is well known that, according to the linear stability theory, boundary layers on a flat plate become spatially unstable at a Reynolds number (based on the freestream velocity U_∞ and the local boundary layer displacement thickness δ^*) of $Re_{\delta^*} = 520$. This leads to the formation of hairpin structures, which eventually undergo secondary instabilities and ultimately causes the flow to transition to a turbulent state. However, if large disturbances are introduced into the flow system, bypass transition occurs, which typically moves upstream

the entire transition process. This approach can be followed to force the transition point at a fixed position along the airfoil chord in a certain flight phase; however, the flow generated by turbulators is strongly dependent on the characteristics of both the control system and the freestream velocity, and an optimized approach for their design is far to be obtained. This issue will be widely addressed in Sec. 1.4.

Acoustic excitation can be also employed to control both internal and external flows. The reader can find more information about this topic on the review paper by Greenblatt and Wygnanski [16], and citing references. This framework was initiated by the experimental observations of Schubauer and Skramstad [17], who realized that the transition behaviour of a boundary layer can be modified by sound waves. The effect was found to be strongly dependent on the sound frequency and intensity. Following studies by Ahuja *et al.* [18] and Ahuja and Burrin [19] showed that the separation of a turbulent boundary layer in stall conditions can be significantly delayed by sound waves. A massive effort, therefore, has been carried out to determine the scaling laws for the ‘optimal’ sound frequency, to maximize the interaction between the acoustic waves and the separated shear layer, which is responsible for the controlled flow behaviour.

Porous surfaces and perforated plates also allowed to deal with separated zones, especially on transonic wings: the system is located in the (expected) shock region, and a empty plenum, located underneath the surface, is used to link the regions located upstream and downstream of the shock wave. It has been demonstrated that shock-induced separation can be mitigated by means of this approach, and flow separation can be significantly delayed, which is beneficial for the performances of the aircraft. The effectiveness of active and passive suction for the present case have been investigated by Krogmann *et al.* [20] for a supercritical airfoil.

Finally, another strategy to deal with separation on both aerodynamic and bluff bodies makes use of moving objects and coatings. Piezoelectric flaps have been proposed by Seifert *et al.* [21] for separation control and stall delay, working similarly to passive devices as MVGs. Modi *et al.* [22] proposed to replace the leading edge of the airfoil with a rotating cylinder: its wind tunnel tests revealed that huge increases in the maximum lift coefficient and the stall angle can be achieved. However, the implementation of this technique on a civil aviation aircraft could be hardly feasible. Hairy coatings, instead, has been tested on the wake behind a circular cylinder by Favier *et al.* [23], inspired by the feather coating over the wings of

birds. They found, by means of CFD computations, that such coatings are able to mitigate the effect of the vortex shedding, which is beneficial for drag reduction.

1.3 Synthetic jets

Synthetic jets (SJ) are generally produced by micro acoustic-mechanical systems (MEMS) and are involved in several industrial applications, as flow control, electronic cooling, mixing and heat transfer enhancement, control of liquid jets and sprays and micropropulsion, as reported in the review works of Cattafesta and Sheplak [24] and Mittal and Mohseni [25]. The generation of a synthetic jet requires the design of an actuator that is able to produce a turbulent jet from the periodic alternation of fluid ejection and ingestion in a small cavity. The actuation principle can exploit several physical phenomena, leading to different actuator configurations. The first devices were based on the oscillations of a piston within a cylindrical cavity, which was connected to the external environment through one or more orifices. This simple system was not suitable for implementation in industrial applications, therefore several alternative configurations have been proposed: their design was based on woofer and piezoelectric technologies, plasma generation, thermoacoustic effect and acoustic excitation. Two common techniques, namely the piezo-driven synthetic jets and plasma synthetic jet, are described in the following.

Piezo-driven synthetic jets are generally composed of a small cavity, which is closed on one side by a flexible diaphragm, and connected to the external flow by one or more orifices. Fig. 1.4 depicts the baseline geometry of this actuator, and introduces the fundamental components of this actuator. The oscillation of the diaphragm, which is generally constituted by a thin metallic shim on which a piezo-ceramic element is glued, produces periodic cavity volume changes, and correspondingly pressure variations within the cavity. When the internal pressure is bigger than the ambient one, the fluid is ejected from the orifice, while the cavity is refilled during the suction phase. The evolution of the vortex ring in the actuator symmetry plane is shown in Fig. 1.5, for a slotted SJ actuator. During the ejection phase a vortex ring (a rectangular vortex in the slotted case) forms near the lips of the orifice exit which, under favourable operating conditions, convects itself downstream. If the control system is properly designed, the vortex is not ingested during the suction

phase, and after a few cycles a train of vortices, which interact with each other, is formed. Viscous dissipation is then responsible for the break-up of the vortical structures, eventually leading to a turbulent jet always directed downstream in the far-field region.

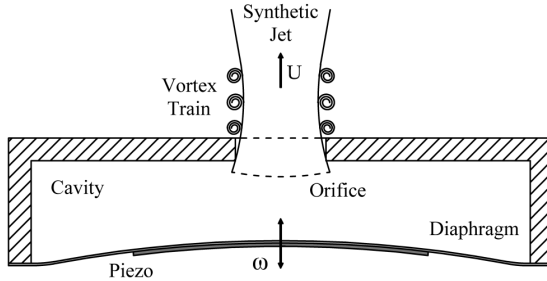


Figure 1.4: Sketch of a piezo-driven synthetic jet device.

The behaviour of the flow during the suction phase is shown in Fig. 1.6: a stagnation point is formed, the so called saddle point, which is approximately located one to three orifice diameters away from the orifice itself (depending on the jet Reynolds number and the actuator geometry). The extremal position of this point can be used to conventionally separate the near field region, where the flow is directed towards the cavity in the suction phase, from the far field where the turbulent jet is established.

A major characteristic of this jet is that the average mass flow rate during an operation cycle is null, whereas a non-zero average momentum rate is produced. This feature, along with their high flexibility, wide operating frequency range and reduced weights, sizes and total cost, makes this flow control technique particularly attractive for flow control applications, especially in aerospace and automotive applications. The major drawbacks of these devices are related to the low reliability (due to the presence of the moving diaphragm, which strongly suffers from fatigue phenomena), and the relatively small exit velocities, if compared with other flow control actuators. However, piezo-driven SJ actuator has been used to optimize the aerodynamic forces on aircrafts and control the wake behind cars, trucks and trains. Other typical applications can be found in the heat transfer context (in impinging configuration), for electronic cooling and in the separation control of wing in stall conditions and ramps.

On the other hand, Plasma Synthetic Jet (PSJ) actuators are able to

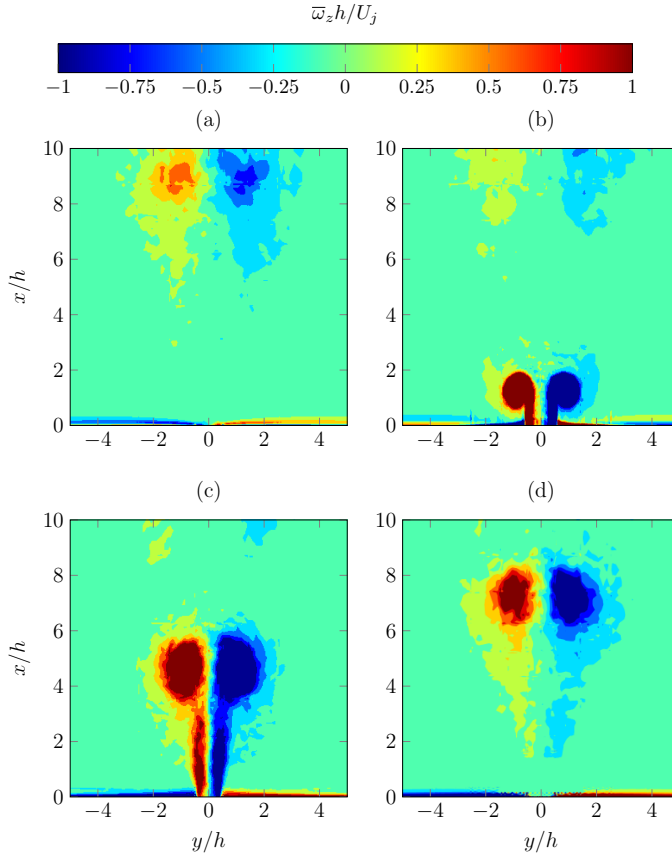


Figure 1.5: Near-field evolution of the vortical structures for a slotted SJ in quiescent conditions. (a): $t/T = 0$, (b): $t/T = 0.25$, (c): $t/T = 0.5$, (d): $t/T = 0.75$.

produce very high jet velocities, without any moving parts, thus outperforming the piezo-driven SJs in such fields. It is generally composed of two or three electrodes, embedded in a small cavity, and linked to the external environment through an orifice. The operating cycle of a plasma synthetic jet is depicted in Fig. 1.7; it begins with an electrical discharge between the electrodes, which sharply increases the cavity temperature and pressure. The high-pressure air exhausts through the orifice, converting the increased internal energy into kinetic one. In the end, fresh air is drawn back inside the cavity, refilling the device for the next pulse. After a lim-

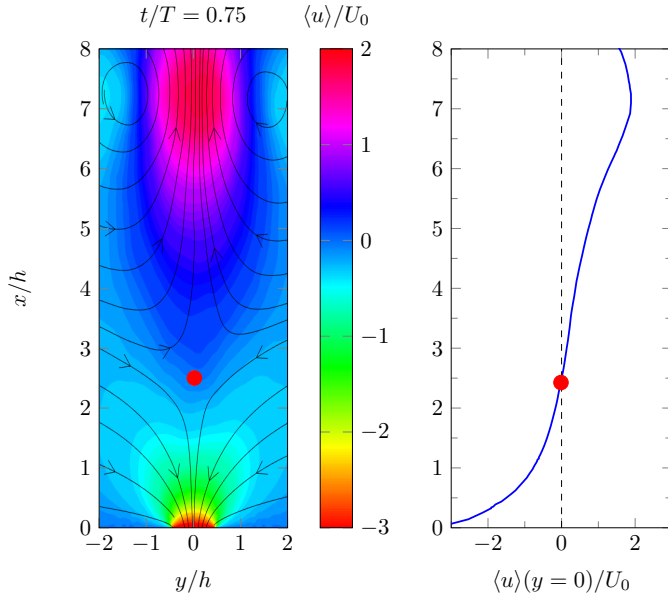


Figure 1.6: Contour map of the phase-averaged velocity and corresponding centerline velocity profile at suction peak. The red point indicates the saddle point position.

ited number of cycles the device reaches a periodic behavior, generating a synthetic jet.

Plasma synthetic jet actuator has been initially developed at the Johns Hopkins University at the beginning of the 2000s [26], and subsequently involved in several research activities and international projects. The interaction between a PSJ actuator and a morphing wing flap on a new-generation aircraft has been recently investigated by the present research group within the CleanSky2 project, as shown in a recent work [27]. It is worthwhile noting that, contrarily to piezo-driven SJs, plasma synthetic jets are not zero-net-mass-flux.

Finally, novel synthetic jet devices have been introduced in the last couple of years. Li and Zhang [28] defined the concept of hybrid synthetic jet actuators to overcome the limitations in exit velocity of piezo-driven synthetic jets. They demonstrated, by means of numerical simulations and a dedicated lumped model, that this device is able to reach high jet velocities by adding a piezo-driven diaphragm at the lower end of a

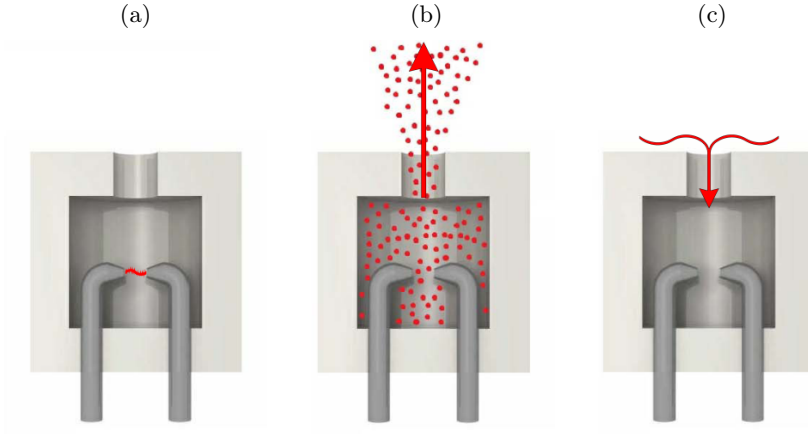


Figure 1.7: Schematic view of the operation cycle of a plasma synthetic jet actuator. (a): energy deposition stage; (b): jet discharge; (c): refill.

PSJ. Chen *et al.* [29], instead, proposed a new class of synthetic jets based on the thermoacoustic effect. A thermoacoustic engine (TAE) is employed to produce thermoacoustic standing waves, whose energy is used to produce a synthetic jet. As PSJ actuators, therefore, their device does not include any moving part, which improves the reliability of the system. Moreover, preliminary simulations showed that this new actuator type clearly outperform the piezo-driven actuator in terms of exit jet velocity. The authors argued that this device should be cheaper and simpler than plasma actuators; however, further investigations must be carried out in order to understand the relation between the thermoacoustic instability of the flow within the actuator and the performance of the device. Both hybrid and thermoacoustic devices must prove to be suitable for practical flow control applications.

The present PhD activity mainly concerns piezo-driven synthetic jets, from both a theoretical, numerical and experimental point of view. A calibrated lumped element model for the evaluation of the PSJ performances in quiescent conditions is described in Sec. 3.1.

1.3.1 Dimensionless parameters and data reduction

The performance of piezo-driven synthetic jet actuators are evaluated in terms of a set of dimensionless parameters. The main dimensionless parameters for a synthetic jet issuing in a quiescent environment are the jet Reynolds, Stokes and Strouhal numbers, defined in Eq. (1.1)

$$Re_0 = \frac{U_0 d}{\nu}, \quad St_0 = \frac{2\pi f d}{U_0}, \quad S = \sqrt{\frac{2\pi f d^2}{\nu}} \quad (1.1)$$

where d is a relevant length scale (the jet smaller dimension for rectangular or elliptic orifices, the jet diameter for circular orifices), f the actuation frequency and ν the air kinematic viscosity. In the present thesis work the reference length for slotted configurations is called h . The averaged jet velocity U_0 is defined by Eq. (1.2), where T is the actuation period.

$$U_0 = \frac{1}{T} \int_0^{T/2} \left[\int_A U(x=0, y, z) dydz \right] dt \quad (1.2)$$

The stroke length L_0 is then defined as $L_0 = TU_0$. This parameter represents the length of a (hypothetical) slug of fluid which is ejected during the expulsion phase, as explained by Smith and Glezer [30], and is related to the distance covered by the vortex rings during this period. The definition of the stroke length can be understood by observing the geometrical construction in Fig. 1.8, obtained by the direct numerical simulation of a slotted actuator. It is worth noting that the dimensionless numbers are not independent, but they are related by $St_0 = S^2/Re_0$. Moreover, in some applications the averaged jet velocity is replaced by the time-averaged centerline velocity of the jet during the ejection phase U_j to obtain the jet non-dimensional parameters. This leads to slightly different evaluations of Reynolds and Strouhal numbers and the stroke length. In the present thesis work these quantities will be denoted with the subscript $(\cdot)_j$, whereas the one obtained using the reference velocity (1.2) will be indicated by the subscript $(\cdot)_0$.

The results of the simulations are post-processed, throughout the thesis work, in terms of time-averaged fields, phase-averaged velocity fields and phase-averaged Reynolds stresses. Indeed, is worth mentioning that the study of flows where a periodic component may be distinguished from a residual, random component is generally carried out using the triple de-

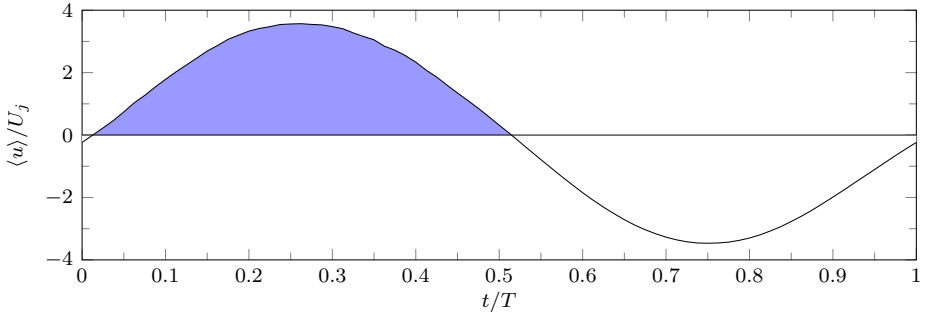


Figure 1.8: Time evolution of the phase-averaged centerline velocity at the orifice exit during the actuation cycle, for a slotted synthetic jet actuator. The blue area depicts the definition of stroke length L_j .

composition introduced by Hussain & Reynolds [31], as shown in Eq. (1.3):

$$u(x, t) = \langle u(x, t) \rangle + u'(x, t) = \bar{u}(x) + \tilde{u}(x, t) + u'(x, t) \quad (1.3)$$

where \tilde{u} is the coherent, fluctuating component of the instantaneous velocity, \bar{u} the long-time averaged flow field, $\langle u(t) \rangle$ the phase-averaged velocity and u' the turbulent fluctuation. In the present research the phase-averaged velocity is obtained as the ensemble average of all the velocity fields realized at a fixed phase ϕ . Finally, for this type of flows the phase-averaged Reynolds stress tensor $\tau_R = \langle u'u' \rangle$ is also an important quantity, often employed to detect zones characterized by high values of turbulent intensity and possible flow transition/relaminarization during the actuation cycle.

As regards the interaction between a synthetic jet and a crossflow, the flow physics is strongly dependent on the jet-to-crossflow velocity ratio and the ratio between the a characteristic frequency of the flow and the actuation one. These relationship are generally written in terms of the momentum coefficient C_μ and the reduced frequency F^+ , defined by Eqs. (1.4)

$$C_\mu = \frac{\rho_j U_{j,max}^2}{\rho_\infty V_\infty^2}, \quad F^+ = \frac{f}{f_{ref}} \quad (1.4)$$

where $U_{j,max}$ is the maximum jet velocity, located on the center of the orifice exit plane. If a sinusoidal approximation is assumed for the time

variation of the exit jet velocity, it can be stated that $U_{j,max} = \pi U_j$. For laminar boundary layer the reference frequency can be derived from the linear stability theory. The momentum coefficient reduces, in the present case, to R_j^2 , where R_j is the jet-to-BL velocity ratio (again, in terms of the maximum jet velocity). Moreover, a further relevant parameter which must be controlled (both in experimental and numerical studies) is the ratio between the jet diameter and a characteristic wall-normal length of the uncontrolled crossflow. In the present work the displacement thickness at the jet center δ_0^* for the uncontrolled boundary layer is chosen as reference length. This quantity can be obtained, for laminar boundary layers, using the Blasius similarity solution.

1.4 Towards a rational design of AFC systems

Since the end of World War 2 a massive research effort has been paid in order to understand the behaviour of a crossflow, when subjected to a certain flow control technique (generally by means of on passive methods or closed-loop devices). A typical outcome of such investigations is shown in Fig. 1.9, for a commonly employed drag reduction strategy, an array of localized roughness elements.

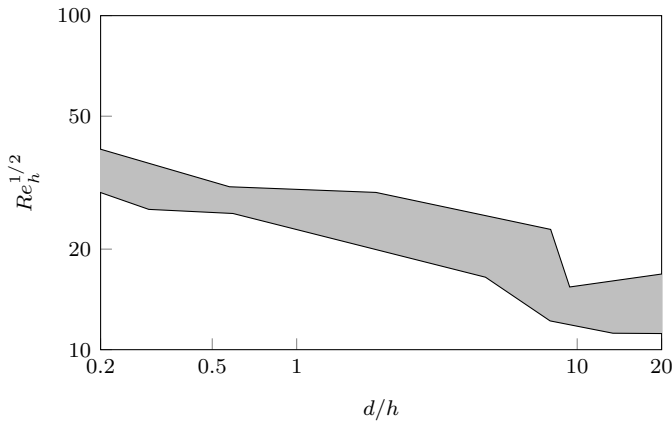


Figure 1.9: Reproduction of the transition diagram obtained by Von Doenhoff and Braslow [32] for an array of roughness elements. The filled gray area depicts the region of the $d/h - Re_h$ plane where transition to turbulence has been experimentally detected.

Von Doenhoff and Braslow [32] obtained, as a result of an extensive experimental campaign, a ‘transition diagram’ in the $d/h - Re_h$ plane (where d and h are, respectively, the diameter and the height of the roughness element, and Re_h a Reynolds number based on the theoretical value of the Blasius velocity profile U_{BL} at the roughness higher surface), which allowed to distinguish between favourable combinations of flow and control parameters and situations where the flow control technique has a detrimental effect on the performance of the surface. The preliminary design of these devices could take advantage of this diagram, whereas further tests should have been accomplished for their implementation on a lifting surface. The main issue of this approach is that these results were often driven by empiricism, and no information about the mechanism leading to the controlled flow features are given. For this reason these findings often have a small applicative range and must be used carefully, since they could have been influenced strongly by noise parameters as the freestream turbulence or (ubiquitous) sources of disturbances.

However, a more rational approach has been carried out during the last years, generally based on the coupling of fluid-dynamic instability, modal reduction techniques and *ad-hoc* experimental/numerical campaigns. The vortical structures generated by the application of a flow control device on a flow to be controlled are explained in terms on linear modes, whose spectral characteristics are in turn compared to the experimental/numerical findings. This not only allows to explain the nature of the driving mechanisms generated by the actuator, but also to create, in some cases, linear, reduced-order models of the flow system, which can be used to better design the actuators. Closed-loop control can be handled in a similar way: the time variation of the control law can be obtained in terms of the current state of the flow, measured by one or more sensors. An input-output model can be created to link the output signal of the sensors and the actuator, either in feedback or feedforward fashion, in order to optimize a certain characteristic of interest. This approach, based on proper orthogonal decomposition or other modal reduction techniques, has found a solid background in the control theory, developed for the management of electrical circuit, and it has been successfully applied to the closed-loop control of the flow separation induced by an open cavity by Barbagallo *et al.* [33] and the transition delay on a flat-plate boundary layer by Semeraro *et al.* [34].

A modern investigation on the effectiveness of a passive control tech-

nique can be found in the recent work by Puckert and Rist [35]. This investigation allows to explain that roughness elements are able to produce streaky structures, which in turn are able to delay transition on a flat plate by reducing the spatial growth rate of the Tollmien-Schlichting waves for appropriate values of a properly defined Reynolds number and the roughness aspect ratio. Nonetheless, in many practical situations the streaks become unstable, leading to early transition just downstream of the control surface, which explain its detrimental effect on the aerodynamic drag. It has been also observed that the flow behaviour is highly sensitive to a large set of parameters, including also the spanwise distance between two consecutive elements and the freestream turbulence, which can dramatically modify the instability and transition of the flow. A quantitative comparison between theoretical and experimental results showed that the present hypothesis well explains the behaviour of the controlled flow and gave important information for the design of new passive control devices.

The approach followed by Puckert and Rist [35] in this example has become the state-of-the-art workflow to deal with several flow control applications. Recent studies generally rely on global stability analyses, as well as energy methods and data-driven approaches, to find the optimal position of the actuator and its optimal control law. All these approaches are briefly outlined in the following. Global stability analyses are based on the resolution of the linearized Navier-Stokes equations, obtained by the decomposition of the instantaneous flow field \mathbf{U} into a base flow $\bar{\mathbf{U}}$ and a small fluctuation \mathbf{u}' . Perturbations are imposed to have a modal behaviour in time; introducing this ansatz in the linearized Navier-Stokes equations leads to an eigenvalue problem, which can be solved to analyze the (linear) instability of the flow. It is possible, with the current computational resources, to perform three-dimensional stability analysis of complex flows, whereas researchers, in past times, relied on simplifying assumptions on the spatial distribution of the perturbation field in order to reduce the computational size of the problem. This approach allows to obtain qualitative information about the instability mechanism; to obtain quantitative information about the flow control design adjoint methods and sensitivity analyses have been introduced. Indeed, these types of investigation are intended to provide the location of the ‘wave-maker’, namely to identify the regions where the instability originates. As discussed in the review paper by Camarri [36], the huge interest in such

methods from a flow control perspective is clear: the sensitivity of a flow to a steady forcing can be related to the introduction of control systems into the flow domain. As an example, Marquet *et al.* [37] investigated the control and stabilization of the Von Karman vortex shedding behind a circular cylinder by placing a small cylinder in the downstream region of the flow. The optimal control region found by the sensitivity analysis was found to be in fair agreement with the previous experimental study by Strykowski and Sreenivasan [38], which constitutes an evidence of the potential capability of sensitivity analyses in flow control design.

Another interesting application of fluid-dynamic-stability-based tool for flow control design is based on the perturbation energy budget. The rational basis for the energy budget approach to the instability of incompressible flows was given by the Reynolds-Orr equation (1.5), which governs the time evolution of the disturbance energy $E = u'_i u'_i / 2$, for a given base flow $\bar{\mathbf{U}}$:

$$\frac{dE}{dt} = - \int_{\mathcal{V}} u'_i u'_j \frac{\partial \bar{U}_i}{\partial x_j} d\mathcal{V} - \frac{1}{Re} \int_{\mathcal{V}} \frac{\partial u'_i}{\partial x_j} \frac{\partial u'_i}{\partial x_j} d\mathcal{V} \quad (1.5)$$

One can note that the time derivative of the disturbance energy is obtained as the difference of two terms: the first one is commonly attributed to the energy exchange between the base flow and the perturbation, and, depending on its sign, can lead the flow towards the instability. Conversely, the second one always acts as a dissipative term, therefore it is always stabilizing. For this reason, these terms are often called, respectively, production and dissipation of perturbation, in analogy with the corresponding terms in the fluctuating energy equation for turbulent flows. Energy methods have been initially conceived to give information about the instability of viscous incompressible flows, leading to a branch of the fluid dynamic instability that is, somehow, complementary to the modal stability theory (as widely explained in the book by Schmid and Henningson [39]). Besides, the detection of the regions where the production term is much bigger than the dissipation one could be worthwhile to gain information about the design of flow control techniques devoted to attenuate the unsteadiness of the investigated flow. This feature is briefly discussed in Appendix A with reference to the channel flow instability; a new pseudo two-phase model, developed within the present doctoral work, is also presented in the Appendix.

Finally, in the last decades a great number of data-driven modal de-

composition techniques has been introduced, starting from the classical proper orthogonal decomposition, up to the recently introduced dynamic mode decomposition (DMD) and spectral POD. The main aims of these techniques are to provide a low-rank approximation of the flow (that it is necessary for flow control applications because a dynamical system arising from a straight-forward discretization of the Navier-Stokes equations for control purposes is still intractable) and recognizing coherent structures of the flow. Differently from stability analyses, which are based on the study of the (linearized) governing operator, these techniques are based on the knowledge of the time evolution of the flow field (that could be obtained using either experimental techniques or numerical simulations). Obviously, global stability analyses require the (numerical) solution of an eigenvalue problem, while the data-driven approach can handle both numerical data or experimental measurements. Indeed, in both POD and DMD approach data are arranged in snapshots: POD techniques reconstitutes an optimal, orthogonal set of basis vectors by analyzing the covariance matrix, whereas DMD aims to decompose data into a set of modes, each one with a single characteristic frequency and growth rate. The determination of both the modes and their characteristic frequency in DMD is based on approximating the relationship between two consecutive snapshots with a linear operator.

As a general conclusion, therefore, it can be said that a joint analytical/experimental procedure for the design of several passive flow control devices is nowadays available in literature, as well as analytical input-output approaches for low-dimensional sensors-actuators systems. Unfortunately, literature works related to the evaluation of a low-dimensional representation of synthetic jets in crossflow are still lacking. There are many research works with the aim of obtaining a lumped element modeling (LEM) of synthetic jets in quiescent conditions, with different philosophies and approximations, which can be used as a starting point for a reduced-order modelling of the former problem. A proper way to obtain such models could be related to stability investigations of the controlled system, but the stability of a fully tridimensional system around a periodic solution is still a difficult task, then in the present research a receptivity analysis of the boundary layer flow to the jet actuation, based on linear stability studies around the uncontrolled state, has been carried out.

1.5 Aim of the work and thesis structure

The present thesis work deals with two open issues for the design of such devices for separation control: a first task of the research activity is devoted to investigate the jet/crossflow interaction, with special reference to the influence of the jet in the transition behaviour of the crossflow. This step is mandatory for the optimized design of a synthetic jet actuator to control more complex crossflows, as airfoils in stall conditions, bluff body wakes and mixing layers. The chosen crossflow is a laminar boundary layer on a flat plate, as a baseline case to properly compare the characteristics of the uncontrolled and the controlled flow. The numerical findings are corroborated by comparison with other, similar flow fields, generated by passive control systems as roughness elements.

The other task of the activity consisted in refining existing design and simulation approaches for synthetic jets in quiescent conditions (i.e. without a grazing flow). More in depth, a comparison between different computational approaches for the aforementioned problem has been carried out, in order to ascertain the best numerical setup. Besides, a wide analysis on the flow field generated by multiple-orifice actuator have been performed, in order to investigate the interaction between adjacent jets. Two configurations have been selected: a first one based on a double-orifice, single cavity actuator, employed to specifically study the interaction between two jets, and another one composed of several slots and designed for the optimized control of the separated flow created by a ramp.

It is worth noting that the partition of the doctoral activity into two research lines, however, is only apparent, since the main aim of the work is to build a rational approach for the design and characterization of synthetic jets for industrial applications. A typical workflow for the design of such devices must obviously include investigations of the uncontrolled and the controlled field (which, in this case, are obtained via numerical simulations) to find the optimal design parameters of the actuator (velocity, frequency and position). However, the design of an actuator which is capable of matching these requirements is generally carried out in quiescent conditions, using both LEM approaches and experimental/computational campaigns. The latter step is crucial if unconventional actuators are employed, since standard LEMs are often not suitable for dealing with such devices.

The thesis is organized as follows. Chapter 2 provides a critical review on the choice of the numerical setup for the simulation of synthetic jets, by

means of an extensive comparison of low-order and high-order numerical methods for the direct numerical simulations of synthetic jets. The choice of the numerical solvers employed for the numerical simulations carried out during the doctoral period has been made according to the results of this comparative investigation. Besides, the outcomes of this study are expected to be useful not only for the flow control community, but also for other research fields.

Chapter 3 is devoted to briefly outline recent advancements in the lumped element modeling of synthetic jet actuators in quiescent conditions. Firstly, a calibrated lumped element model for the prediction of the performance of a plasma synthetic actuator has been developed. A LEM-based design approach, able to predict resonance amplifications and jet formation for synthetic jets in quiescent conditions, is then explained; implications of the LEM approach in simulating piezo-driven SJ actuators are briefly reported afterwards.

Chapter 4 faces the characterization of multiple-orifices and multi-slotted synthetic jet actuators in quiescent conditions. This activity included numerical simulations of the internal and the external flow field, focusing mainly to the development and the interaction between the vortical structures formed at the orifice exit. Experimental measurements, obtained via hot-wire anemometry (HWA) have been carried out for the slotted actuator, and used to evaluate the frequency response of the actuators and validate the numerical simulations. Both configurations have been specifically designed (in terms of geometry, peak velocity and design actuation frequency) to match the performances required to optimally control separated flows.

Finally, Chapter 5 concerns the numerical characterization of a low-speed synthetic jets issuing in a realistic, wind tunnel flat plate boundary layer. The innovative aspect of this work is that the actuation frequency of the jet is chosen according to the linear stability of the boundary layer, in order to evaluate its efficiency. A series of direct numerical simulations have been carried out, by studying the influence of several design and noise parameters on the resulting flow field. More in depth, the actuation frequency, the boundary layer inlet Reynolds number and the inlet turbulent intensity of the boundary layer are systematically varied to ascertain the effect of such variables on the turbulent development of the flow.

Chapter 2

Numerical tools for SJ design and characterization

A strong contribution on the knowledge of synthetic jet flow fields has been brought by numerical simulations. Indeed, CFD analyses allowed to obtain high-resolution data for the velocity and the pressure fields, to carry out parametric analysis of the resulting flow (in terms of the actuator geometry, actuation frequency and crossflow characteristics) and to recognize the vortical structures arising from the SJ actuation. The simulation of synthetic jets both in quiescent environment and in crossflow condition poses severe challenges, since the resulting flow fields are both rather complex. For this reason, a crucial step of the present doctoral work has been to find the most suited approach in simulating synthetic jets. A comparative investigation of two open-source solvers, Nek5000 and OpenFOAM, has been carried out, in order to establish some guidelines on the choice of a numerical code for the simulations of synthetic jets. Time- and phase-averaged velocity fields and phase-averaged Reynolds stresses have been compared to an experimental dataset obtained in the same flow conditions; further investigations concerned the computational cost of the simulations and the parallel performances of both codes.

In the following section a brief introduction on the simulation approaches employed for SJ simulation has been made; this Section includes an exhaustive review of the existing literature. Sec. 2.2 concerns open-source solvers: the use of such codes in the CFD community is widespread nowadays, and both Nek5000 and OpenFOAM fall into this category. Finally, Sec. 2.3 is devoted to the performance comparison of such codes

in simulating synthetic jets. The results of this investigation are briefly summarized at the end of the Chapter, explaining how the choice of the proper numerical code has been made for each of the simulations shown in the following Chapters.

2.1 Introduction

As regards the investigation of synthetic jets in quiescent conditions, the first notable computation has been carried out by Kral *et al.* [40], who performed 2D RANS simulations and did not include the cavity in the computational model. Later, Rizzetta *et al.* [41] were able to reproduce the spanwise instability mechanisms uncovered experimentally by Smith & Glezer via DNS. Subsequently, an attempt to compare the performance of different CFD methods and clarify some computational issues was made at the 2004 *Synthetic Jets and Turbulent Separation Control Workshop*, organized by NASA Langley Research Center. Three test cases were proposed: a slotted synthetic jet in quiescent external flow, the interaction between a turbulent boundary layer and a synthetic jet and the control of the separated flow behind a ramp geometry. The results of the workshop were summarized by Rumsey *et al.* [42], who observed strong discrepancies between the numerical results of the contest. The quiescent case was later investigated via DNS by Kotapati *et al.* [43], who obtained a good agreement between the computational findings and the experimental data.

Table 2.1 attempts to summarize twenty years of computational research on synthetic jet in quiescent conditions. It is interesting to observe that several numerical methods have been employed for the computations. As a conclusion, Direct Numerical Simulation is nowadays the state-of-art technique to deal with SJs in quiescent conditions, since the present computational resources allow to obtain space and time-resolved solutions in acceptable times. However, a rather wide variation in the results has been observed, and it is not clear which specific technique and modelling approach are the best suited for predicting the flow behaviour. In fact, DNS is able to obtain a decent view of both the averaged flow and its spectral features; nonetheless, the accomplishment of high-fidelity simulations is still strongly dependent on the chosen computational setup.

On the other hand, the choice of the computational method to properly simulate SJs in grazing flows is still dependent on the application. While direct numerical simulations of the interaction between a laminar

Table 2.1: Review of significant CFD studies of SJs in a quiescent environment.

Authors	Modeling	2D/3D	Numerical method
Kral (1997) [40]	RANS	2D	Third-order flux-difference splitting
Rizzetta <i>et al.</i> (1999) [41]	DNS	3D	High-compact finite-differences
Lee & Goldstein (2002) [44]	No model	2D	Fourier-Chebyshev spectral method
Menon & Soo (2004) [45]	LES	3D	Lattice-Boltzmann
Carpy & Manceau (2006) [46]	RANS	2D	Second-order finite-volume
Cui & Agarwal (2006) [47]	RANS	3D	Second-order upwind finite-volume
Kotapati (2007) <i>et al.</i> [43]	DNS	3D	Second-order finite-differences
Arad <i>et al.</i> (2014) [48]	LES	3D	Second-order finite-volume
Mu <i>et al.</i> (2018) [49]	DNS	3D	Lattice-Boltzmann

boundary layer and a synthetic jet are still feasible, their application in crossflow conditions often forces to use RANS or LES computations. Some significant CFD investigations of synthetic jets in crossflow are summarized in Table 2.2. It is worthwhile noting that DNS is restricted only to simple flow configurations, as low-Reynolds-number boundary layers on a flat plate, controlled cylinder wakes and, in recent works, to study separated flow control applications, whereas LES and RANS computations are often employed to deal with high-Reynolds-number separated flows, stall control on airfoils and wings and controlled turbulent boundary layers. A strong effort has been carried out in the last years to employ LES or hybrid RANS/LES techniques, capitalizing on the recent improvements in the performance of the supercomputers.

Table 2.2: Review of significant CFD studies of synthetic jets in crossflow.

Authors	Modeling	Application
Dandois <i>et al.</i> (2007) [50]	DNS/LES	Control of a backward-facing ramp
Kim & Kim (2007) [51]	RANS	NACA0015 airfoil separation control
Zhou & Zhong (2009) [52]	DNS	SJ in laminar boundary layer
Sahni <i>et al.</i> (2011) [53]	DNS	Controlled flow on a NACA airfoil
Lardeau & Leschziner (2011) [54]	LES	Control of a backward-facing ramp
Wen & Tang (2014) [55]	DNS	SJ in laminar/turbulent BL
Jansen <i>et al.</i> (2018) [56]	DDES	Separation control on a vertical tail
Seo <i>et al.</i> (2018) [57]	DNS	Laminar separation bubble control
Belanger <i>et al.</i> (2020) [58]	LES	Slotted SJ in turbulent BL

2.2 The increasing importance of open-source solvers

In the last decades several research projects and industrial companies relied on open-source and/or in-house codes for the simulations of a certain type of flow. Interestingly, the widespread diffusion of such CFD codes in place of commercial software is not strictly related to the investment associated with the license acquisition. The main concern about commercial software is often related to their reduced specialization: since these codes are designed to handle complex phenomena, it is often difficult to obtain high-fidelity simulations of many fluid systems, especially for DNS and LES applications. This fact often leads to stability and convergence issues, which are often related to the low-order, well-established schemes typically employed in such programs. These issues could be solved by the final user by asking for support to the software house, which often leads to wait for the new release of the software.

On the other hand, an open-source code is often specifically designed for a smaller range of applications, but clearly outperforms the other ones in its own specific field. Moreover, the final user of the solver is often allowed to modify the code, introducing, for instance, new temporal or spatial discretization schemes, new I/O procedures, and, sometimes, new terms into the governing equations. Obviously, the project leader must know which is the best suited software for the relevant application. However, many workshops, whose results are often publicly distributed, can aid to choose the proper CFD code and the best numerical approach (RANS, DNS, LES, etc...) to be used. A downside of such codes is generally found in their steep learning curve. Indeed, while commercial codes are often equipped with a graphical user interface (GUI), which is generally simple to use, the most part of open-source solvers does not employ any interface, which makes less intuitive to initialize a simulation. Moreover, in many cases the documentation of the solver is not adequate to properly understand how to set a simulation. This issue can be crucial for the practical use of these codes, which are often based on high-order schemes or innovative algorithms.

As a final remark, the high performance typically guaranteed by open-source solvers is associated, unfortunately, with a bigger training time for a non-expert user and an overall difficulty in designing a new simulation. Notwithstanding all the cited problems, however, the upsides belonging

to these codes often convince the researchers to consider them as the only way to obtain reliable simulations of the investigated phenomenon. Some of the most used open-source codes within the aerospace community are described below, with special reference to OpenFOAM and Nek5000, which are widely used in the present thesis work.

- OpenFOAM (Open source Field Operation And Manipulation) [59] is probably the leading open-source CFD code, due to its huge versatility and good performances. It is very used both in university research programs and in industries due to its fair reliability and effectiveness, if compared both with commercial and in-house codes. This code employs a large number of solvers, each one able to deal with incompressible/compressible flows, unsteady/steady simulations, multiphase systems, structural dynamics problems and others. On the other hand, pre- and post-processing can be made employing the utilities provided by the OpenFOAM software, which can be used to generate the computational mesh, check the quality of the grid, collect averaged and fluctuation data, interpolate the solution on another grid. OpenFOAM started as FOAM around 1993 at Imperial College, and written in C++. The spatial discretization of the governing equation is based on a finite-volume approach, generally employing first- and second-order discretization both in space and time. Several turbulence models can be selected for the simulation of turbulent flows, ranging from RANS to LES and hybrid RANS/LES.
- Nek5000 [3] has recently become a standard tool in high-fidelity direct numerical simulations of turbulent flows and stability calculations. The code has been developed and maintained by the Argonne National Laboratory, and it is based on the spectral element method (SEM) for the numerical solution of the Navier-Stokes equation. This method was first introduced by Patera [60] to combine the main advantages of finite element (geometric flexibility) and spectral methods (high-order resolution). The domain is partitioned in non-overlapping hexahedral elements, and the velocity and pressure fields are obtained as the combination of Lagrange polynomials, based on Gauss-Lobatto-Legendre (GLL) and/or Gauss-Legendre (GL) quadrature points. This code has been generally used for the direct numerical simulation of incompressible flows, however also natural convection, fluid-structure interaction and low-Mach prob-

lem can be handled by means of this code.

- SU² [61] is a tool suite developed by the Aerospace Design Lab of the Department of Aeronautics and Astronautics at Stanford University. The suite has been written in C++, and its primary purposes were to simulate external flows and solve shape optimization problems. However, the code has been recently extended to analyze more complex phenomena, becoming *de facto* a multi-physics solver, as explained in Economon *et al.*'s work [62]. The current release of SU² (v7 Blackbird) can deal with chemically reactive fluids, electrodynamics, potential flows by means of unstructured grids.
- Gerris [63] is a specialized code for the simulation of multiphase flows, developed by prof. Stéphane Popinet and supported by the Institut Jean le Rond d'Alembert. It adopts the Volume-of-Fluid method to solve incompressible, two-phase flow problems, using adaptive mesh refinement to achieve a high resolution in the neighbourhood of the interface. It also included an accurate modeling of the surface tension and electrohydrodynamics effects. This code has been recently replaced by Basilisk [64], which is developed by the same researchers, to handle more complex phenomena.
- Nektar++ [65], finally, uses high-order polynomial functions to achieve fast convergence rates. Differently from Nek5000, the code is based on a Spectral/hp discretization for the resolution of the incompressible Navier-Stokes system and the compressible Euler equations. The code has been successfully applied to investigate high-Reynolds-number turbulent flows and inviscid, transonic field around aerodynamic bodies.

As a final comment, it is worthwhile noting that Nek5000 has been extensively used to simulate the interaction between a jet and a crosswind, for example by Brynjell-Rahkola *et al.* [66] for the computation of boundary layer suction devices, by Peplinski *et al.* [67], who investigated continuous jets in crossflow, and Ezhova *et al.* [68] to perform LES of the interaction between a jet and a thermocline. Similarly, a great success has been achieved by the present code in simulating other flow control cases. Indeed, Loiseau *et al.* [69] and Bucci *et al.* [70] used Nek5000 to investigate the flow behind roughness elements, whereas Siconolfi *et al.* [71] accomplished a numerical study about micro-vortex generators. Nek5000

can be considered, therefore, one of the state-of-the-art approaches for the characterization of flow control techniques.

2.3 Low vs High-order numerical methods

The choice of the numerical code to be used for the numerical simulations is a key point for the success of a computational project. Several commercial and open-source codes are available for this purpose, based on low or high-order space discretizations of the Navier-Stokes equations. First or second-order discretizations based on finite-volume or finite-difference methods are generally employed by commercial codes, and are of widespread application due to their simplicity of use. On the other hand, high-order methods are mostly used by research and in-house codes, and often provide high-fidelity simulations and better numerical performance (in terms of reduced numerical dissipation, high spatial and temporal accuracy and high accuracy-to-cost ratio). These codes often rely on spectral-element and discontinuous Galerkin methods, which should combine the high flexibility guaranteed by the finite element method and the high accuracy of spectral techniques. Finally, the choice of the numerical solver must be also guided by information on the parallel performances of the numerical code and possible hardware-related issues.

To this aim, a series of direct numerical simulations has been carried out, using Nek5000 and the OpenFOAM native solver *pimpleFoam*, with the aim of investigating their capabilities in the simulation of synthetic jets. The present section summarizes the chosen computational setup and the main conclusions of the activity, whereas further results can be found in the journal article of Capuano *et al.* [72]. The present investigation is a follow-up of the works by Sprague [73] and Kooij *et al.* [74], who performed direct numerical simulations of a turbulent channel flow and turbulent Rayleigh-Benard convection, respectively, with both Nek5000 and OpenFOAM. The work was mandatory to properly choose the computational setup for the subsequent simulations, carried out during the doctoral period.

2.3.1 Computational model

The computational setup employed for the code comparison resembles the experimental conditions described by Yao *et al.* [75], whose results

will be used to evaluate the performances of OpenFOAM and Nek5000. The non-dimensional parameters of the experiments have been perfectly reproduced in the simulations: $\text{Re}_j^* = U_j^* h / \nu = 1150$ and a Strouhal number $\text{St}_j = 2\pi f h / U_j^* = 0.25$. Note that, for the present investigation only, the characteristic velocity $U_j^* = 2U_j$ has been used, to match the definition of the experimental case by Yao *et al.*. All these parameters strongly affect the performance of the SJ device, therefore a key point of the simulations is to obtain an a-posteriori accurate evaluation of the reference velocity. Obviously, this quantity is strongly dependent on the chosen computational solver and the numerical mesh, therefore a proper mesh independence study must guarantee the convergence of U_j^* or some related quantity.

Several assumptions have been made during the design of the numerical setup, which are described below. Firstly, incompressible solvers have been used to investigate the flow field generated by the SJ actuator. As it will be outlined in Sec. 3.3, the validity of this choice is strongly dependent on the Strouhal number of the experimental campaign. However, in the present case the actuator was driven at a frequency close to the structural resonance one, and sufficiently lower than the Helmholtz frequency of the cavity. Therefore, the flow can be considered as incompressible in the whole domain.

The actuator geometry considered in the simulations is also simplified, if compared to the experimental one. Following Kotapati *et al.*'s work [43], the domain used in the simulations is depicted in Fig. 5.1, along with the boundary conditions enforced on each boundary face. The domain includes the cavity, the orifice, and the external environment. The dimensions of the external domain are chosen, after a preliminary independence study, to be $L_x/h = L_y/h = 60, L_z/h = 9$, whereas the actuator geometry is modelled as a simple parallelepiped, of dimensions $l_c/h_c = 2.0, l/h = 2.6, h_c/h = 2.45$ and $L_z/h = 9$, following Kotapati *et al.* [43].

Moreover, differently from the experimental setup, both numerical studies consider the lower end of the cavity as the driving wall, whereas the moving diaphragm is located on the left boundary of the actuators in the experiments. Nonetheless, in a preliminary phase of the work the flow asymmetry has found to be negligible for the present computational phase, justifying the adopted simplification. Finally, the high aspect ratio of the slot orifice used in the experimental campaign ($AR = 28$) justifies the assumption of nominal homogeneous spanwise flow. As it will be ex-

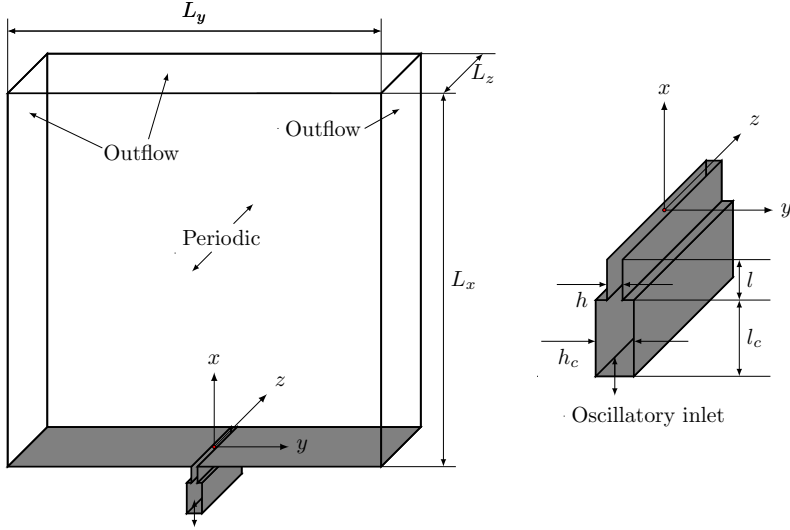


Figure 2.1: Computational domain and boundary conditions used in the numerical simulations. The gray patches are solid walls. An enlarged view of the cavity is shown in the right part of the figure.

plained in Sec. 3.3 the diaphragm motion is mimicked by an oscillatory Dirichlet condition for the streamwise velocity (Eq. (2.1)).

$$u(x = x_c, y, z, t) = U_w(y, z) \sin(2\pi ft), \quad (2.1)$$

A plug inlet $U_w = \text{const}$ is considered; the constant value of the streamwise velocity is obtained by enforcing the incompressible continuity equation between the lower end of the cavity and the orifice exit $U_0^* = (2/\pi)U_w(h_c/h)$. No-slip conditions are used for all the cavity walls and the external flat plate, while the external field faces are modeled as outflow boundaries, and periodic boundary conditions are applied for the z -normal faces. The flow is initialized in quiescent conditions, and twenty actuation cycles have been simulated. The last ten cycles are used to obtain time and phase-averaged velocity fields. Furthermore, both quantities have been also averaged along the (homogeneous) spanwise direction. Numerical results obtained by doubling the number of cycles confirmed that statistics are well converged after 10 accumulation cycles.

Four grids have been selected and used to describe the convergence of Nek5000 and OpenFOAM. The resulting test matrix is reported in

Table 2.3: Test matrix of the computational runs. The number of elements (Nek5000) and cells (OpenFOAM) along each direction refers to the external environment only. The final column reports the total number of degrees of freedom (DOF) for each case.

Solver	Acronym	L_x/h	L_y/h	L_z/h	N_x	N_y	N_z	#DOF
Nek5000	N1	60	60	9	13	12	4	592182
Nek5000	N2	60	60	9	19	18	6	1709514
Nek5000	N3	60	60	9	26	24	8	3953630
Nek5000	N4	60	60	9	32	30	10	7177860
OpenFOAM	OF1	60	60	9	120	120	36	655200
OpenFOAM	OF2	60	60	9	160	170	54	1674000
OpenFOAM	OF3	60	60	9	220	240	72	4075200
OpenFOAM	OF4	60	60	9	290	270	90	7389000

Table 2.3. All meshes have been obtained using the standard meshing tools provided by OpenFOAM (`blockMesh`) and Nek5000 (`genbox`).

It is worth noting that the resolution of DNS performed in [43] is comparable with the one used for the OF2 and N2 simulations. The grid is clustered in the slot area, along both the x and y directions, in order to obtain a good resolution of the turbulent motion in that region, even for the coarsest grid. To allow for a fair comparison, the number of cells for the OpenFOAM runs was obtained by multiplying the number of elements used in Nek5000 by the polynomial order.

As regards the numerical solvers, the native incompressible flow solver *pimpleFoam* has been selected for the OpenFOAM numerical simulations, whereas the version `r1115` of Nek5000 is used in this work. The former is based on a finite-volume approach, with both convective and diffusive terms approximated by second-order centered schemes. Time integration is achieved by a second-order Crank-Nicolson method. The solution algorithm is based on the PIMPLE algorithm, a slightly modified version of the PISO. The pressure linear system is solved by a generalized geometric-algebraic multi-grid (GAMG) method with a tolerance of 10^{-7} . On the other hand, the $\mathbb{P}_N - \mathbb{P}_{N-2}$ formulation is used in Nek5000, with $N = 9$ polynomials for the velocity field. Time integration is based on a high-order splitting method (BDF3-EXT3). A third-order extrapolation is used for the convective terms (EXT3), while the viscous term is treated implicitly. Two linear systems of equations arise: the pressure system is solved using a generalized minimal residual method (GMRES), while the linear

system for the velocity field is solved using the conjugate gradient method with Jacobi preconditioning. For both solvers, the tolerance is set to 10^{-7} .

2.3.2 Results and conclusions

The evaluation of the capability of Nek5000 and OpenFOAM in simulating synthetic jets was carried out by comparing both field variables and global quantities with their experimental counterparts. The analysis focused also on the parallel performances of the codes. A complete characterization of the time- and phase-averaged flow field, with useful comparison between Nek5000, OpenFOAM and experimental data can be found in the referenced work [72]. In this Section the main results are briefly summarized.

Firstly, time-averaged flow fields revealed that there are no significant differences in the computational results, except for the coarsest OpenFOAM grids. Indeed, as shown in Fig. 2.2, a remarkable agreement between numerical and experimental data is found, especially for the finest grids.

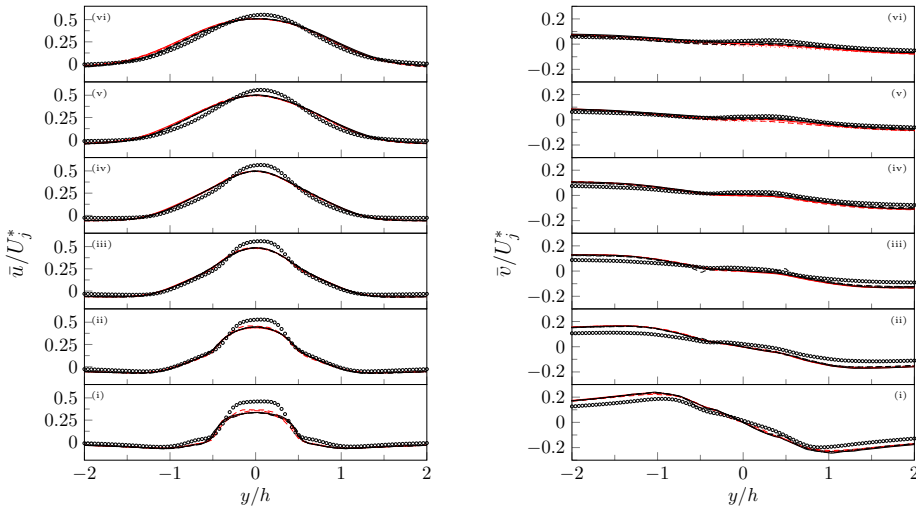


Figure 2.2: Crosswise distribution of time-averaged streamwise (left) and cross-stream (right) velocity at streamwise stations (i) $x/h = 0.5$, (ii) 1.0, (iii) 1.5, (iv) 2.0, (v) 3.0, (vi) 4.0. Lines refer to the Nek5000 (black) and OpenFOAM (red) computations on the coarse (dashed), medium (dashdotted), fine (solid) and very fine (dotted) grid levels; \circ PIV.

Similarly, crosswise profiles of phase-averaged streamwise velocity at

peak espulsion ($t/T=0.25$, Fig. 2.3(left)) obtained by DNS practically coincide with the experimental data. Conversely, at peak suction ($t/T=0.25$, Fig. 2.3(right)) some differences between OpenFOAM and Nek5000 arose: OF1 and OF2 cases are quite noisy, whereas velocity profiles from Nek5000 are smoother and rapidly collapse onto the experimental data for finer grids. However, both code converge to the experimental velocity profiles for the finest grid resolution (especially far from the orifice exit). This discrepancy led to a different time distribution of the saddle point position, which appears only during the suction phase and, as a consequence, is strongly dependent on the chosen computational case.

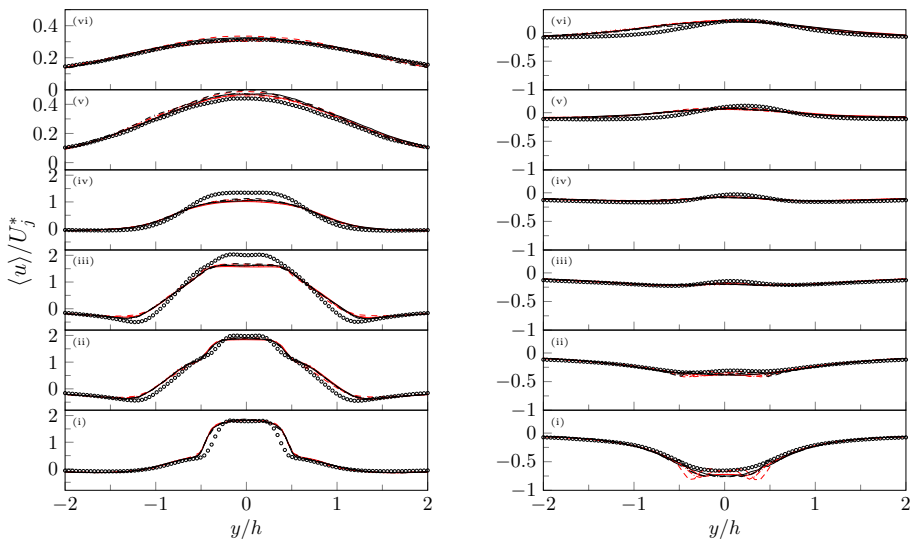


Figure 2.3: Crosswise distribution of phase-averaged streamwise velocity at maximum ejection (left) and maximum ingestion (right) phases at streamwise stations (i) $x/h = 0.5$, (ii) 1.0, (iii) 1.5, (iv) 2.0, (v) 3.0, (vi) 4.0. Lines refer to the Nek5000 (black) and OpenFOAM (red) computations on the coarse (dashed), medium (dashdotted), fine (solid) and very fine (dotted) grid levels; \circ PIV.

However, the biggest discrepancy between the two codes can be found by inspecting the turbulent behaviour of the flow (Fig. 2.4). In fact, while phase-averaged streamwise fluctuation at peak espulsion are in good agreement to each other (with small differences for cases N1 and OF1), OpenFOAM fails in capturing the actual behaviour of the flow at maximum ingestion, when the experimental data showed a partial remilaminarization of the flow. On the other hand, Nek5000 well predicts the reduction

in the streamwise turbulent intensity occurring during the suction phase, even for the coarser computations.

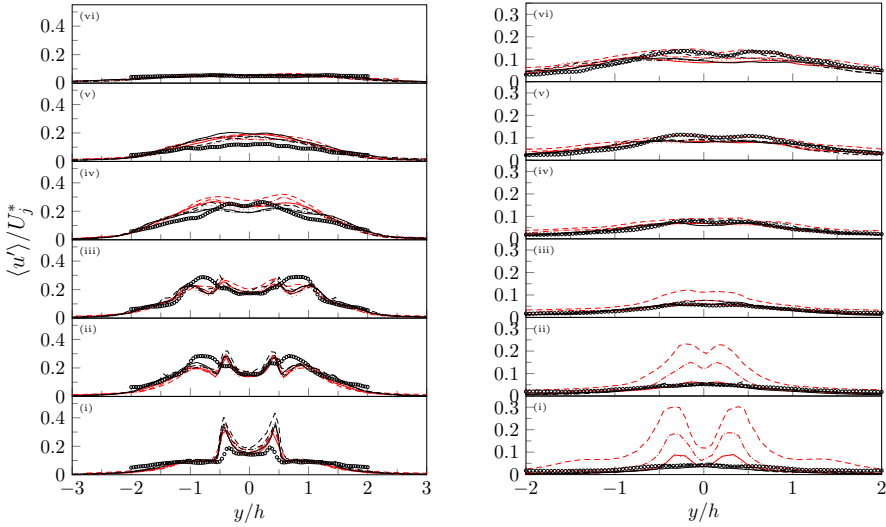


Figure 2.4: Crosswise distribution of streamwise r.m.s. velocity at maximum ejection (left) and maximum ingestion (right) phases at streamwise stations (i) $x/h = 0.5$, (ii) 1.0, (iii) 1.5, (iv) 2.0, (v) 3.0, (vi) 4.0. Lines refer to the Nek5000 (black) and OpenFOAM (red) computations on the coarse (dashed), medium (dashdotted), fine (solid) and very fine (dotted) grid levels; \circ PIV.

As a final comment, therefore, it can be stated that Nek5000 and OpenFOAM simulations are equally efficient in evaluating time-averaged velocity fields, whereas only Nek5000 is capable of obtaining the actual behaviour of the phase-averaged turbulent fluctuation along the entire cycle.

A second phase of the performance evaluation focused on the convergence of two global engineering quantities, as a function of the grid refinement level: the highest position of the saddle point x_{sp} during the actuation cycle and the stroke length L_j^* . Results are shown in Fig. 2.5: it is clear that the extremal position of the saddle point is correctly estimated also for the coarser grids, since its variation is small than the grid size. On the contrary, the stroke length variation provide useful information on the code convergence: indeed, while Nek5000 is able, at the finest grid, to reach grid independence, a non-negligible difference can be found between OF3 and OF4. This result constitutes a further evidence of the

faster convergence of the high-order code if compared with OpenFOAM. It is worth noting that both simulation cannot converge to the analytical value of 12.5, which is obtained if the phase-averaged velocity is averaged over the entire exit plane. The stroke length here defined is based on the centerline velocity, which is significantly higher than the average velocity for the present case (the ratio between those velocities depends mainly on the jet Stokes number).

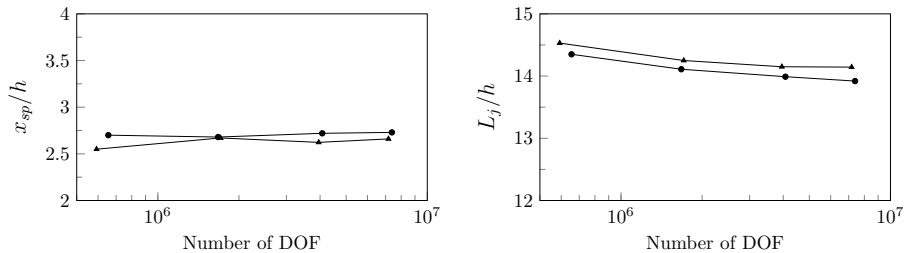


Figure 2.5: Saddle point x_{sp} and stroke length L_j as a function of grid refinement. Triangle is for Nek5000, circle for OpenFOAM.

Two more tests have been carried out, to ascertain which is the most performing approach for SJ simulations. First, the performance of the linear solvers of the codes are investigated by analyzing the variation of the CPU time per time step as a function of the total number of degree of freedoms 2.6 (right). As expected, the computational effort scales linearly with the total number of DOF for both Nek5000 and OpenFOAM. Finally, a strong scaling test has been carried out in order to investigate the parallel performances of the codes. The test was performed on CINECA supercomputer Marconi, whose characteristics can be found on the CINECA website [76]; N3 and OF3 cases has been considered for this purpose. Results are shown in Fig. 2.6 (right). At the lowest number of processors, $N_p = 34$, OpenFOAM takes roughly 2/3 of the time with respect to Nek5000 to perform a single time step. On the other hand, the parallel performances of OpenFOAM decline quickly, leading to speedup flattening at $N_p = 272$, where the computational load per processor is of roughly 15000 cells/processor. In contrast, Nek5000 scales quite well up to $N_p = 544$, which was the maximum number of processors tested in this study.

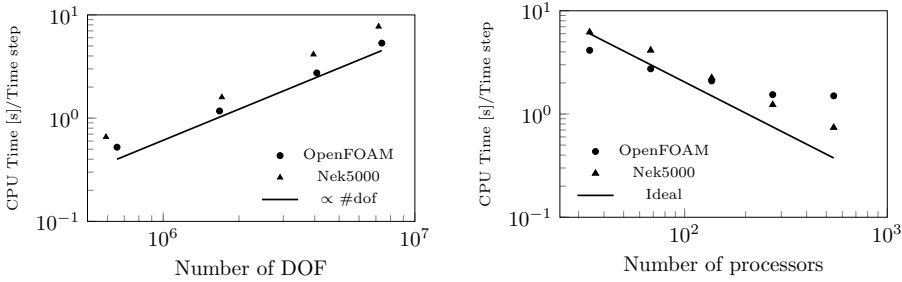


Figure 2.6: Computational performances of OpenFOAM and Nek5000. (left) Elapsed CPU time per time step for the three cases of Table 2.3 on 68 processors; (right) elapsed CPU time per time step for the cases OF3 and N3 as a function of the number of processors.

2.3.3 Final remarks

The present analysis allowed to state that, if high-fidelity velocity fields and fluctuations are required, Nek5000 is more efficient than OpenFOAM in the simulation of synthetic jets. This finding provided useful guidelines for the use of these open-source solvers to investigate the flow field generated by such devices, both in quiescent conditions and in presence of a crossflow. Indeed, as reported in Chapters 4 and 5, both codes have been massively used throughout the doctoral work: in particular, OpenFOAM resulted adequate for the simulations shown in Chapter 4, whereas Nek5000 has been chosen for the simulations of synthetic jets issuing in boundary layers. The main reason why OpenFOAM has been employed to gain physical insights about the flow generated by multi-slotted and multi-orifice actuators is its simplicity in generating and handling complex grids. It must be considered, indeed, that the generation of a structured grid can actually be the bottleneck activity during the execution of a CFD activity if complex geometries are involved; the use of the `blockMesh` utility allowed to obtain all the desired computational meshes in a reduced time, while the `checkMesh` command permitted to check both the quality of the generated grid and the presence of errors during the grid generation process. It must be noted, moreover, that all the OpenFOAM computations have been focused on the vortex trajectories and the streamwise evolution of the jets, rather than on (possible) secondary instabilities of the vortex structures and their subsequent transition to turbulence.

On the other hand, Nek5000 was deemed the best choice for the inves-

tigation of synthetic jets in crossflow, for which a parametric analysis (in terms of the SJ actuation frequency, the inlet boundary layer Reynolds number and freestream turbulence intensity) has been carried out. All the simulations have been performed using a simplified geometry, since the synthetic jet is injected into a boundary layer through a circular pipe, thus neglecting the effect of the cavity geometry on the resulting flow field. More importantly, the boundary layer transitions to turbulence while moving in the streamwise direction (due to the presence of the jet), and both the beginning and the extent of the transition region were considered crucial features in determining the SJ performance. The high efficiency and accuracy guaranteed by Nek5000 has permitted to get high-fidelity evaluation of these parameters.

Chapter 3

Experiment-based design of synthetic jets

The design of synthetic jet actuators in quiescent conditions is often tackled using Lumped Element Models. LEMs are already available for several SJ configurations: a review of the main lumped-element approaches has been made by Chiatto *et al.* [77] for piezo-driven SJs, and by Zong *et al.* [78] for plasma SJs. A low-dimensional model of thermo-acoustic synthetic jet actuators has been recently derived by Chen *et al.* [29]. In the following section the lumped element model for plasma synthetic jet actuators is outlined, along with some original considerations about the efficiency performances of the jet. Sec. 3.2 is devoted, instead, on the development of a LEM-based approach for the performance evaluation of piezo-driven synthetic jet actuators. Finally, Sec. 3.3 concerns the usage of the LEM output to gain information about the whole external flow field generated by the device in quiescent conditions.

3.1 A calibrated LEM for plasma synthetic jet actuators

A lumped element model for the design of plasma synthetic jet actuators has been recently developed by Chiatto and de Luca [79], and refined in a following work [80] during the doctoral period. The LEM allowed to investigate both single pulse and repetitive regimes, providing insights on the major actuation characteristics. A brief summary of the model

and its experimental calibration is outlined in the present section; further information can be found in the aforementioned studies.

3.1.1 The lumped element model

The PSJ device is modeled as a cylindrical cavity, with an internal volume V_c , and a nozzle, whose length and diameter are l and d . The governing equations are based on the lumped assumption, and the air involved within the cavity is considered at local thermodynamic equilibrium. The cycle is schematized as a sequence of three stages, energy deposition, discharge and refresh phases.

Energy Deposition

Within the LEM model, if the discharge time is very short the energy deposition can be considered as instantaneous. If this assumption holds, this phase can be considered as a constant specific volume process: the state variables, ρ , T and p (air density, temperature and pressure) after the spark can be computed as follows

$$\begin{cases} \rho_{ci+1} = \rho_{ci} \\ T_{ci+1} = T_{ci} + E_f / (M_{ci} c_v(T_{ci})) \\ p_{ci+1} = \rho_{ci} R(T_{ci+1}) T_{ci+1} \end{cases} \quad (3.1)$$

where i and $i + 1$ stand for, respectively, the time instants before the arc formation process and after the spark, $R(T)$ is the air gas constant, which is temperature-dependent as it includes compressibility effects. The subscript c refers to all the quantities computed within the cavity; whereas the subscript e to those evaluated at the nozzle exit. E_{tot} is total amount of energy provided by the power supply system; $E_f = \eta_{tot} E_{tot}$ is the effective amount of energy supplied to the fluid, M_c is the air mass and c_v the constant volume specific heat. It is worthwhile noting that η_{tot} is the total efficiency of the jet, which includes all the losses due to parasitic resistance and inductances and the non-uniform heating effects of the arc discharge. This parameter is used, in the following experimental characterization, as a fitting parameter for the model.

Discharge and Refresh Phases

During this phase the high-pressure and high-temperature fluid exhausts through the orifice of the PSJ actuator, converting its internal energy into the kinetic one. This phase can be simulated as the discharge process of a reservoir connected to the external ambient by means of a relatively short nozzle, or orifice. Conservation of mass and total energy can be enforced:

$$\frac{d\rho_c}{dt} = -\frac{\rho_e U A_e}{V_c} \quad (3.2)$$

$$\left[\rho_c \frac{d}{dt}(u_c) + u_c \frac{d}{dt}(\rho_c) \right] V_c + \rho_e \left(h_e + \frac{U^2}{2} \right) U A_e + \dot{Q} = 0 \quad (3.3)$$

where U indicates the exit velocity, A_e the orifice area, t the time, u and h the energy and thermodynamic enthalpy, and \dot{Q} is the heat power exchanged through the entire surface of the system. It is worth noting that Equation (3.3) is valid only for $T_d = O(1e^{-6})$ s; otherwise the energy deposition cannot be considered a constant volume process, because the ejection and the heating processes occur simultaneously. In this case, the energy deposition cannot be modeled as an independent process, but it should be treated as a jet stage with both heat input (arc energy discharge) and output (heat losses through the actuator walls) terms [81]. By combining Eqs. (3.1) and (3.3), it is possible to obtain:

$$\left[\rho_c \frac{d}{dt}(u_c) + u_c \frac{d}{dt}(\rho_c) \right] V_c + \rho_e \left(h_e + \frac{U^2}{2} \right) U A_e + \dot{Q} - \frac{E_f}{T_d} = 0 \quad (3.4)$$

Finally, the application of the compressible unsteady Bernoulli's equation, between a point inside the cavity (where the flow velocity is practically null) and the exit section of the nozzle, yields a third equation for these phases:

$$u_c + \frac{p_c}{\rho_c} = u_e + \frac{p_e}{\rho_e} + l_e \frac{\partial U}{\partial t} + K \frac{|U| U}{2} \quad (3.5)$$

where K is the head loss coefficient, including entrance/exit losses at exit orifice; l_e is the modified effective length, representing the distance between the two points of application of Bernoulli's equation. In the present case,

both the head loss coefficient and the modified effective length have been estimated via numerical simulations, obtaining $K = 1.78$ and $l_e/d = l/d + 1.5$. The computational setup and the post-processing of the simulation data are shown in [79].

Another convenient equation for the flow along the nozzle is the classic isentropic relationship linking the thermodynamic properties inside the cavity to those at the orifice exit:

$$T_c = T_e \frac{c_p(T_e)}{c_p(T_c)} \left[1 + \frac{\gamma(T_e) - 1}{2} M_e^2 \right] \quad (3.6)$$

with γ being the specific heat ratio, which is considered as a function of the temperature for real gases. Two more equations must be imposed, in order to close the problem. First of all, the exit condition must be given: depending on the ratio between the cavity pressure and the exit one, the flow can be choked or unchoked. If the pressure ratio, after the energy deposition, is greater or equal than its critical ratio, the flow is choked, otherwise an unchoked regime is assumed. For choked flow, sonic conditions (Eq. (3.7)) must be imposed at the nozzle exit, whereas a Kutta condition $p_e = p_a$ is enforced if the flow is unchoked.

$$M_e = \frac{U}{\sqrt{\gamma(T_e)R(T_e)T_e}} = 1 \quad (3.7)$$

Finally, the total heat power \dot{Q} , which is included in the energy balance, must be defined. It is considered as the sum of two quantities, one related to the external natural convection mechanism, the other due to the radiative heat transfer.

$$\dot{Q} = \dot{Q}_{conv} + Q_{rad} = h_{conv} S_{conv} (T_c - T_a) + \varepsilon \sigma S_{rad} (T_c^4 - T_a^4) \quad (3.8)$$

where S_{conv} and S_{rad} are the exchange surface and the relevant surface of emission, respectively, h_{conv} is the convective heat transfer coefficient, T_a is the external ambient temperature, ε is the emissivity coefficient (in the case of ceramic material it is equal to about 0.8) and σ is the Stefan-Boltzmann constant. Note that here the cavity wall is supposed to constitute a vanishing thermal resistance, which is validated by the occurrence of a very small Biot number.

3.1.2 LEM calibration

The presented LEM can be calibrated by comparing the experimental data and the LEM computations of the time-averaged total pressure and velocity; the total efficiency of the device is assumed as the fitting parameter of the model. Therefore, total pressure and velocity measurements must be acquired, for different values of the actuation frequency and the discharge energy. It must be preliminary observed that the fitting parameter η_{tot} not only contains information on the actual device efficiency, but includes some modeling and experimental uncertainties, related also to the used measurement technique.

As regards the experimental measurements, a plasma synthetic jet actuator, mainly composed of a two-part case in MACOR has been designed and manufactured. The actuator cavity has a cylindrical geometry (6 mm in diameter and 6 mm high) with an orifice of 1 mm in diameter and 2 mm in length. The electrodes, with a diameter of 1 mm and placed at a distance of 1.5 mm, are located in the bottom part via through holes and blocked with a non-conductive bond, making a replacement extremely easy. More information about the supply system and the actuator operation can be find in the full paper [80]. The set of experimental data consists in total pressure data, obtained using a home-made Pitot tube, with a 0.6 mm external and a 0.4 mm internal diameter, and placed 1 diameter downstream of the nozzle exit (as shown in Fig. 3.1). The Pitot tube is connected with a Mouser sensor pressure transducer (range: ± 5 in H_2O , accuracy: 0.25%), whose output signal has been acquired with a data-acquisition system (USB Instruments DS1M12 or “Stingray”).

Time-averaged data is computed by averaging the acquired signal for 10 s, assuming that the reference pressure is equal to the ambient one. As the discharged energy in the present experimental campaign is relatively small, the classic Bernoulli equation can be used. The measure of the actuator external temperature with a FLIR SC6000 Series Infrared Camera (Flir, Wilsonville, Oregon, USA) has allowed a good estimation of the actual air density to be used in the post-processing phase, with a uncertainty estimation of about 6%, computed with the standard procedures of literature.

The total pressure measurements allow to obtain streamwise velocity distributions in the radial direction, depicted in Fig. 3.2 for different values of the discharged energy E_d and fixing both the actuation frequency and the duty cycle to $f = 500\text{Hz}$ and 10%. In the chosen range of E_d , the

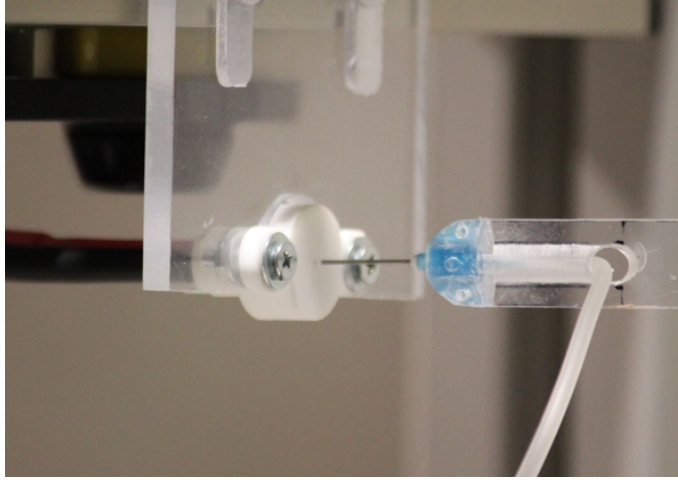


Figure 3.1: PSJ actuator with the Pitot probe.

jet peak velocity seems to increase almost linearly. The shape of the velocity profiles is strongly dependent on the Stokes number, which in turn is proportional with the kinematic viscosity of the air. The latter quantity increases with E_d , therefore the Stokes number reduces with the discharge energy. This fact explains the change from top-hat to near-parabolic shaped velocity profile as E_d is increased.

As regards the numerical results, LEM simulations were performed for 80 actuation cycles (usually the device reaches a periodic behavior after 20/25 cycles); a mean total pressure value was computed at the last cycle of the simulation considering the ejection phase only, as explained in Zong *et al.* [82]. The best fit between numerical and experimental data yields the value of $\eta_{tot} = 0.45$.

At this stage, the tuned model is able to predict the PSJ performances. Fig. 3.3 shows a comparison between the numerical jet mean velocity, obtained using the total pressure data, and the experimental measurements acquired at the centerline of the jet. More precisely, the jet velocity has been experimentally evaluated 1 diameter away from the nozzle exit, where the velocity peak should be approximately located. This assumption impacts on the efficiency evaluation, which is basically a conventional estimation. The LEM model is able to predict, with a good accuracy, the jet mean velocity as a function of actuation frequency and discharged energy: the numerical data predict an almost linear behaviour of the jet velocity

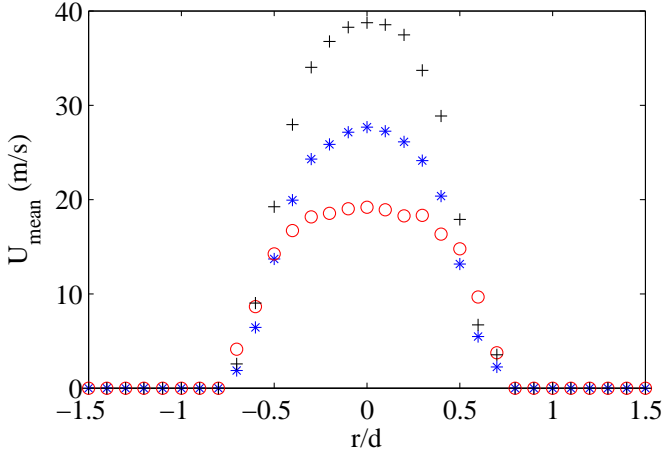


Figure 3.2: Jet velocity profiles in the radial direction for different discharged energy. Red markers are the results for $E_d = 1.2$ mJ ($S = 12.36$), blue ones for $E_d = 2.1$ mJ ($S = 11.01$), and black ones for $E_d = 3.4$ mJ ($S = 9.96$).

with the discharge energy (except for low values of the energy), and an increasing trend with the actuation frequency.

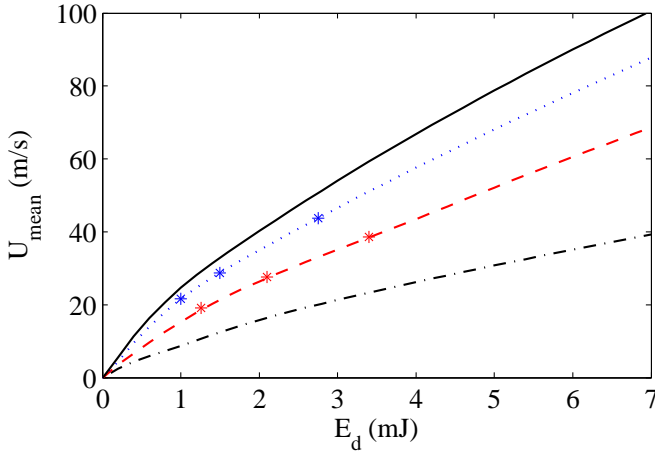


Figure 3.3: Mean flow velocity as a function of the discharged energy and the actuation frequencies. Black solid line: $f = 1000$ Hz; blue dotted line: $f = 750$ Hz; red dashed line: $f = 500$ Hz; black dashed-dotted line: $f = 250$ Hz. Star markers represent experimental data.

3.2 LEM-based design approach for piezo-driven SJs

Several lumped element models for piezo-driven synthetic jets are already available from literature; these methods allow to obtain the frequency response of the actuator, with a fair accuracy and in a short time. However, after evaluating the natural frequencies of the actuator, a practical need in many applications is to ascertain that the jet really forms in such conditions. As a consequence, the LEM approach should be coupled with other criteria, to verify that the designed actuator is able to provide a strong jet at the chosen actuation frequency (which, in turn, is related to the characteristics of the flow to be controlled, in terms of reduced frequency and momentum coefficient).

Several formation criteria can be found in the specialized literature, based on different conditions to be satisfied by the device parameter. Holman *et al.* [83] stated that a jet forms when the self-induced velocity of the vortices generated during the ejection phase is bigger than the jet velocity during the suction phase. The original formulation of the Holman's criterion reads

$$St_0^{-1} > C \quad (3.9)$$

where C is a constant, which depends on the geometrical characteristics of the orifice: for axisymmetric orifices $C \simeq 0.08$. Holman's Eq. (3.9) provides the minimum air ejection velocity, \bar{U}_{min}

$$\bar{U}_{min} = Cd\omega \quad (3.10)$$

necessary for the jet formation at a certain operation frequency. This equation can be employed to distinguish between jet and no-jet conditions. However, several other works have been subsequently published, aiming at including more details of both device geometry and flow regime into Eq. (3.9). Timchenko *et al.* [84] obtained a new threshold, valid for low Stokes numbers ($S < 7$), by extending the previous analysis including viscous effects. Milanovich and Zaman [85] carried out systematic tests on various geometrical configurations, and found a formation threshold $St_0^{-1} > 0.04$, lower than that the one proposed by Holman *et al.* [83]. Zhou *et al.* [52] first introduced explicitly the viscous effects within the jet formation criterion. They individuates two boundaries: that of no jet/jet with no roll-up of vortices, and the one of jet with no roll-up/full jet with roll-up of vortices. For high L (approximately $L > 6$), the former

threshold is governed by viscous effects alone, i.e. the jet is not observable for $S < 2.5$, whereas for high S numbers ($S > 30$) the effect of the viscosity vanishes, and the Holman's law is recovered. Trávníček *et al.* [86] deeply investigated the high Stokes number field ($73 < S < 292$), finding that for the moderate range of $S < 160$ the formation threshold is rather close to the Holman's law, while for higher Stokes numbers, a gradual shift toward the threshold proposed by Milanovich and Zaman [85] is evident. Broučková *et al.* [87] summarized the huge amount of data available in the literature in a comprehensive graphical presentation in the $Re - S$ plane.

From a design perspective the presented formation criteria has to be supported by predictive tools, which provide the expected jet velocity as a function of the actuation frequency and other parameters of the actuator. Hence, to predict the jet formation the design velocity has to be compared with the minimum velocity given by Eq. (3.10). The purpose of the present work, therefore, consists of furnishing predictive tools of the SJ formation, as well as recovering part of the aforementioned thresholds from the literature with the aid of experimental evidence and LEM approach, which predicts the (resonance) amplifications of the Helmholtz and diaphragm oscillators of the actuator. General relationships for the minimum velocity of formation will be considered, starting from the general boundary correlation $Re = AS^\beta$ of Broučková *et al.* [87], with A and β being two suited constants.

3.2.1 Experimental measurements

An extensive experimental campaign has been carried out to investigate the jet formation. Hot-wire measurements have been obtained, basically placing the sensor one diameter downstream of the orifice exit, to measure the peak jet velocity, U_{max} , which is intrinsically predicted by the LEM approach; data acquired at farther locations has been used to investigate the jet formation. Moreover, another series of measurements has been specifically made by varying the normal-to-orifice distance of the probe in order to detect the saddle point position. Various actuators, realized in-house (whose characteristics are described in Table 3.1), with a brass shim and one or two orifices, were experimentally analyzed. The actuation frequency was systematically varied between 0 to 2500 Hz, corresponding to Stokes numbers ranging from 10 to 65.

The main experimental results are briefly summarized in the following, with reference to the single-orifice cases. Fig. 3.4 shows the frequency

Table 3.1: Geometrical characteristics of the tested actuators.

Parameter	Value
Cavity diameter, D/d	21
Cavity height, H/d	0.75, 1.50, 2.25, 3.00, 3.75
Orifice height, h/d	1
Orifices distance, e/d	0, 12.5

Table 3.2: Mechanical properties of shim and piezo-electric element. Subscript (*) stands for “s” and “p”, indicating the shim and the piezo-electric element, respectively.

	Thickness $th_{(*)}/d$	Diameter $D_{(*)}/d$	Young’s Module (Pa)	Poisson’s Module	Density (Kg/m ³)
Shim	0.1	21	$9.7 \cdot 10^{10}$	0.36	8490
Piezo	0.0955	15.9	$6.6 \cdot 10^{10}$	0.31	7800

response of the actuators, in terms of the peak jet velocity measured at the orifice exit, for different cavity heights. At low frequencies all the curves collapse onto the incompressible solution (blue straight line), $U_{inc} = (A_w/A_0)\omega\Delta x_w$, which represents the static solution of the equivalent spring-mass system describing the dynamics of the actuator. It is worthwhile noting that the Helmholtz natural frequency shift towards lower values as the cavity height increases, whereas the structural frequency is almost independent of the cavity height, showing a slight shift towards lower values due to the decreased coupling factor between the two oscillators. This effect has been already observed in Chiatto *et al*’s work [77].

Experimental measurements can be also compared with the frequency response predicted by the lumped element model: Fig. 3.5 shows that a good agreement between numerical and experimental data is achieved, especially for the resonance frequency predictions. However, for moderate to high values of the actuation frequency, the model overpredicts the jet exit velocity; it is interesting to observe that, in these frequency ranges, the jet is not forming, whereas the LEM predicts a nonzero exit velocity. This issue could be solved during the design procedure by coupling the lumped model with one of the aforementioned formation criterions.

An effective way to correlate the present experimental results with the formation criterions is to depict the frequency response in non-dimensional

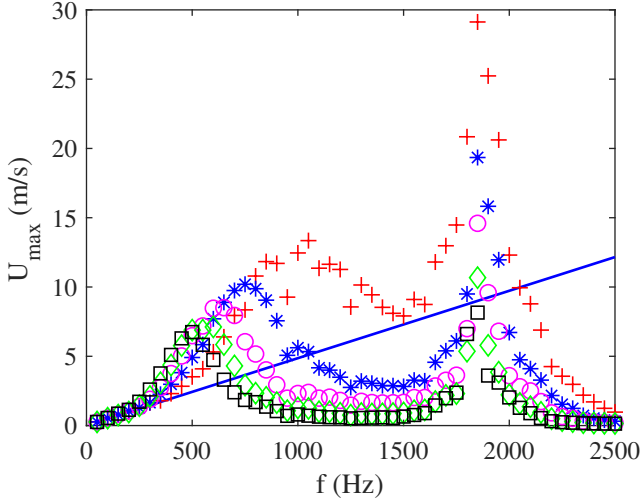


Figure 3.4: Frequency response of the brass single-orifice actuator in terms of peak jet velocity at the orifice exit, for different cavity heights. Red cross represents the $H/d = 0.75$ case; blue star $H/d = 1.5$; magenta circle $H/d = 2.25$; green diamond $H/d = 3$; black square $H/d = 3.75$. The blue continuous line is the incompressible solution.

form, in the $S - St_0$ plane (Fig. 3.6). The stroke length, which is inversely proportional to the jet Strouhal number, is also reported. This plot clearly highlights the jet formation region in terms of Stokes and Strohal numbers, which is bounded by the Holman’s criterion Eq. (3.9) (with $C = 0.08$) and the asymptotic threshold for low Stokes numbers of $S > 2.5$. Moreover, as proposed by Zhou *et al.* [52], and Broučková *et al.* [87], the two asymptotic limits can be linked to each other by the best fit trend $St_0^{-1} = 4.1 \cdot S^{-1.61}$, representing the boundary between no jet and jet formation without roll-up (black dashed line). However, it is worthwhile noting that there are several data points that are below the Holman’s horizontal limit. Moreover, it can be also observed that the jet exit velocity (represented by St_0^{-1} in the present figure) does not abruptly vanish when crossing the Holman’s threshold, but all the frequency responses gradually reach a null value.

It seems, therefore, that the jet is almost forming for any value of H/d and f , which seems to violate the jet formation criteria. However, this apparent contradiction can be solved if velocity measurements are collected

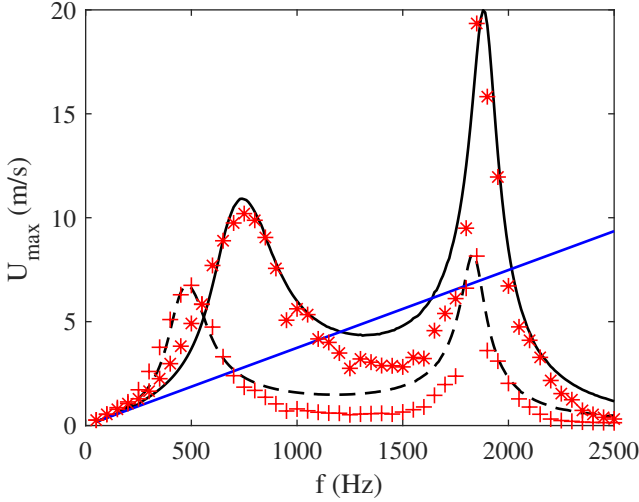


Figure 3.5: Comparison between the experimental data and LEM for $H/d = 1.5$ and 3.75 cases. The black dashed line and the red cross markers refer to the LEM and the experimental data, respectively, for the $H/d = 1.5$ case. The black continuous line and the red star markers are for $H/d = 3.75$ case. The blue continuous line is the incompressible solution.

downstream of the extremal position of the saddle point. Fig. 3.7 depicts its position as a function of the Stokes number, along with the stroke length trend. The saddle point maximum distance from the actuator exit plane is found to be decreasing as the actuation frequency is increased, whereas for low operating frequencies and large values of the stroke length it fades away from the orifice exit. The latter situation occurs at the Helmholtz resonance frequency, where the stroke length exhibits a relative maximum. It is worthwhile noting that for frequencies ranging in between the two resonance values and for very high frequencies, data points of saddle point location are not reported, because the formation criterion is not satisfied.

The subsequent step of the research, therefore, has been to verify these observations, by taking the same velocity measurement also one diameter downstream of the orifice exit (which is certainly beyond the saddle point for all the investigated frequencies). In this position, the vortex ring is fully formed and the probe reflects its passage only; therefore, in case of no jet formation, a null peak velocity would be obtained. Of course, the velocity evolution calculated by LEM code at the orifice exit should match

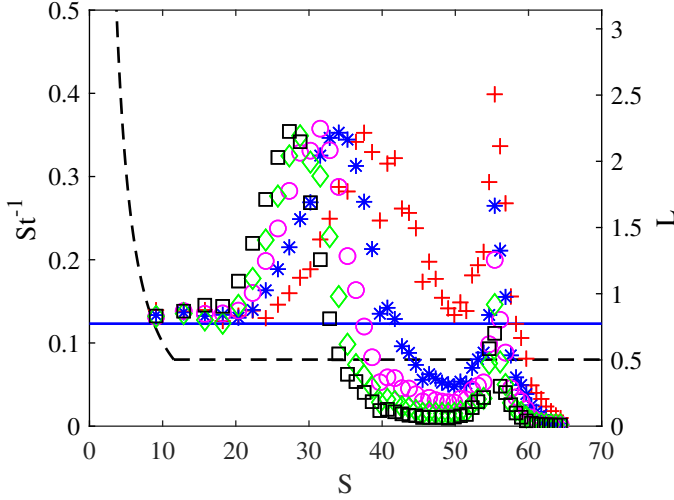


Figure 3.6: Frequency response of the brass single-orifice actuator in the $S - St$ plane, for different cavity heights. Red cross represents the $H/d = 0.75$ case; blue star $H/d = 1.5$; magenta circle $H/d = 2.25$; green diamond $H/d = 3$; black square $H/d = 3.75$. The blue continuous line is the incompressible solution; the black dashed line indicates the formation threshold.

the corresponding experimental data. These findings can be observed in Fig. 3.8, reporting the experimental measurements and the LEM data of dimensionless $u(t)/\bar{U}$ (where $u(t)$ is the instantaneous jet velocity) for the $H/d = 3$ case, at a frequency of $f = 500$ Hz. The peak velocity measured 1 diameter downstream of the orifice section, for the $H/d = 2.25$ case (red star), is shown in Fig. 3.9, together with previous data taken at the orifice (blue cross). It is interesting to observe that, when the Holman's criterion is not satisfied, the velocity measured beyond the saddle point quickly drops to zero, whereas a slow variation is observed in the formation region only.

3.2.2 Linking jet formation and LEM results

The final step of the activity has been to compare quantitatively the minimum velocity for jet formation criteria and LEM results, taking also advantage of the experimental results. The former quantity, according to Eq. (3.9), varies linearly with the frequency; other formulations can be

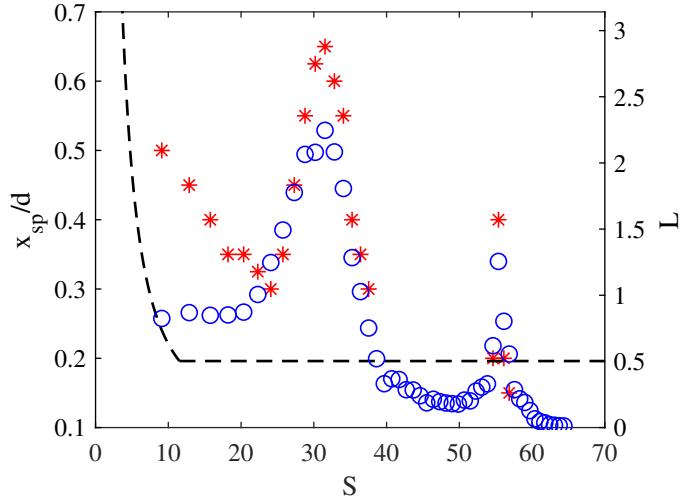


Figure 3.7: Non-dimensional saddle point position (red star markers) and stroke length (blue circle markers) as a function of the Stokes number. $H/d = 2.25$ case.

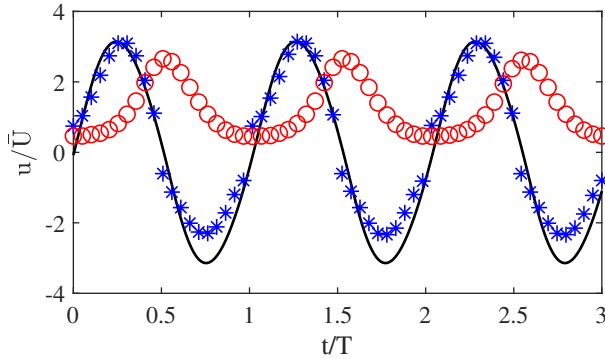


Figure 3.8: Comparison of instantaneous jet velocity experimental data and LEM prediction. The blue markers represent the measurements at the orifice exit, the red ones 1 diameter downstream; the black continuous line is the LEM prediction. $H/d = 3$ case, $f = 500$ Hz.

followed to have more general relations between U_{min} , d and ω , as the one by Broučková *et al.* [87].

$$U_{min} = Ad^{\beta-1}\nu^{1-\beta/2}\omega^{\beta/2} \quad (3.11)$$

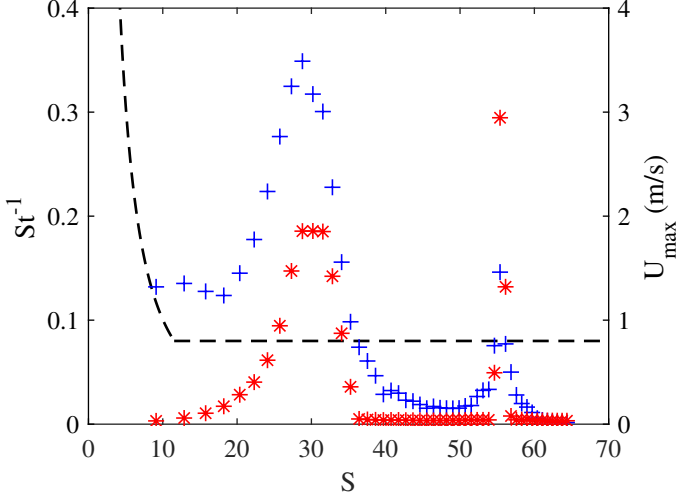


Figure 3.9: Frequency response of the brass single-orifice actuator in terms of peak jet velocity one diameter downstream of the orifice exit (red markers), together with the corresponding data at the orifice exit (blue markers); $H/d = 2.25$. The black dashed line indicates the formation boundaries.

For relatively low frequencies, it is quite straightforward to combine LEM results with Holman’s criterion. Indeed, in this condition the incompressible solution approximately holds, as long as the Strouhal number based on the fluid sound speed, $St_c = \omega H/c$, is very small. Taking into account the incompressible velocity definition, the following equation can be derived:

$$\left(\frac{D}{d}\right)^2 \frac{\Delta x_w}{d} > 0.08 \quad (3.12)$$

with D being the diaphragm diameter. The previous experimental campaign has shown that this constraint is satisfied for the single orifice device.

For higher frequencies, instead, the incompressible model cannot be used, therefore the amplification factor, defined by Eq. (3.13), must be evaluated:

$$\frac{U_{\max}}{U_{\text{inc}}} = \frac{1}{\sqrt{\left[2\zeta_w \frac{\omega}{\omega_w} \delta_H + 2\zeta_U \frac{\omega}{\omega_H} \delta_{CF}\right]^2 + \left[\delta_1 \delta_2 + 4\zeta_w \zeta_U \frac{\omega}{\omega_w} \frac{\omega}{\omega_H}\right]^2}} \quad (3.13)$$

where $\omega_w = \sqrt{k_w/m_{wt}}$ represents the uncoupled (first mode) natural frequency of the structural oscillator, $\omega_H = \sqrt{k_H/m_a}$ is the Helmholtz frequency, with k_H and m_a being the equivalent stiffness of the air inside the cavity and the effective mass of the air at the orifice, and $\omega_{wc} = \sqrt{k'_w/m_{wt}}$ represents the natural frequency of the spring made of the air enclosed within the cavity volume, whose stiffness is k'_w , and the oscillating diaphragm mass m_{wt} . In addition, $\delta_{(\cdot)} = \left(1 - \omega^2/\omega_{(\cdot)}^2\right)$, $\delta_{CF} = (1 + CF - \omega^2/\omega_w^2)$, and CF is defined as the *coupling factor* of the two oscillators, $CF = \omega_{wc}^2/\omega_w^2$. Moreover, ζ_w and

$$\zeta_U = \frac{KU_{\max}}{2\omega_H\ell_e} \quad (3.14)$$

are the non-dimensional structural and fluid dynamic (or acoustic) damping factors, respectively, with K being the (minor) head loss coefficient and ℓ_e the effective orifice length.

When the operation frequency lies in between the resonance frequencies, it is possible that the predicted jet velocity falls below the minimum value established by the formation criterion; this happens for all H/d values considered in the previous section except the $H/d = 0.75$ case. Moreover, for devices with relatively long pipes, the fluidic damping coefficient, ζ_U , must include also distributed head losses: within the LEM formulation it can be obtained as $16\nu/d^2\omega_H$. One can argue that when the *overdamped condition* is verified at the Helmholtz's frequency, namely $\zeta_U \geq 1$, the amplitude of the acoustic oscillator is not amplified with respect to the incompressible solution, and the jet could not be experimentally observable. The overdamped condition is:

$$\frac{\bar{U}}{\omega_H d} \geq \frac{Re}{16} \quad (3.15)$$

which in turn becomes:

$$S \leq 4 \quad (3.16)$$

where the equality holds for the critically damped case.

It must be noted that the present result is a boundary for the overdamped behaviour, not a jet formation criterion. As a principle, the jet can still form for $S < 4$, but its velocity is lower than the corresponding incompressible solution. Moreover, further decreases in the Stokes number would lead to a greater reduction of the amplification factor and, eventually, to the no jet occurrence. This result is consistent with the analysis

of Zhou *et al.* [52], and it is an evidence of the validity of the present approach. For the cases of devices making use of orifices, the Stokes number practically ranges from 40 to 100 and the only one effect limiting the jet formation is due to the kinematic one, as well established by the Holman's criterion.

As a final case, it must be considered that the overdamped condition could also occur in the case of cavity with exit orifice, where the no amplification condition is given by:

$$\frac{\bar{U}}{\omega_H d} \geq \frac{1}{K} \frac{2 \ell_e}{\pi d} \quad (3.17)$$

where, for sine jet velocity time trend, $U_{max} = \pi \bar{U}$. Combining the Holman's criterion with the overdamped condition, one finally obtains the range of Strouhal numbers for the jet formation without overdamped condition, at the Helmholtz resonance:

$$0.08 < \frac{\bar{U}}{\omega_H d} \leq \frac{1}{K} \frac{2 \ell_e}{\pi d} \quad (3.18)$$

where the minor head losses coefficient K depends on the geometry of the exit orifice and its machine finish. Several estimations of K can be found in literature: Sharma [88], based on the data of Gallas *et al.* [89], assumed $K = 0.78$, whereas for the present actuator $K = 1.14$ is chosen. Since $2\ell_e/(\pi d) \approx 1$, the reciprocal of Strouhal number is fully less than $1/K = 0.88$, and the Helmholtz peak has been always observed in all the present experimentals. However, it is possible in some applications that also the Helmholtz peak is not visible (as in case 2 of Gallas *et al.*'s work).

3.3 Obtaining full-field data from LEM output

As explained before, a complete characterization of the entire external flow field cannot be obtained directly from LEMs, even in quiescent conditions. One possible approach to gain information about the motion induced by the jet on the external environment is to link the output of the model with numerical and theoretical studies, which can be used to 'convert' the zero-dimensional information given by the LEM in time-averaged velocity profiles. Examples of analytical correlations for the external flow field are the papers by Smith and Swift [90] and Krhishnan and Mohseni [91], respectively for circular and rectangular jets. These works aim also to

compare the characteristics of the synthetic jet flow field with the one of an equivalent continuous jet, by examining, among other things, the scaling laws of the centerline streamwise velocity, the jet spreading and the air entrainment as functions of the streamwise coordinate.

The LEM output can provide important insights on the creation of simple boundary conditions to be used in the numerical simulations of synthetic jets. As a matter of fact, the lower end of the actuator should be modelled as a thin diaphragm, whose motion could be strongly dependent both on the piezo-element vibration and the pressure forces of the air within the cavity. Therefore, to properly simulate the actuator it should be necessary to evaluate, for each time step, the diaphragm vibration using a fluid-structure interaction model. This approach, however, often leads to unacceptable computational costs. Lumped element models can be used, therefore, to simplify the computational setup, and, more importantly, to estimate the approximation induced by this choice. In particular, in several applications the diaphragm motion can be approximated by an oscillatory Dirichlet condition for the wall-normal velocity at the undeformed position of the wall ($x = x_c$)

$$U(x = x_c, y, z, t) = U_w(y, z) \sin(2\pi ft) , \quad (3.19)$$

where a plug approximation ($U_w = \text{const}$) or more complicated velocity distributions can be used. For asymmetric and multiple-orifice devices, indeed, it could be necessary to obtain (experimentally, theoretically or by a FEM computation) the diaphragm vibration and differentiating it in time. It should be noted that the enforcing of an autonomous oscillatory diaphragm motion basically corresponds to decoupling the structural and the Helmholtz oscillator, which is possible if the coupling factor is vanishing. In more general cases, the diaphragm dynamics and the air dynamics in the orifice neck are mutually influenced.

Moreover, it is worthwhile noting that Eq. 3.19 implicitly requires that the maximum diaphragm displacement is much lower than the cavity height. The latter assumption can be made if the maximum diaphragm displacement is much lower than the cavity height, otherwise a moving mesh technique should be used. Finally, in many applications the flow can be treated as incompressible, especially if the diaphragm is driven at its structural resonance frequency. In many cases, indeed, this frequency is much smaller than the Helmholtz resonance frequency. This fact holds, for instance, for the benchmark case analyzed in Chapter 2, and for the

multi-slotted actuator in Chapter 4. As explained in the previous Section, compressibility effects are negligible if the cavity is *acoustically thin*, which means that the acoustic Strouhal number $St_{ac} = 2\pi fw_c/c \ll 1$.

Chapter 4

Unconventional SJ actuators in quiescent environment

As explained in Chapter 3, several lumped element models and analytical expressions for the external flow field have been developed for the study of synthetic jets in quiescent condition. Nonetheless, these studies are typically based on simple configurations, such as single-cavity and single-orifice/slot devices, whereas in many applications the actuator must be inserted in narrow places. Moreover, the application of a single-orifice actuator to control flows around aircraft wings and tail is not appropriate, since the orifice exit area is much smaller than the wing area, leading to unsuccessful control. For this reason, in many flow control applications asymmetric or multiple jet configurations are often employed, especially to deal with separation control on wings [53] and aircraft tails. Moreover, the application of multiple-orifice actuators has revealed its maximum potential in impinging configurations. Indeed, Chaudhari *et al.* [92] first and Mangate *et al.* [93] later explored the thermal performances of an impinging SJ device. Their experimental measurements revealed that a multiple-orifice device exhibits a better heat dissipation with respect to a single centred orifice.

It is necessary, therefore, to analyze these unconventional devices in order to create new LEMs (which are able to account variations in the actuator geometry) and analyze the external flow field to detect jet interactions and possible modifications in the shape, the trajectory and the strength of the vortical structures generated by the actuator. First of all, different cavity geometries required a specialized study: as a matter of

fact, a very recent research line concerns the effect of the actuator and orifice geometry on the synthetic jet characteristics [94, 95]. The present research, instead, has been devoted to investigate the interaction of multiple synthetic jets for flow control applications. This subject has been segmented in two branches: on the one hand, a numerical study of a double-orifice device have been carried out, in order to study the resulting flow field. The advantage of using numerical simulation in place of experimental measurements is that they provide an unintrusive evaluation of the thermo-fluid-dynamics quantities within the cavity and an accurate tridimensional description of the vortical structures in the external flow field via Q-criterion (Hunt, Wray and Moin [96]) or λ_2 isosurfaces. The other branch is related to the design, characterization and testing of an unconventional slotted actuator. This device consists of 3 cavities, which are connected to the external environment by means of 12 slots. The analysis of the actuator in quiescent conditions could allow to state whether the device is capable of controlling the separated flow behind a backward-facing ramp.

4.1 Continuous twin jets: literature review

Parallel jets issuing from rows or arrays of adjacent nozzles are commonly encountered in several applications, such as in air conditioning systems, fire extinguishers, gas turbines, nuclear reactors, boundary layer control devices and vertical take-off/landing systems. Therefore, a significant effort has been devoted to understand their interaction mechanisms, both for two-dimensional (slotted) and three-dimensional (circular) configuration. Nonetheless, the interaction between multiple turbulent jets leads to very complicated flow systems, then the research focused on simpler cases, able to reproduce the interaction between multiple jets.

The minimal configuration able to mimic the interaction between multiple jets is the so-called twinjet, which is composed of two parallel (plane or round) jets, issuing from two identical nozzles in a quiescent environment. Apart from being a simple model of the mutual interaction between several jets, this system has also been employed in several engineering applications, such as in exhaust systems and cooling devices. The structure of the resulting flow field is well recognized in literature; Fig. 4.1 depicts the time-averaged streamwise velocity field, along with some relevant velocity profiles, obtained via a RANS computation per-

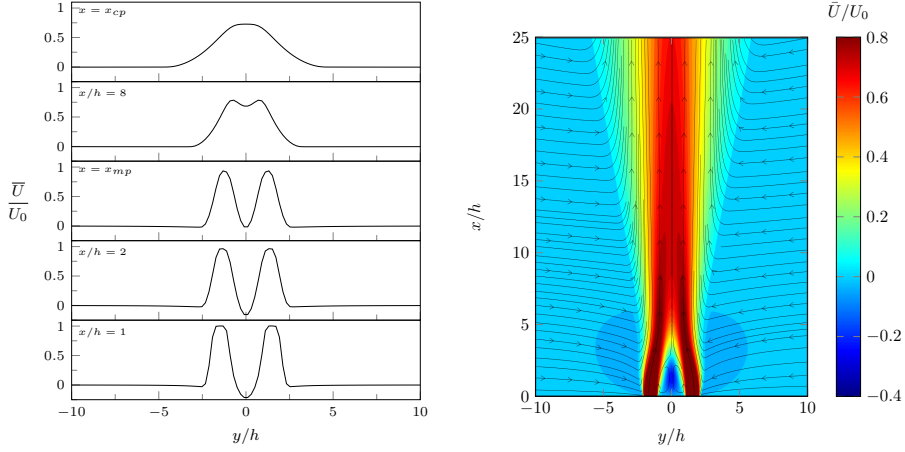


Figure 4.1: Time-averaged streamwise velocity component of a plane continuous twinjet. RANS simulations, $k - \varepsilon$ model (OpenFOAM). Reference case: Lee & Hassan (2018) [97]. $Re = U_0 h / \nu = 4900$, $s_o / h = 2.07$.

formed in OpenFOAM. The chosen reference case is reported in Lee and Hassan [97] (2018), and their PIV database was employed as a Validation & Verification benchmark by ASME. The relevant Reynolds number $Re = U_0 h / \nu = 4900$, where U_0 is the mean streamwise velocity at the slot exit and h the slot width, and the non-dimensional jet spacing is $s_o / h = 2.07$ (defined as the inter-axis distance).

Tanaka *et al.* [98, 99] and Okamoto *et al.* [100] identified three main regions, moving downstream from the exit plane, respectively for plane and round twinjets: converging, merging and combined regions. In the converging region the jets converge towards each other, whereas a recirculation zone appears between them (i.e. the mean flow is directed towards the exit plane). This recirculation zone is characterized by a sub-ambient pressure, as investigated by Miller and Comings [101], which makes the jet streamlines to curve and converge. This behaviour has been mainly observed for slotted configurations, whereas no recirculation regions has been detected for circular twinjets (where only a low-speed region has been detected in the converging region).

The merging region starts at the end of the converging one. In this zone the velocity peaks of the jets, initially lying on the nozzle axes, converge towards the symmetry plane, eventually reaching it and coalescing at the combined point. From this point the twinjet behave similarly to

a single free jet, with similar scaling laws of the axial velocity decay and the jet width increase. Lin and Sheu [102] found that the time-averaged velocity profiles are self-similar in both the merging and the combined region, whereas the velocity fluctuations become self-similar only far away from the exit plane, in the combined region. It is worth to note that, especially for high nozzle spacings, initially the jets are not influenced by the presence of the other jet, developing a potential core of small streamwise extension.

Special attention, therefore, have been initially paid on the main points of interest of the flow field, the merging point and the combined point. The former delimitates the converging region, whereas the second is located between the merging and the combined ones. Several scaling laws for the merging and combined points have been proposed, typically depending on the jet Reynolds number and the spacing-to-diameter ratio s_o/d of the jets, as show by Laban *et al.* [103] for circular jets and by Lee and Hassan [97] and Oskouie *et al.* [104] for slotted ones. Moreover, their position is obviously dependent on the nozzle geometry. Finally, also the jet injection strategy could have an impact on the flow features. In some experimental works the twinjet is obtained by splitting a single converging nozzle by means of a rectangular or conical pin. Other research groups inject the flow in the measurement regions by means of two non-interacting pipes. In other words, it can be stated that there is a strong influence of the inlet turbulence intensity on the near field characteristics of the flow field has also been found. This feature is critical for RANS simulations and DNS/LES computational not including the inlet pipes, which are strongly dependent from the inlet value of the turbulent kinetic energy, as demonstrated in Anderson and Spall [105].

More recently, several experimental works (basically based on PIV) have been devoted to analyze the vortex development in the near-field, especially for jets in close proximity. Zang *et al.* [106] found for circular jets that, independently from the separation distance, two different peaks in the velocity spectra can be seen. They associate this frequencies with the vortex formations on the inner and the outer shear layers of the jets. However, only for $s_o/d < 2$ the vortices arising from the inner shear layers instability merge, forming a staggered configuration similar to the Von Karman vortices behind a bluff body. This conclusion have been corroborated by a decomposition of the flow field by means of a Proper Orthogonal Decomposition. A similar study have been carried out by Lee and Hassan

[97] for plane jets, revisiting the problem of the merging point scaling with s_o/d and investigating more in detail the turbulent characteristics of the twinjet. Similar analyses on the turbulent statistics have been also made for circular jets by Laban *et al.*[103] and Aleyasin *et al.* [107].

4.2 Double-orifice synthetic jet actuators

Several works concerned the interaction between twin continuous jets issuing in a quiescent medium. However, as stated in Chapter 1, in many active flow control techniques pulsed jets are preferred to continuous jets, in order to reduce the mass flow rate required by the control systems and introduce a characteristic frequency in the flow field to be controlled.

The first study concerning dual-orifice SJ actuators was carried out by Watson *et al.* [108], which investigated experimentally the effect of the jet exit area and jet spacings. Implications of the use of adjacent synthetic jets to control an incoming crossflow were discussed subsequently by the same group [109]. More recently, Riazi and Ahmed performed numerical simulations of the flow field generated by a double-orifice SJ [110]. The behaviour of the flow field generated by this device has been first compared with an equivalent, single-orifice one; then the effect of varying the orifice diameter and the jet spacing have been investigated. They stated that the jet spacing strongly affects the generation of the vortex systems, and two distinct and non-interacting vortex trains can be seen when the ratio between the jet spacing and the orifice diameter is high enough. Moreover, they found that the threshold value of s_o/d for this behaviour depends on the dimensionless stroke length of the actuator. However, their analysis is restricted to very low Reynolds numbers (indeed, the flow is laminar), which are hardly obtained in practical SJ applications. Moreover, the flow is treated as symmetric with respect to the two (geometrical) symmetry planes of the actuator. This assumption obviously precludes any chance to observe any wave-like interaction between the jets, previously observed by Zang *et al.* [106] for continuous twinjets.

As for continuous twinjets, several techniques can be chosen to produce synthetic twin jets. In all the aforementioned studies the orifices are on top of a single resonant cavity. In this case the deformation of a piezoelectric element, glued on the bottom part of the cavity, produces periodic variations of volume and pressure within the cavity, which leads to the formation of two, in-phase, synthetic jets. This configuration has

been also selected by Chiatto *et al.* [111], which studied a double-orifice SJ device with a joint numerical, experimental and analytical LEM investigation for high values of s_o/d . However, in some cases it could be useful to introduce a phase difference between jets, as in the research work of Smith and Glezer [112]. Luo *et al.* [113] designed an innovative synthetic jet device, where a resonant cavity is splitted by a wall on which two piezoelectric elements are glued. The walls oscillation creates two ZNMF jets in opposing phase. Finally, the same goal can be accomplished by means of jets issuing from twin, independent cavities, as in Alimohammadi *et al.* [114]; this leads to a continuous range of the phase difference between the jets, which can change between 0 and 2π .

As a summary, the characteristics of the zero-net-mass-flux twinjets are strongly affected by many dimensionless characteristics: Reynolds, Strouhal and Stokes numbers (as for single-orifice actuators), s_o/d (as for continuous twinjets) and jet phase difference. The present numerical study concerns the evolution of the vortex structures and their merging in case of a double-orifice, single-cavity synthetic jet actuator. A series of direct numerical simulations involved one of the double-orifice devices examined in Chapter 3, which is properly designed to control separated flows. Indeed, its design frequency (which equals the coupled structural resonance one) is $f = 1850$ Hz, its diameter is $d = 2$ mm, and the jet reference velocity is $U_0 \approx 6$ m/s. Only the jet spacing effect has been investigated: starting from the experimental setup, this parameter has been gradually reduced, in order to recognize the jet interaction for low values of s_o/d .

4.2.1 Numerical setup

The first numerical campaign consisted in a series of three-dimensional direct numerical simulations, carried out using OpenFOAM. The code was deemed adequate for the present simulations (which aims only to investigate time-averaged and phase-averaged flow fields), indeed it has been already used for RANS/LES simulations of twin, continuous jets by Li *et al.* [115, 116]. The numerical setup is described in Fig. 4.12, whereas the main non-dimensional geometrical parameters are listed in Table 5.1. It is worth noting that the full three-dimensional geometry of the actuator is included into the numerical domain, since the cavity geometry strongly affects the external development of the flow. The computational domain, therefore, was made of a cylindrical cavity, two orifices and the external

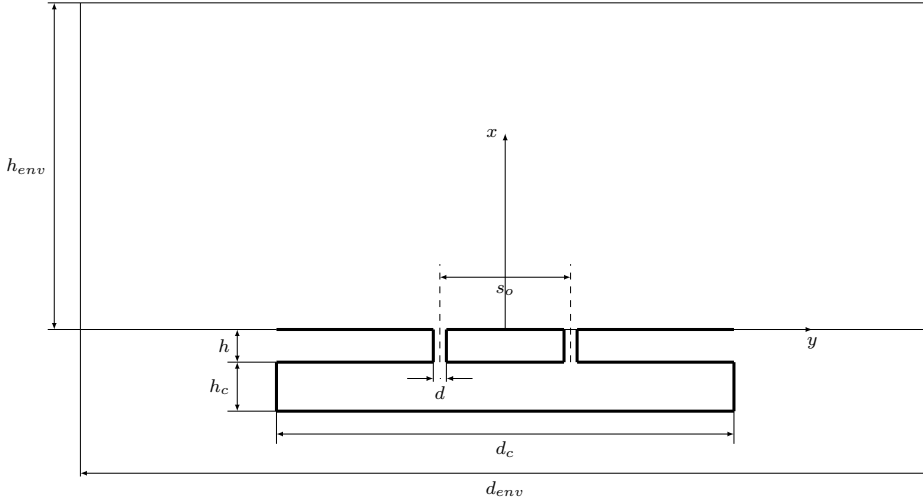


Figure 4.2: Description of the nomenclature and symmetry-plane slice of the three-dimensional numerical domain. Actuator walls are depicted in bold.

domain (of cylindrical shape).

Table 4.1: Main non-dimensional parameters for the numerical simulations.

Parameter	Value
Cavity diameter, d_c/d	21
Cavity height, h_c/d	1.5
Orifice height, h/d	1
Orifice distance, s_o/d	2.5,3,3.75,5,7.5,12.5
External domain diameter, d_{env}/d	71
External domain width, h_{env}/d	25
Dimensionless stroke length, L_0/d	1.7
Reynolds number, Re_0	806
Strouhal number, St_0	3.67
Stokes number, S	54

The flow is treated as incompressible and, as explained in Chapter 3, the diaphragm motion is mimicked by an oscillatory inlet condition on the cavity bottom. However, in order to describe the actual shape of the diaphragm vibration, the spatial variation of the inlet velocity at the cavity bottom is chosen as the time derivative of the theoretical deforma-

tion at the resonance frequency, which can be fairly approximated by the leading vibrational mode of a simply supported circular plate $F_w(y, z)$. This assumption has been confirmed by experimental measurements of the diaphragm deformation obtained by means of a laser Doppler vibrometer (not shown herein). The amplitude of the diaphragm motion is obtained enforcing the global cycle-averaged mass conservation between the diaphragm and the orifice exits, whose validity is guaranteed by the "lumped" flow conditions within the cavity (as explained in Chapter 3).

$$U(x = 0, y, z, t) = \dot{x}_w(y, z, t) = F_w(y, z) \sin(2\pi ft) \quad (4.1)$$

No-slip boundary conditions are applied on all the fixed walls of the actuator, whereas Neumann boundary conditions for the velocity are enforced on the side boundaries and on top of the external domain (where the differential pressure is set to 0). A domain-independence study has been made to define the dimensions of the external environment. Simulations has been carried out for six values of the orifice spacing s_o ; the minimum jet spacing is shown according to Riazi and Ahmed work, which pointed out that only for $s_o/L_0 < 1.5$ a strong interaction between the jets can be observed. However, it is worth remembering that they considered a different definition of jet interaction, basically incentrated on the vortex merging and coalescence. The present analysis, instead, is based on the definition of time-averaged merging and combined points to quantify the interaction between the jets. The flow field is initially in quiescent conditions; time-averaged flow fields have been obtained by averaging the instantaneous flow fields over 40 cycles, starting from the eleventh one to remove transient effects. In fact, while the merging point positions are well estimated even if twenty averaging cycles were used, the far field was still far away from convergence.

The validation consisted in the comparison of the phase-averaged hot-wire data at the orifice exit and its numerical counterpart. The hot-wire measurements have been inverted during the suction phase to reflect the actual behaviour of the flow, following Smith and Glezer's work [30]; this procedure allows to have a fair comparison with the numerical data. This comparison is shown in Fig. 4.3 for the three meshes used for the grid-independence analysis. It can be observed that the velocity time-series recovers an almost-sinusoidal shape only at the finest grid resolution. Unfortunately, the present case can be only used for validation; indeed, time-averaged streamwise velocity distributions in the $x - y$ plane showed

that the interaction between the jets is almost negligible for this value of s_o . Therefore, after validating the computational mesh for $s_o/d = 12.5$, the orifice spacing have been progressively reduced.

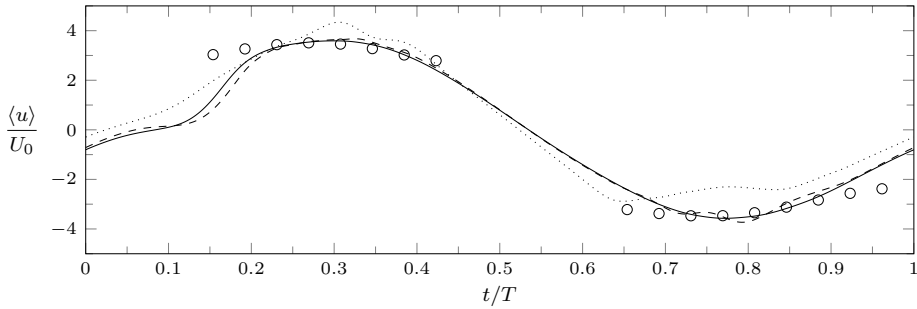


Figure 4.3: Comparison between numerical and experimental (circles) stream-wise phase-averaged velocity data at the orifice exit plane: coarse grid (dotted), medium grid (dashed), fine grid (solid line).

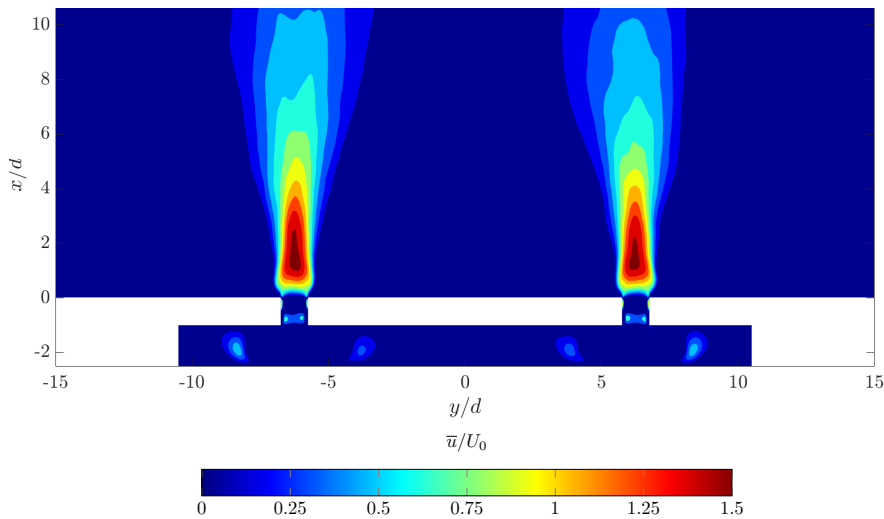


Figure 4.4: Distribution of the time-averaged stream-wise velocity field in the $x - y$ plane, $s_o/d = 12.5$.

4.2.2 Effect of orifice spacing

Fig. 4.5 shows a contour plot of the streamwise time-averaged velocity \bar{u} for two smaller orifice spacings, $s_o/d = 2.5$ and $s_o/d = 5$.

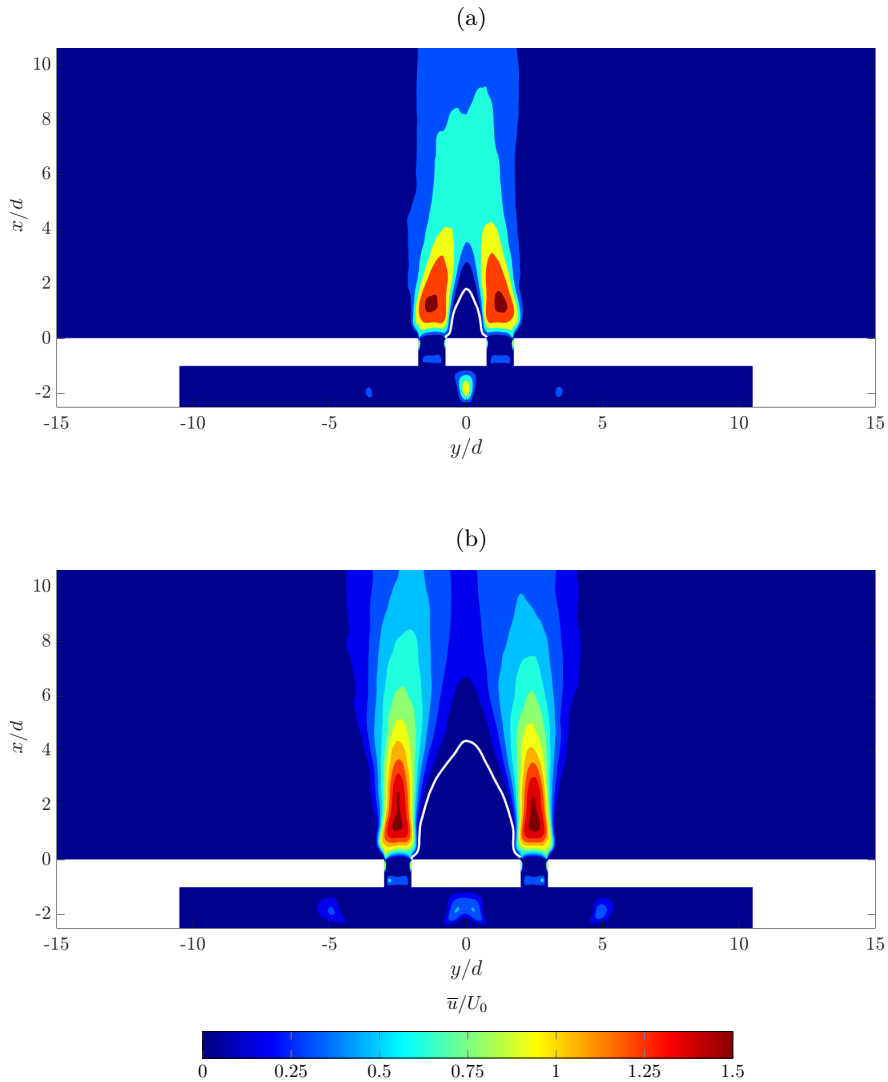


Figure 4.5: Time-averaged flow field, streamwise component \bar{u} , $z = 0$. (a) $s_o/d = 2.5$, (b) $s_o/d = 5$. A white contour line $\bar{u} = 0$ is depicted to highlight the recirculation zones.

The very same flow structure described in Sec. 4.1 can be recovered for double-orifice SJ actuators. As a matter of fact, the flow field can be still divided in a converging, merging and combined regions. The first region is characterized by the converging and merging of the jets. Indeed, the entrainment of the flow by the jets creates a recirculation zone between them, which is characterized by a low (time-averaged) pressure. At the end of this region a reattachment point appears on the actuator axis, whose distance from the exit plane is proportional to the orifice spacing, as shown in Fig. 4.6. The strength of the recirculation region, represented by the maximum counterflow velocity, decreases monotonically with s_o/d . It can be stated that the flow field behaviour is closer to plane twinjets rather than round jets, possibly due to the higher mixing and entrainment generated by synthetic jets with respect to continuous ones [90]. Moreover, it seems that, contrarily to the result of Riazi and Ahmed, jet interaction can be still detected for $s_o/L_0 > 1.5$. It must be noted, however, that their study has been carried out at a smaller Reynolds number, which leads to a fast dissipation of the vortex ring before they can meet each other.

Similarly to the merging point, also the combined point fades away from the actuator exit plane as the orifice spacing is increased. The velocity in this point, which is the maximum centerline velocity along the actuator axis, decreases for higher orifice spacings. Crosswise distributions of time-averaged velocity profiles at several streamwise stations are represented in Fig. 4.7, showing the transition from the twin-jet behaviour (in the vicinity of the jet exit) to the typical far-field characteristics of a single jet.

Further insights about the vortex trajectories and the jet formation can be obtained using phase-averaged quantities. Fig. 4.8 depicts the evolution of the synthetic jet, in terms of phase-averaged phase-averaged streamwise velocity contour plots, for $s_o/d = 2.5$ and $s_o/d = 5$, whereas in Fig. 4.9 a visualization of the vortical structures at the end of the ejection has been obtained by means of Q-criterion. In Fig. 4.8 only the right orifice is reported, since phase-averaged fields are symmetric about the actuator axis. The interaction between the twinjets is very strong for $s_o/d = 2.5$: the entire jet is inclined towards the actuators axis during the entire actuation cycle, and the velocity profiles in the crosswise direction are strongly asymmetric with respect to the orifice centerline. In particular, the entrainment generated by the vortex ring is stronger in the inner side of the field, creating the recirculation zone detected also in the

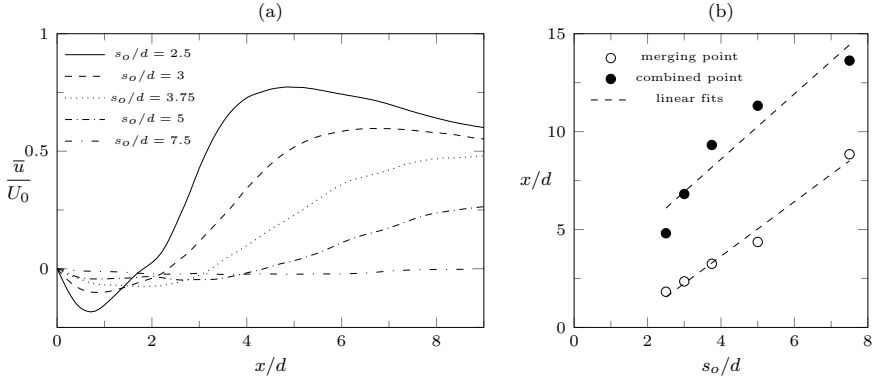


Figure 4.6: (a) Distribution along the x axis of the streamwise component of the time-averaged flow field \bar{u} ; (b) Streamwise location of merging and combined points as a function of the orifice spacing.

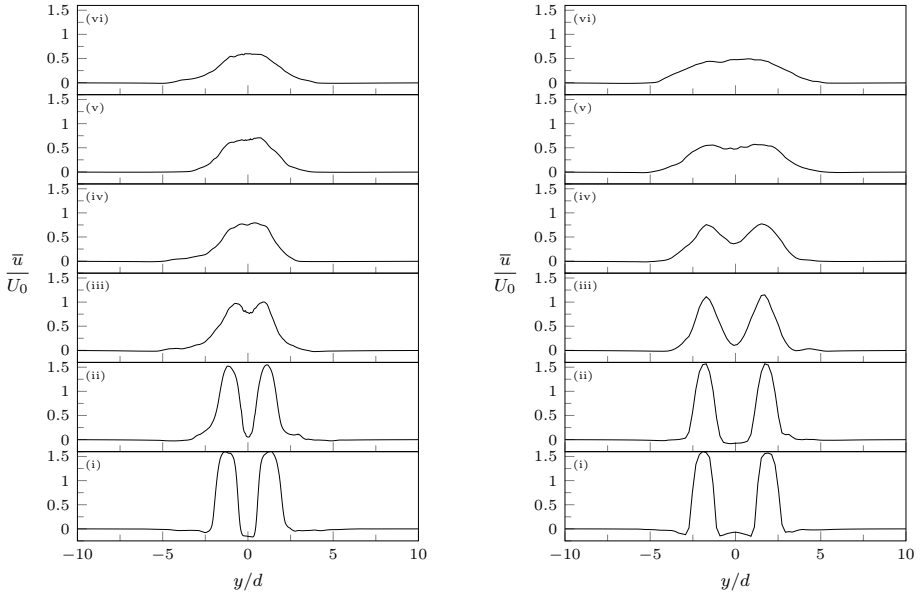


Figure 4.7: Crosswise distributions of time-averaged streamwise velocity at streamwise stations (i) $x/d = 1$, (ii) 2, (iii) 4, (iv) 6, (v) 8, (vi) 10, for $s_o/d = 2.5$ (left) and $s_o/d = 3.75$ (right).

time-averaged velocity profiles. This effect is milder for the $s_o/d = 5$ case, where basically the near-field is symmetric about the orifice centerline and

the vortex trajectories are aligned with the streamwise direction.

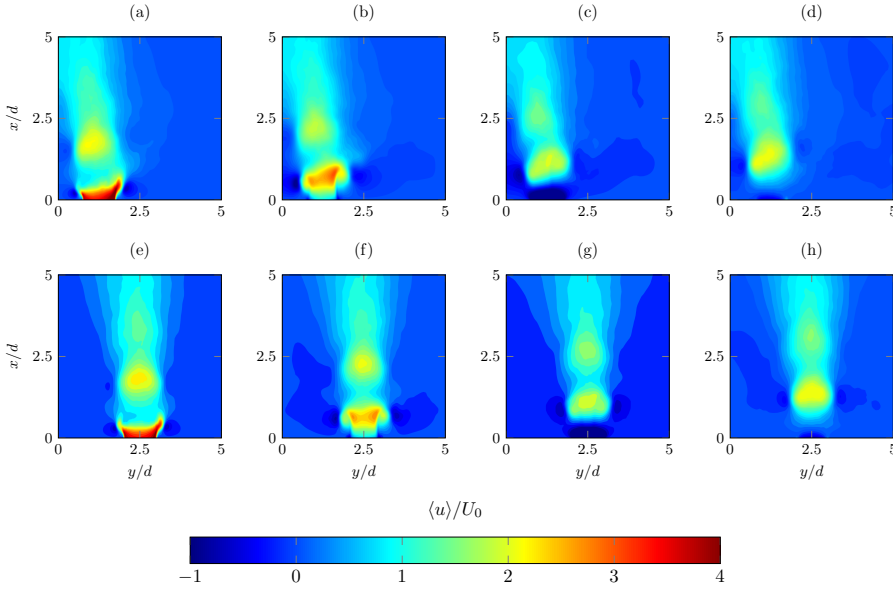


Figure 4.8: Phase-averaged flow fields, streamwise component $\langle u \rangle$, $z = 0$, $s_o/d = 2.5$ (panels (a)-(d)), $s_o/d = 5$ (panels (e)-(h)), $t/T = 0.25$ (first column), $t/T = 0.5$ (second column), $t/T = 0.75$ (third column), $t/T = 1$ (last column). Only the right orifice is reported, due to the symmetry of the streamwise velocity field.

The vortex behaviour in the latter case is very similar to the single-orifice one: at the beginning of the ejection phase a vortex ring is created from the orifice edges, therefore the induced velocity is maximum in that zone. At the end of this phase the vortex breaks up in smaller structures and slows down. At the beginning of the suction phase a stagnation point appears along the jet centerline (saddle point); the maximum distance of the saddle point from the exit plane is less than d . It is worth noting that using a very large number of averaging cycles for the phase-averaging leads to preserve the vortical structures of the previous cycles, showing that the interaction of the initially parallel vortices starts only after more than 3 actuation cycles for the vortices generated in the $s_o/d = 5$ case. At this point, indeed, the jets spread and eventually interact with each other. As a summary, for low spacings the interaction between the twin jets occurs in the near field, and it is generated by the inclination of the vortex trajectories towards the x axis, whereas for high spacing the jet interaction

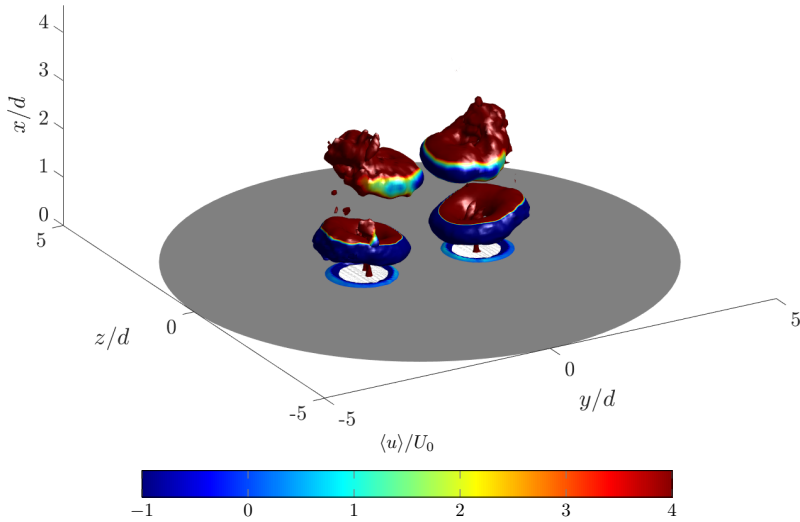


Figure 4.9: Isosurfaces of phase-averaged Q-criterion, coloured with the streamwise phase-averaged velocity component $\langle u \rangle$: $s_o/d = 2.5$, $t/T = 0.5$, $Q = 0.05$.

is restricted to the far field and it is basically due to the jet widths increase. The threshold between these two behaviors can be a key design parameter if no strong jet interaction and/or spanwise modulation of the control are required (as, for instance, for separation control applications).

4.3 Design and characterization of a multi-slotted SJ actuator

In this section the design, the experimental and numerical characterization of a multi-slotted SJ actuator for the control of separated flow is explained. The experimental part of the present activity has been funded by CIRA (Italian Center for Aerospace Research) under the SHAFT project. The use of slotted configurations is widespread in the suppression of separation bubbles; the specialized literature reports several contributions about slotted SJs in crossflow, where both single long slots running all over the spanwise direction of the flow to be controlled, as in Van Buren's *et al.* work [117], and discrete evenly spaced orifices, as in [53, 118, 119] are employed. For instance, in Sahni *et al.* [53] an array of actuators, formed by three rows of 5 actuators, were mounted along the span of a wing. Obvi-

ously, in this case there are as many slots as diaphragms, since each slot is located on top of a cavity. Similarly, Jabbal *et al.* [118] designed an array of 30 synthetic jet actuators and placed them within the flap of a wing model. Finally, in McGlynn *et al.*'s work [119], a segmented synthetic jet actuator was used to control the flow over a NACA 4421 airfoil at zero incidence. The slot of the synthetic jet has been segmented in two equal pieces (along the wingspan) to study the vortical structures generated by the edges of the slits (using LES). The flow fields obtained varying the gap between the slots were then compared with the one obtained with a single slot in the same flow conditions (and same total exit area).

The research activities has been developed in two steps. Firstly, the design of the actuator and preliminary testing have been carried out. During this preliminary activity it has been demonstrated that the designed actuator complies with the values of momentum coefficient and reduced frequency to be achieved for the final application. Experimental measurements, obtained by means of hot-wire Anemometry, allowed to obtain the velocity field at the slot exit in order to validate the actuator design. Numerical simulations permitted to state that the edge effects on the external slots are negligible, thus obtaining a homogeneous control power along the spanwise direction. In a second step a more accurate description of the device has been obtained, combining also lumped element modeling and laser Doppler vibrometer data. The shape and the amplitude of the diaphragm deformation has been first obtained. The expected external flow field is obviously more complex than for a single-slotted actuator, due to the possible interaction between the jets. The latter field is quite complicated as well, indeed previous studies by Van Buren *et al.* [117] via PIV and by Wang *et al.* [120] via flow visualization techniques showed that each vortex train is subjected to the axis switching phenomenon, namely seems to vary its orientation when moving downstream (axis switching). These facts yield a very complex topology of the vortex system in the external environment.

4.3.1 The SJ Device

The device was made in-house, with the only exception of the piezoelectric actuators (Sonitron SPS-8770-03). Fig. 4.10 shows the bottom (left) and the top (right) views of the actuator, whereas Fig. 4.11 summarizes the reference frame and the nomenclature used to describe the actuator geometry (whose characteristics are in Table 4.2). The device is based on a

stainless steel sandwich structure: the top part, with dimensions of $261 \times 70 \text{ mm}^2$, contains twelve slots. A flat rectangular ring is used to create a single cavity, under which three piezo-speakers are applied; the bottom part has been designed only to provide a structural support to the piezo-elements. The slot spanwise dimension is $l = 15 \text{ mm}$ and $h = 1 \text{ mm}$, the distance between two consecutive slots of the same group is $l_c = 5 \text{ mm}$, whereas two adjacent slot rows are distant from each other by $l_s = 11.85 \text{ mm}$. This means that jet interaction in the far field must be expected, especially for slot belonging to the same row. The overall height of the actuator is 5 mm : the cavity depth is $w_c = 2 \text{ mm}$, the interconnecting zone between the three actuator parts is $w_i = 1 \text{ mm}$, whereas the piezo-speaker support is 2 mm thick.



Figure 4.10: Actuator bottom (left) and top (right) part views. Courtesy of CIRA.

Table 4.2: Main geometrical characteristics of the analyzed actuator.

Parameter	Value
Slot width and spanwise length, h and l (mm)	1x15
Slot depth, w (mm)	1
Slot distance in the same group, l_c (mm)	5
Slot distance of adjacent rows, l_s (mm)	11.85
Cavity depth, w_c (mm)	2
Diaphragm dimensions, h_d and l_d (mm)	70 x 87

The choice of such a configuration is driven by the fact that the exit velocity is uniform across the slot and it is high enough for flow control applications; moreover, the realization and the maintenance of this actuator is simpler than a synthetic jet array. The actuator has been designed to have a structural natural frequency of $f = 250 \text{ Hz}$ in order to match the target values of C_μ and F^+ determined for the crossflow application. The device, therefore, is preliminarily characterized at this frequency in

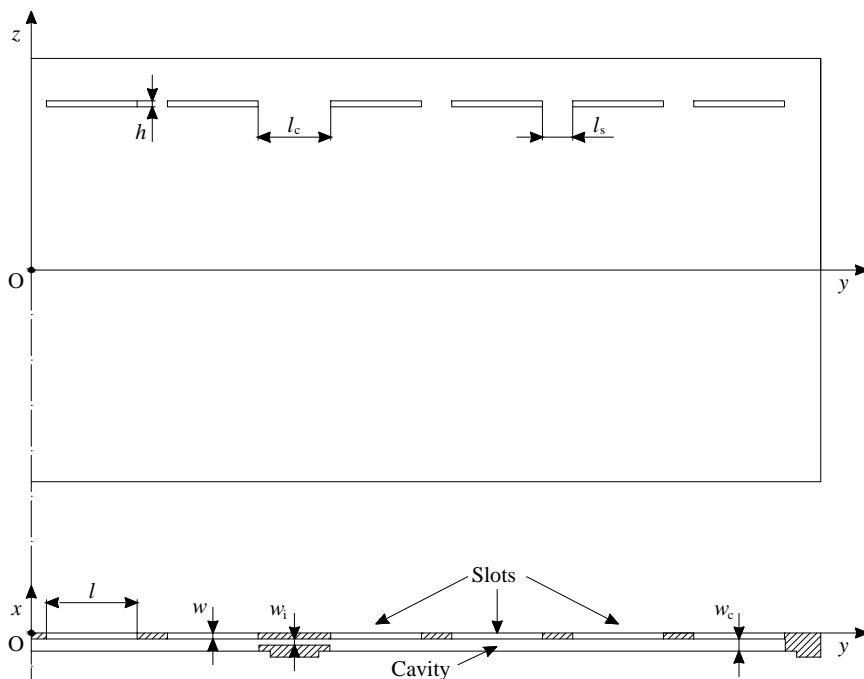


Figure 4.11: Definition of the geometrical characteristics of the multi-slotted actuator and description of the reference axes.

Sec. 4.3.2 using hot-wire anemometry and DNS. In a second step, instead, its frequency response has been evaluated in a wider range of actuation frequencies, and a lumped element model has been calibrated on the experimental data.

4.3.2 Preliminary characterization

A preliminary investigation was made using the hot-wire anemometry technique: a complete characterization of the second slot has been carried out, placing the probe parallel with the slot width, and moving it along x and y directions, to obtain the distribution of the streamwise velocity. Phase-averaged quantities has been collected with a sampling rate of 10 kHz, for 2000 operating cycles. Forty phases have been therefore obtained. A hot-wire anemometer (Dantec Dynamics, MiniCTA), equipped with a $5 \mu\text{m}$ diameter, 1.25 mm long wire probe, is used for this pur-

pose. The experimental uncertainty on this quantity has been estimated following Yavuzkurt's work [121], finding to be less than 3% for all the measured values.

On the numerical side, all simulations have been carried out using the *pimpleFoam* solver of OpenFOAM. The computational setup is similar to the one employed in Chapter 2. The finite-volume discretization of the Navier-Stokes equations is based on second-order centered schemes for both the convective and the diffusive terms. The pressure linear system is solved by the GAMG method with a tolerance of 10^{-7} , and the time discretization is based on second-order schemes. The actuator geometry is completely included into the simulations, and the external environment is a parallelepiped of dimensions $60h \times 290h \times 140h$. The y and z dimensions of the domain are deliberately chosen to be larger than the actuator ones, in order to estimate the upstream entrainment of the jet. The mesh is obtained using the *blockMesh* utility, initially creating half mesh and then mirroring it about the symmetry plane $y = 0$ of the actuator. A grid independence analysis has been performed, to obtain a final numerical grid of about 35 million mesh for the finest case. The stroke length L_0/h has been used as an indicator of the mesh convergence, as explained in Chapter 2.

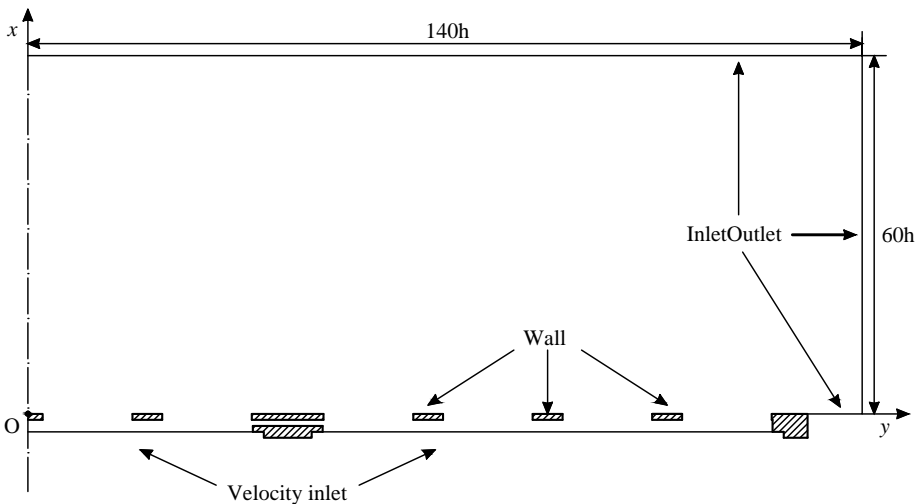


Figure 4.12: Domain and boundary conditions used in the numerical simulations. Only half of the computational domain is represented in the sketch.

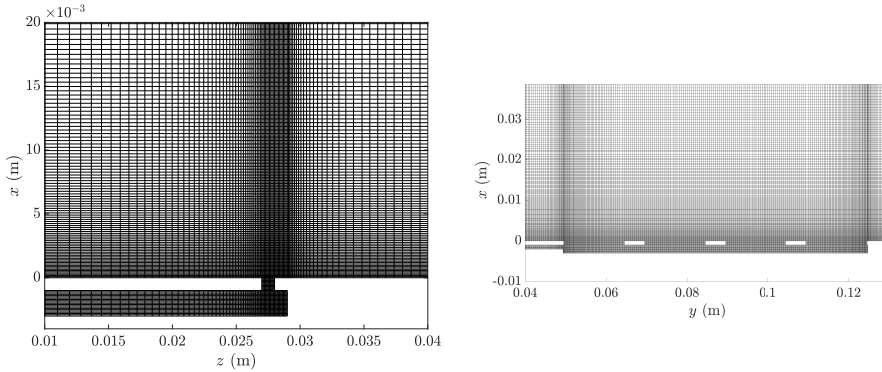


Figure 4.13: Front (left) and side (right) view of the mesh used in the numerical simulation, zoomed near the slot exit plane.

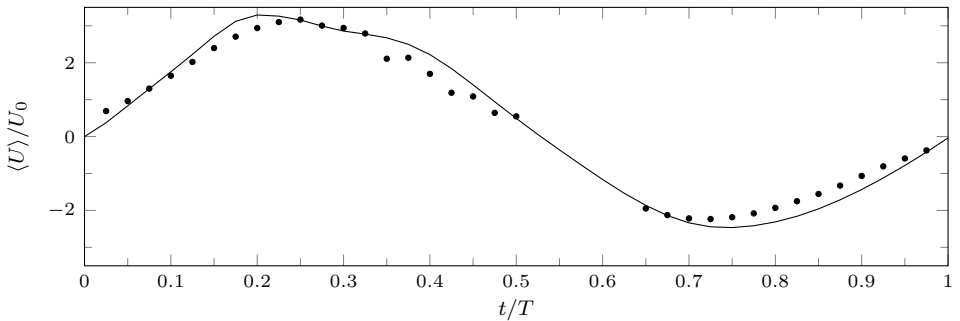
DNS computations have been based on the hot-wire measurements, with the same procedure explained in Chapter 3. In particular, the value of U_0 to be used in the simulations is equal to 2.85 m/s, which corresponds to a peak velocity of 9 m/s; the main dimensional and non-dimensional parameters are summarized in Table 4.3. An oscillating inlet condition has been applied on the lower surface of the actuator, estimating U_w as $\pi n(A_0/A_w)U_0$, (where A_w are the total area of the oscillating surfaces and $n = 12$ the number of slots). A no-slip condition is enforced on all the other actuator walls, while the InletOutlet boundary condition is used for all the environment faces. Zero-gradient boundary conditions are enforced for the pressure field on the walls, while pressure is set to zero on the outlet boundaries. The flow field is initially in quiescent conditions; thirty actuation cycles are simulated, time- and phase-averaged quantities have been accumulated over the last 20 cycles.

The computational work has been accomplished in two phases. Firstly, the numerical phase-averaged velocities near the second slot exit has been compared with their experimental counterpart, to validate the simulations. The time variations of the streamwise velocity at the slot exit $x = 0$ are shown in Figure 4.14. Both simulations and experiments detect an almost sinusoidal trend, with an ejection peak slightly higher than the suction one. The agreement between DNS and experimental data is fairly good for the chosen grid, confirming the validity of the computational setup.

Numerical and experimental results have been also compared in the spanwise direction of the flow, to ensure that all the main characteristics

Table 4.3: Main dimensional and non-dimensional parameters for the analyzed case.

Parameter	Experimental	Numerical
Actuation frequency, f (Hz)	250	250
Slot width, h (mm)	1	1
Slot spanwise length, l (mm)	15	15
Average jet velocity, U_0 (m/s)	2.85	2.95
Maximum exit velocity, U_p (m/s)	9.1	9.5
Reynolds number, Re_0	190	197
Strouhal number, St_0	0.0877	0.0842
Stokes number, S	10.23	10.23
Dimensionless stroke length, L_0/h	11.41	11.86

**Figure 4.14:** Time variation of the phase-averaged streamwise velocity component at the center of the 2nd slot exit; numerical (solid line), experimental (\bullet).

of the flow field are properly captured. Results are shown for for the ejection peak (Fig. 4.15 (a)), and for the suction peak (Fig. 4.15 (b)). Both data predict an irregular velocity profile at ejection peak, as the vortex system is still in the vicinity of the slot exit at that time, whereas the velocity profile at suction peak is smoother. It is worth noting that a fair agreement between the results is achieved at suction peak, which is a good indicator of the grid independence of the simulation (as shown in Chapter 2), whereas some discrepancies arise in the ejection peak.

The second step of the work consisted in using DNS data to get insights on the effectiveness of the novel actuator as a flow control system. Vortex visualization has been used to investigate the vortex formation and evolution. Figs. 4.16-4.17 show that the vortex system is formed by twelve rectangular vortices, which quickly undergo secondary instability

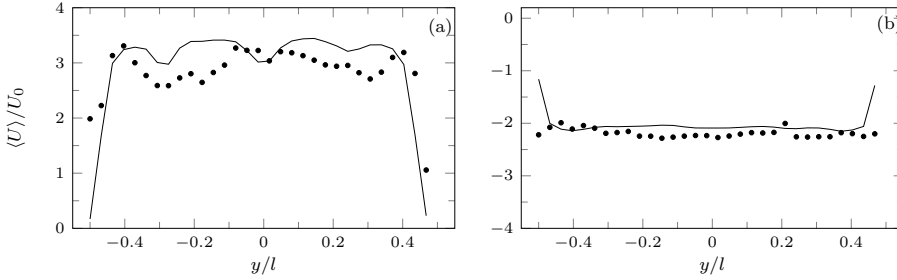


Figure 4.15: Phase-averaged streamwise velocity profiles along the spanwise y direction; slot 2, $x/h = 0.2$. (a) expulsion peak ($t/T = 0.25$); (b) suction peak ($t/T = 0.75$); numerical (solid line), experimental (\bullet).

and transition to turbulence. The vortex development in the far field is characterized by the axis switching, as shown in previous works concerning rectangular jets. The characteristic length of the axis switching is related to the slot spanwise width, which is much smaller than the actuator spanwise length; this results in a vortex system which covers the entire spanwise length, which is an interesting feature for control purposes. In addition, the extension along the z direction of the vortex system is bounded by the slot spanwise length, which means that the actuator provides a localized modification of the flow to be controlled.

Finally, an investigation of the saddle point position has been made for all the slots. Two main results have been obtained: firstly, edge effects are of minor importance for the extremal position of the saddle point. Secondly, the saddle point position is relatively close to the exit plane, which means that the near-field region extends only for a few slot widths h from the exit plane.

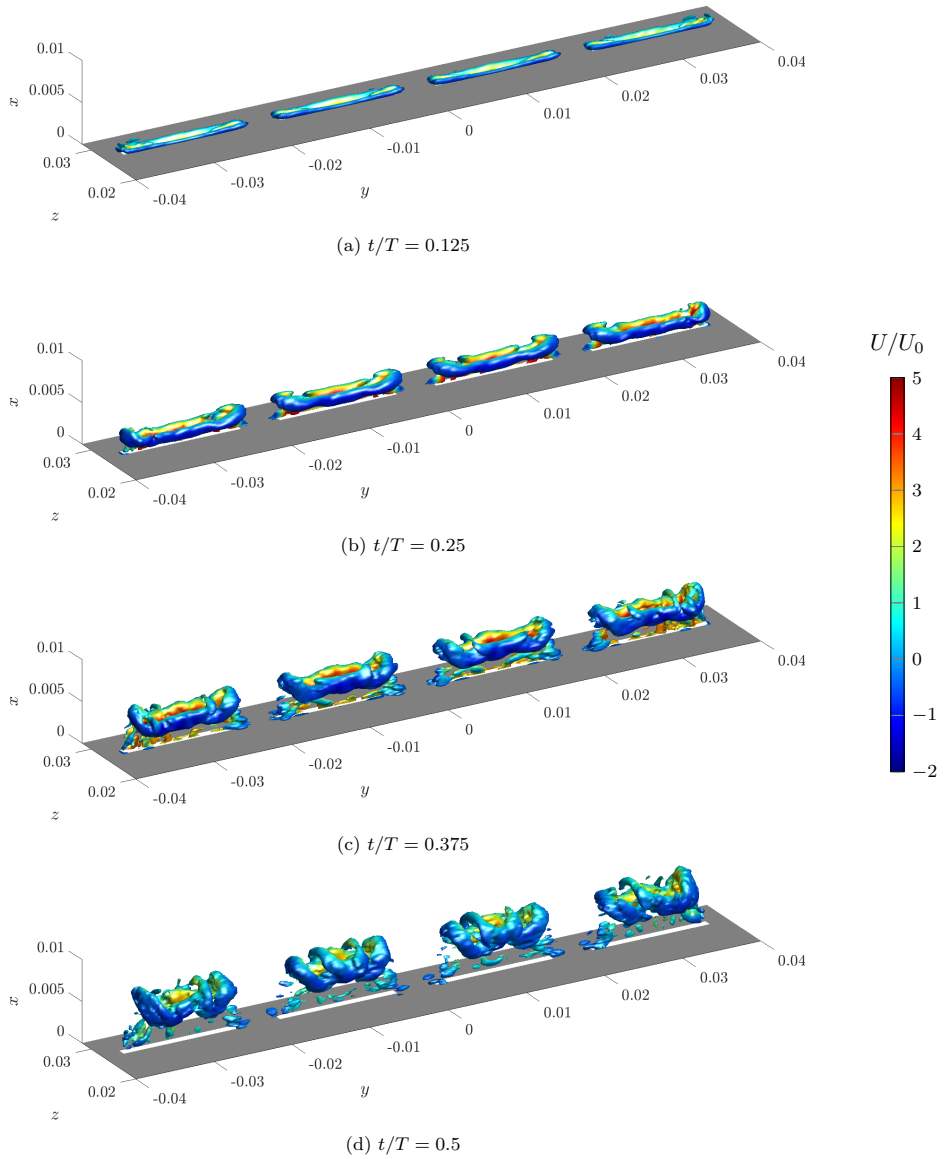


Figure 4.16: Evolution of the vortical structures in the near-field for the central slots, visualized by $Q = 0.02$ isosurfaces. Ejection phase. The isosurfaces are colored with the phase-averaged streamwise velocity component U/U_0 .

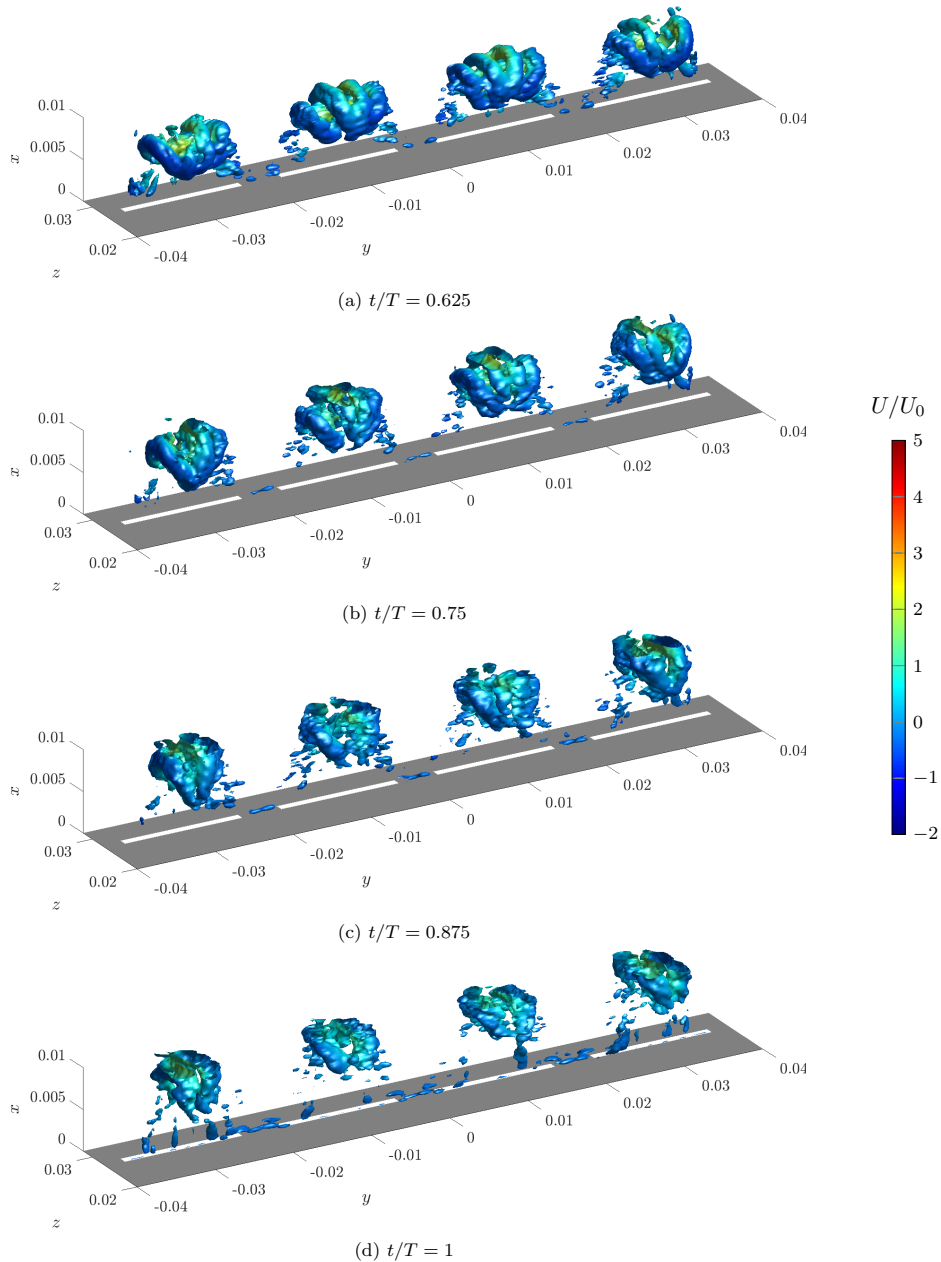


Figure 4.17: Evolution of the vortical structures in the near-field for the central slots, visualized by $Q = 0.02$ isosurfaces. Suction phase. The isosurfaces are colored with the phase-averaged streamwise velocity component U/U_0 .

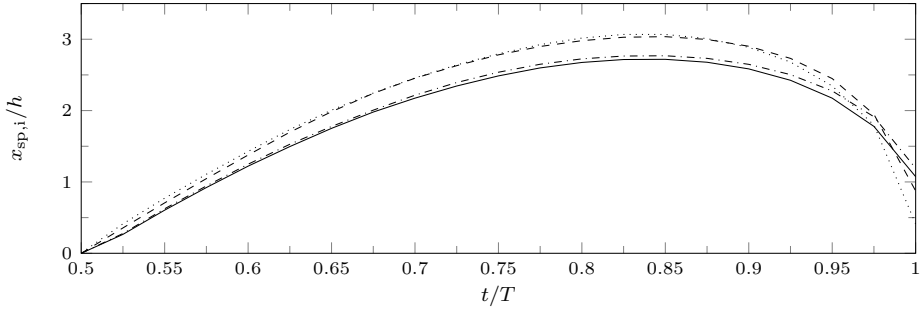


Figure 4.18: Saddle point position $x_{sp,i}$, during the suction phase, for different slots: continuous and dotted lines refer to outer slots; dashed and dashdotted lines to inner slots.

4.3.3 Frequency response and lumped element modeling

The frequency response analysis was obtained analyzing both the diaphragm dynamics (and its characteristic frequencies) and the streamwise jet velocity at the exit section of a central slot (the 6th one). The former analysis has been carried out to evaluate the diaphragm vibrational modes and its natural frequencies, as the mechanical properties of the diaphragm were not provided by the manufacturer. For this aim, a vibration test was performed with a scanning Laser Doppler Vibrometer (LDV): the piezo-element was excited with a sine signal (of $V_{pp} = 1$ V in amplitude), having its forcing frequency f in the 0 – 5000 Hz range.

Fig. 4.19 reports the frequency response, in terms of maximum diaphragm displacement, for a point located at the center of the piezo-element disk. Two peaks can be identified: a major peak is found around $f \approx 250$ Hz and corresponds to the first modified structural resonance frequency of the diaphragm; a second peak is uncovered at $f \approx 1000$ Hz, which represents a higher shim vibrational mode. The Helmholtz resonance frequency is not retrieved, meaning that it occurs at higher values.

Vibration tests provide also information on the entire diaphragm deformation (not shown herein). The deformation corresponding to the first resonance frequency resembles the classical mode (1,1) of a rectangular plate. Higher frequencies correspond to more complicated deformations; indeed, it has been verified that the second peak corresponds to a deformation resembling the mode (1,3). As a consequence, the dynamics of the diaphragm at the first frequency peak can be approximated by the

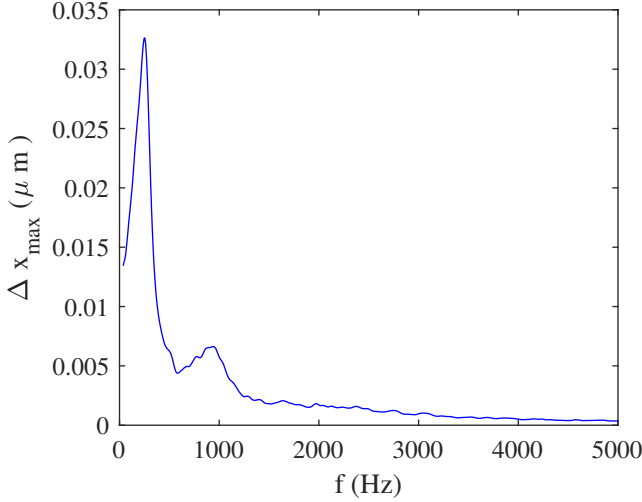


Figure 4.19: Maximum diaphragm displacement as a function of the actuation frequency.

analytical expression of the (1,1) mode deformation, which reads:

$$z_w(x, y) = Z \cos\left(\frac{\pi}{l_d} x\right) \cos\left(\frac{\pi}{h_d} y\right) \sin(2\pi ft) \quad (4.2)$$

with being Z the maximum deflection. Eq. (4.2) involves a maximum error of 1%. This equation can be used to define a boundary condition for an accurate simulation of the flow within the cavity.

On the other hand, the frequency response in terms of exit jet velocity was accomplished using hot-wire anemometry. The analysis was limited to a frequency ranging from 0 to 1500 Hz, since, as mentioned above, the Helmholtz frequency for this device is too high for flow control applications. The velocity experimental data will be reported in non-dimensional form, using the slot width as reference length. Fig. 4.20 shows the dimensionless stroke length evolution as a function of the Stokes number.

For low Stokes numbers (namely low frequencies), the device follows the incompressible solution, meaning that the fluid flow rate entering the cavity through the diaphragm motion equals the volume flow rate issuing from the slots exit. This is a linear function of the operating frequency, therefore in the $St - L$ plane it corresponds to a constant value. Then, the actuator response is amplified until it reaches a maximum at the major

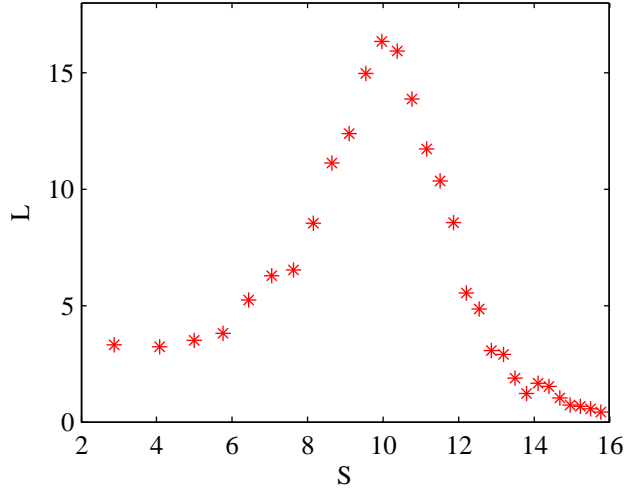


Figure 4.20: Device frequency response in the $S - L$ plane, based on hot-wire measurements.

resonance frequency and finally it goes down towards low values, for which the formation criterion is not satisfied, [83].

Finally, a LEM model is tailored on the experimental data. A single sub-array of slots, namely the actuator behaves as a multiple orifice device with four slots communicating with a single cavity driven by one diaphragm alone. Chiatto *et al.* [111], found that a double-orifice actuator, with symmetric configuration and a relatively high distance between the orifices centers, can be considered as divided in two sub-volumes, each of them operating with its own pressure and exit orifice velocity. However, the previous assumption does not apply for the present case, being the slots too close to each other; for this reason, the analytical approach should consider a single cavity volume beneath a sub-array of four slots. The lumped element model described in Chapter 3 has been therefore extended to a multiple-orifice configuration: the one-degree-of-freedom forced-damped spring-mass equation for the diaphragm dynamics remains unchanged (hereafter not reported); the mass conservation inside the cavity and the unsteady Bernoulli's equations at the exit slots have been

properly modified accordingly to the slots number (Eqs. (4.3-4.4)).

$$\frac{V_c}{\gamma p_a} \frac{dp_i}{dt} - A_w \dot{x}_w = - \sum_{i=1}^n A_{s,i} U_i \quad (4.3)$$

$$\ddot{U}_i + \frac{K}{l_{e,i}} |U_i| \dot{U}_i + \omega_{H,i}^2 U_i = \frac{A_w}{A_{o,i}} \omega_{H,i}^2 \dot{x}_w \quad i = 1, \dots, n \quad (4.4)$$

where n is the slots number, $V_c = A_w w_c$ is the cavity volume, A_w is the diaphragm surface area, $A_{s,i}$ is the i -th slot area, γ is the specific heat ratio of air, p_a is the external ambient pressure, p_i represents the cavity (internal) differential pressure and U_i is the instantaneous flow velocity through the orifice, namely the i -th jet velocity. Moreover, $x_w(t)$ is the diaphragm (average) displacement at a generic time instant t , ω_H is the i -th Helmholtz natural frequency, K is the head loss coefficient, $l_{e,i}$ is the distances between the two application points of the Bernoulli's equations for the i -th slot. The prediction of the LEM model are reported in the Stokes-Strouhal ($S - St$) plane, Fig. 4.21, together with previous hot-wire measurements.

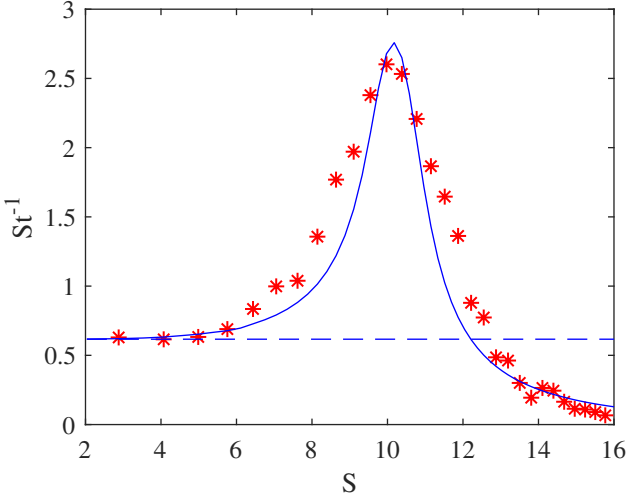


Figure 4.21: Comparison of theoretical LEM (continuous line) and hot-wire measurements (star symbols) frequency responses.

The model agrees quite well with the experimental data, except a slight over prediction around the peak value at the resonance condition. For the

sake of completeness, the corresponding incompressible horizontal straight has been also reported (dashed line). Note that for high frequencies, both experimental and numerical values tends towards very low values, where probably the jet is not forming anymore. The resonance frequency is predicted with a maximum spread of 4% with respect to the experimental data.

Chapter 5

Interaction between synthetic jets and a crossflow

The present chapter deals with the numerical simulation of the flow field generated by the interaction of a synthetic jet actuator and a boundary layer flow. Owing to the transitional behaviour of the flow, the present computational setup constitutes a challenging work, as numerical dissipation and mesh effects strongly affect the repeatability of the results. For this reason, the analysis made use of several numerical tools to get high-fidelity results. In particular, the hexahedral mesh used for the simulations has been obtained using a popular meshing tool, whereas the direct numerical simulations have been carried out using the Nek5000 code. Indeed, as stated in Chapter 2, this code is capable to obtain an accurate description of both averaged and fluctuating characteristics of the jet, even for coarse meshes. For this reason Nek5000 was deemed appropriate for the present numerical setup.

A series of direct numerical simulations has been carried out, in order to investigate the transition to turbulence of the controlled flow for various flow conditions. The actuation frequency, the inlet Reynolds number and the inlet turbulent intensity have been considered in this parametric study. It has been found that the synthetic jet strongly affects the boundary layer development, as shown by the streamwise distributions of the skin friction coefficient and the shape factor. The innovative aspect of this work is that the actuation frequencies are chosen to match the unstable frequency of

the inlet flow (i.e. the frequency of the most amplified Tollmien-Schlichting wave, found using a local stability analysis), instead of employing the well-known virtual aeroshaping effect. The numerical results will show that the streamwise position of the transition region can be anticipated using synthetic jets, which could justify their use to fix the position of transition onset on lifting surfaces.

The chapter is organized as follows. The main results on the application of SJs in laminar and turbulent boundary layers are outlined in Sec. 5.1. In this section various approaches for the choice of the momentum coefficient and the reduced frequency are briefly summarized. Sec. 5.2 concerns the numerical simulations of the synthetic jet in crossflow. Results of the numerical simulations are shown in Sec. 5.3 in terms of instantaneous and time-averaged fields, in order to analyze the flow development downstream of the jet. Comparisons with other flow control techniques and implications for separation control are drawn in Sec. 5.4.

5.1 Background and motivation

Since the introduction of active flow techniques, a special attention has been paid on their application on zero-pressure-gradient boundary layer on a flat plate. Two main reasons drove the researchers to investigate the control of such a flow field: firstly, the controlled flow generated by the actuation on an attached boundary layer can provide insights on the effect of this technique to control lifting surfaces. Several numerical, experimental and theoretical studies have been carried out, aiming to find differences in the turbulence development along the streamwise direction of the plate. Secondly, this configuration constitutes an example of a control of a convectively unstable flow, which has been extensively investigated in literature (see for instance, the review paper of Fabbiane *et al.* [122]). Theoretical works on the active control for the delay of laminar–turbulent transition in boundary layers, handled by means of several strategies, have been made to obtain model-based for the prediction of the controlled flow. The efficiency, the robustness to uncertainties and the performance of such techniques has been also investigated.

On the other hand, the interaction of synthetic jets with a boundary layer has been investigated in detail in several works, both experimentally and via simulations. As a summary, two different philosophies can be followed to design the actuator: the most used one is to obtain the

so-called virtual aeroshaping. This concept has been introduced by Mittal *et al.* [25], who simulated the jet-flow interaction for actuation frequency that are much larger than the characteristic frequency of the flow. They demonstrated that SJs, in this framework, can generate time-averaged recirculation regions that are larger than the actuator diameter, which can be used to introduce a “virtual morphing” of the aerodynamic surfaces. This idea has been subsequently followed by Chatlynne *et al.* [123] for flows around two-dimensional airfoils and by Dandois *et al.* [50] for separation bubbles. Similar studies have been carried out also for plasma SJs by Zong and Kotsonis [124].

The aforementioned works, therefore, gave useful guidelines on the choice of the actuation frequency for a certain control application. Conversely, all the other cited papers mainly focused on the evolution of the hairpin vortices in the far field, the overall topology of the mean and the instantaneous flow fields, the distribution of the skin-friction coefficient on the plate, without linking the flow control parameters to the inherent frequencies of the flow. Therefore, it can be stated that a complete characterization of the receptivity to synthetic jet in boundary layer flows, for different values of C_μ , F^+ and boundary layer Reynolds number, is still lacking. Such a study could be crucial for the advancement of the whole flow control community, from both a physical and modeling perspective. Indeed, on the one hand it could be very interesting to understand which values of the non-dimensional parameters maximize the efficiency in generating hairpin structures. These structures are responsible for an early transition (with respect to the uncontrolled case) and a skin-friction coefficient increase in the streamwise direction.

On the other hand, the present study approaches the problem of realizing a reduced-order modeling of a piezo-driven synthetic jet in crossflow, which should be able to match the LEM output of the SJ in quiescent conditions with the knowledge, via reduced-order modeling, of the spectral characteristics of the field to be controlled. This approach led to the numerical setup chosen in the present investigation: indeed, even if it is necessary to include the orifice into the simulations, it is possible to neglect the cavity, and represent its effect by an oscillating boundary condition at the orifice lower end. The jet velocity at the orifice exit is obtained via existing LEM models for the jet in quiescent conditions, and changes in geometry, actuation frequency and supplied voltage can be easily considered within the LEM formulation. This procedure allows

also to include the compressibility effects of the flow in the cavity and the coupling mechanisms between the diaphragm motion and the fluid flow (Helmholtz resonance).

The present chapter concerns, therefore, the receptivity of synthetic jet actuators in boundary layers over a flat plate. It is worth noting that, in this context, the term *receptivity* must be intended as explained in the original work of Morkovin [125], namely as the internalization of external disturbances into the boundary layer. Direct numerical simulations of the flow field generated by the interaction between the synthetic jet and the crossflow have been carried out. The main aim of the study is to investigate the evolution of the hairpin vortices and their ultimate transition to turbulence, for different values of the actuation frequency and inlet Reynolds number, including an investigation of the flow in presence of freestream turbulence. Differently from the virtual aeroshaping studies, in this case the actuation frequency is next to the characteristic frequency of the crossflow, in order to deepen the understanding of how SJs modify the modes of the uncontrolled flow. The characteristic frequency of the Blasius boundary layer is evaluated via standard linear stability theory. This study constitutes a first brick of a wider project, the realization of a reduced-order model for the design of a synthetic jet to control more complicated crossflows.

5.2 Numerical simulations

5.2.1 Numerical setup

All the numerical simulations have been carried out using Nek5000. A standard setup for transitional flows has been chosen for the present analysis: for all the simulations shown in the present work the polynomial order of the spectral element is $N = 9$. The time integration is based on a third-order splitting method, whereas the linear systems arising from the pressure and the velocity discretizations are solved using, respectively, GMRES and conjugate gradient methods, with tolerances of 10^{-7} and 10^{-9} . The numerical domain is shown in Fig. 5.1: it includes both the external flow field and the jet pipe. All the lengths and the velocities have been made dimensionless against the orifice diameter D and the crossflow velocity U_∞ . The dimension of the external domain are $L_x = 55D$, $L_y = 10D$, $L_z = 10D$, where x denotes the direction of the crossflow, y the direction of the jet and z the spanwise one. It must be highlighted

that the streamwise length of the domain is not long enough to have, in the uncontrolled case, transition to turbulence. As a consequence, any transitional structure detected in the controlled cases must be ascribed to the effect of the synthetic jet.

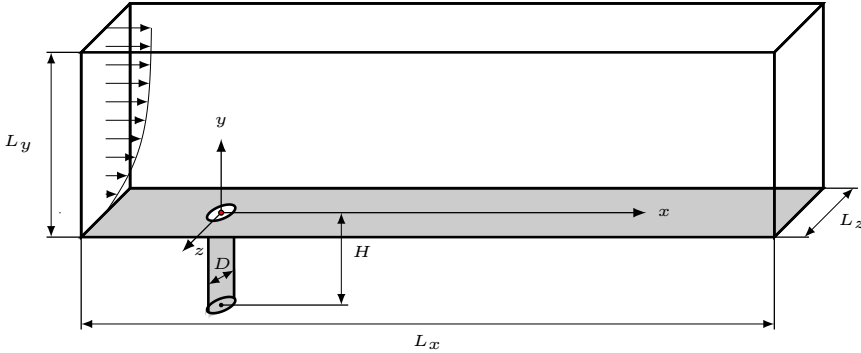


Figure 5.1: Computational domain and main geometrical parameters of the simulations.

The boundary condition at the crossflow inlet, located $10D$ upstream of the jet, has been chosen to mimic a actual boundary layer profile, which can be encountered by the SJ actuator both in wind tunnel experiments and in operating conditions. The boundary condition has been obtained as the superposition of a standard Blasius profile (whose displacement thickness is chosen to have a prescribed value of $Re_{\delta_0^*}$ at the nozzle centerline location) and a freestream turbulence (FST), whose intensity Tu_∞ varies between 0 and 2% in the present simulations. The procedure followed to generate the FST is outlined in the paper by Brandt *et al.* [126]; the FST frequencies and amplitudes are chosen from Von Karman's homogeneous-isotropic turbulence spectrum Eq. (5.1), whereas the FST shape is obtained as a combination of a subset of Orr-Sommerfeld/Squire (OSS) modes. In Eq. (5.1), L is the integral length scale, k the wavenumber.

$$E(k) = \frac{a(kL)^4}{(b(kL)^2)^{17/6}} LTu_\infty^2 \quad (5.1)$$

More details on the procedure and the choice of the model parameters can be found in [126] and citing references. The streamwise distribution of the turbulence intensity at $y = 20\delta_0^*$ is shown in Fig. 5.2, for one of the sim-

ulations involved in the present investigation ($Re_{\delta_0^*} = 550$, $Tu_\infty = 0.02$). It can be observed that the turbulent intensity decreases exponentially from the inlet boundary, as obtained by the aforementioned studies. This finding confirms the validity of the present computational setup.

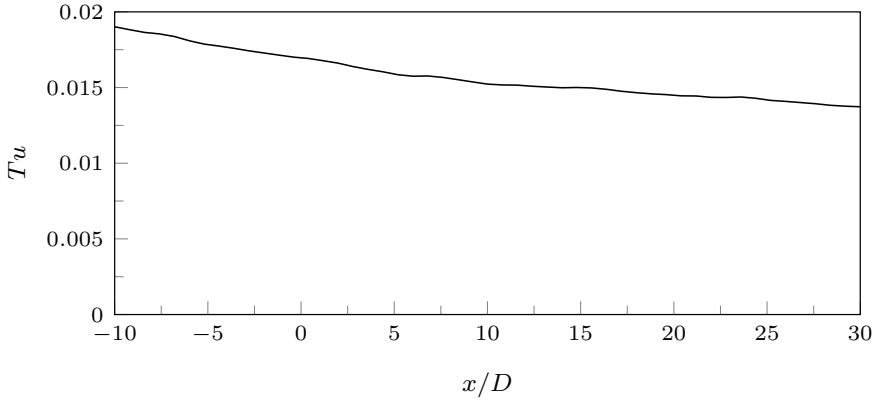


Figure 5.2: Exponential decay of the turbulent intensity Tu along the streamwise direction. Case S6, $y = 20\delta_0^*$.

The inlet condition for the jet is an oscillating Dirichlet condition: the flow is assumed to be laminar at the jet inlet, therefore the jet inlet condition is obtained from Womersley's flow theory, eq. (5.2):

$$\frac{V(r, t)}{U_\infty} = R_j \cdot \text{Real} \left\{ \left[1 - \frac{J_0(i^{3/2}Wo r)}{J_0(i^{3/2}Wo)} \right] e^{i\omega t} \right\}, \quad Wo = \sqrt{\frac{\omega D^2}{4\nu}} \quad (5.2)$$

where J_n is n-th order Bessel function, r the non-dimensional axial distance from the pipe symmetry axis, R_j the velocity ratio between the jet and the crossflow ($R_j = V_{j,max}/U_\infty$), ω the actuation circular frequency and Wo the Womersley number.

The pipe length is chosen large enough to have a fully-developed pulsating jet flow at its lower end; after a preliminary work $H = 5D$ has been chosen. The decision of including the inlet pipe into the simulations derives from a recent literature output: in fact, previous studies on continuous jets in crossflow have shown that it is necessary to include the inflow pipe to correctly obtain the flow field at the orifice exit plane [67, 127, 66].

No-slip conditions have been applied at the plate and on the nozzle boundary, and periodic boundary conditions are enforced at the spanwise

ends $z = \pm L_z/2$. Such a boundary condition is often employed to simulate a synthetic jet array with a reduced computational cost. In this framework L_z is the spanwise spacing between the axis of two consecutive orifices. This distance comes out as an important project parameter of several active and passive flow control systems, as localized roughness elements, micro-vortex generators and fluidic actuators, the latter being exhaustively discussed in Chapter 4, with reference to double-orifice and multi-slotted configurations. Indeed, the control efficiency of an array of actuators is strongly dependent on this distance, being used to modulate the control output in the spanwise direction. However, for $L_z = 10D$ it is possible to neglect the interaction between adjacent jets, at least in the near-field region, as shown in the previous Chapter for double-orifice devices.

A natural outflow boundary condition $-pn + \nu \nabla U \cdot \mathbf{n} = 0$ has been applied at the outlet, while a mixed boundary condition $u = U_\infty$, $v_y = w_y = 0$ is used on the top edge of the boundary layer to allow vertical transpiration of the flow through the outlet boundary.

5.2.2 Flow parameters

As explained in Chapter 1, the characteristics of the controlled flow field depends on the boundary layer Reynolds number at the nozzle centerline station $Re_{\delta_0^*} = U_\infty \delta_0^* / \nu$, the reduced frequency F^+ and the momentum coefficient C_μ . The influence of H/D on the flow behaviour can be omitted as long as the flow is fully developed at the pipe inlet. The non-dimensional parameters chosen in the simulations are summarized in Table 5.1. The crossflow Reynolds number was initially chosen as $Re_{\delta_0^*} = 550$, being slightly above the critical Reynolds number predicted by linear stability theory. This flow condition can be also expressed in terms of local $Re_{x_0} = U_\infty x_0 / \nu$, where x_0 is the virtual position of the nozzle center, thus obtaining $Re_{x_0} \approx 102000$. The ratio between the boundary layer displacement thickness and the pipe diameter is chosen as 0.25 for almost all cases. However, during the present investigation also a smaller value of $Re_{\delta_0^*} = 500$ has been considered; the aim of this computation was to observe how the flow behaves if the Reynolds number is decreased below the linear stability threshold. It is worth noting that variations in the crossflow Reynolds number were obtained by changing δ_0^* , which means, from an experimental point of view, moving the actuator upstream.

The velocity ratio is chosen small enough in order to give a small perturbation on the boundary layer and avoid triggering instability mech-

anisms just downstream of the orifice exit. As regards the reduced frequency, the reference frequency has been obtained by means of spatial, linear stability analyses at the streamwise location of the nozzle centerline (when the jet is off). For each Reynolds number, the value of the circular frequency maximizing the spatial growth rate have been selected, and used as reference frequency. Simulations S1, S3, S5, S6 are performed with $F^+ = 1$, whereas simulations S2 and S4 are performed at $F^+ = 0.5$ and $F^+ = 2$, respectively. Finally, the inlet freestream turbulent intensity is fixed to 0 for S1-S4 simulations; S5 and S6 cases has been devoted to investigate the effect of Tu_∞ on the flow field, by imposing, respectively, $Tu_\infty = 0.01$ and $Tu_\infty = 0.02$. All simulations are summarized in Table 5.1.

Table 5.1: Non-dimensional parameters used in the simulations.

Parameter	Simulation acronym					
	S1	S2	S3	S4	S5	S6
Crossflow Reynolds number, $Re_{\delta_0^*}$	500	550	550	550	550	550
Velocity ratio, R	0.1	0.1	0.1	0.1	0.1	0.1
BL thickness/jet diameter, δ_0^*/D	0.227	0.25	0.25	0.25	0.25	0.25
Jet Reynolds Number, Re_j	220	220	220	220	220	220
Reduced Frequency, F^+	1.0	0.5	1.0	2.0	1.0	1.0
Inlet turbulence intensity, Tu_∞ (%)	0.0	0.0	0.0	0.0	1.0	2.0

5.2.3 Preliminary computations

The chosen computational setup has been validated performing two preliminary computations. A first set of simulations have been carried out to validate the inlet velocity profile of the jet. A three-dimensional simulation of the unforced boundary layer (with a closed nozzle), has been subsequently performed to verify that the unforced case is characterized by a steady solution. The latter computation was required to ensure that the (small) disturbance created by the geometrical discontinuity due to the orifice presence does not lead to instability for the chosen Reynolds number.

As regards the oscillating pipe simulations, two-dimensional axisymmetric computations have been performed, enforcing a top-hat, oscillating velocity profile at the pipe inlet. The velocity profiles, after a development region of small streamwise dimension, converge to the analytical solution

defined by Eq. (5.2), as depicted in Fig. 5.3. The radial coordinate is written as r ; open circles are used to represent the numerical data, whereas continuous lines are employed for the analytical solution. Both the Stokes layer (of order D/Wo) and the central region are very well modelled by the numerical solution.

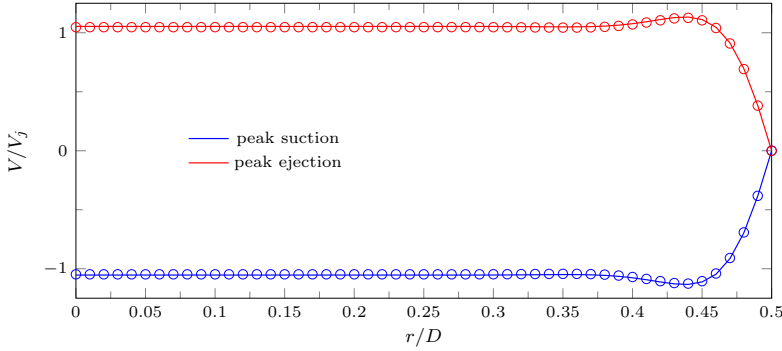


Figure 5.3: Comparison between analytical (continuous line) and numerical (open circles) results of the oscillating pipe flow. $Re_j = 220$, $Wo = 26$.

Furthermore, a preliminary simulation, in which the SJ is off (a no-slip condition is applied at the lower end of the pipe) was carried out. The flow field has been initialized using a standard Blasius solution for the external domain (whereas the velocity pipe is initially null), and the simulation has been performed until a steady state solution was reached. It has been observed the flow field, after a short transient phase, actually attained a steady state, as expected for the present computational setup. The effect of the inlet pipe was confined in the near field only, consisting in a steady, recirculation region of small extension: indeed, the distribution of the skin friction coefficient collapses onto the Blasius solution just downstream of the orifice exit (as shown in Fig. 5.4). This fact assures that the disturbance induced by the nozzle geometry, if no jet is imposed, is not able to make the flow unstable.

5.3 Analysis of the controlled flow field

In this section the results of the investigation are presented in terms of instantaneous and time-averaged velocity fields, for all the configurations introduced in Table 5.1. In particular, case S3, characterized by $Re_{\delta_0^*} =$

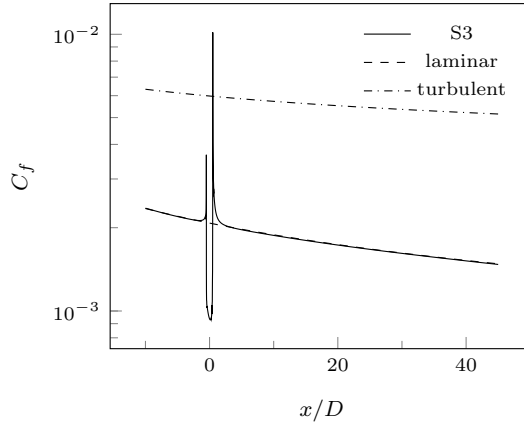


Figure 5.4: Instantaneous distribution of the skin friction coefficient C_f along the streamwise direction in the symmetry plane, SJ off. The laminar (Blasius) solution (dashed lines) and the turbulent correlation $C_f(x) = 0.455/\log^2(0.06Re_x)$ are shown for comparison.

550 and $F^+ = 1$ is considered as the reference case, and is discussed in Sec. 5.3.1. The effects of varying the actuation frequency (cases S2 and S4), the boundary layer Reynolds number (case S1) and the freestream turbulence (cases S5, S6) are investigated, respectively, in Sec. 5.3.2 and 5.3.3 and 5.3.4.

5.3.1 Baseline case ($Re_{\delta_0^*} = 550$, $\omega = \omega_{ref}$)

A view of the vortical structures generated by the interaction between the jet and the boundary layer for case S3 is depicted in Fig. 5.5, through iso-surfaces of the instantaneous λ_2 field [128]. Hairpin vortices are generated at each actuation cycle and advected downstream by the crossflow. The distance between two consecutive vortices in the near field is $\approx 6D$, and which is close to the wavelength predicted by spatial linear stability for the uncontrolled Blasius profile at the jet position. The vortices clearly converge while moving downstream, generating a complex flow field, even if the varicose symmetry of the flow is preserved until the end of the domain. This means that the jet does not excite any sinuous motion in the controlled case, which is possibly related to the small value of C_μ and the low inlet Reynolds number of the boundary layer.

The effect of the synthetic jet on the boundary layer can be investigated

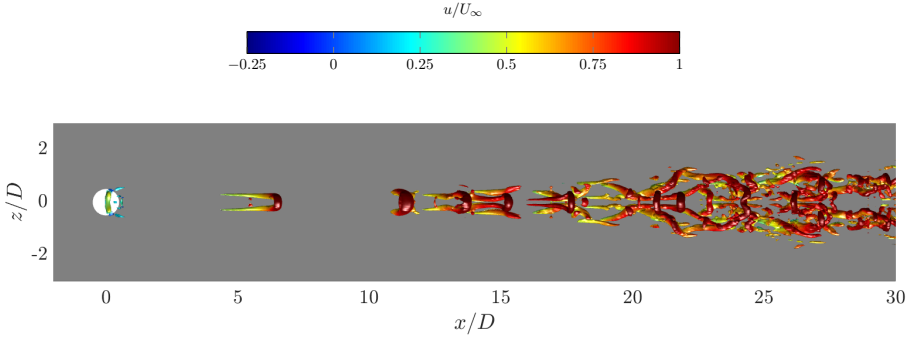


Figure 5.5: Instantaneous view of the vortical structures, highlighted by $\lambda_2 = -0.1$ isosurfaces, and coloured by the instantaneous streamwise velocity. Case S3, tenth cycle, $t/T = 1$ (end of suction phase).

by analyzing the time-averaged flow field. The time-averaged vortical structures are represented in Fig. 5.6, whereas the difference $U_p = \bar{U} - U_B$ between the controlled time-averaged flow field and the corresponding Blasius solution $U_B(x, y)$ is depicted in Fig. 5.7. The latter quantity can be interpreted as the velocity perturbation due to the jet presence. The time-averaged structures include a horseshoe vortex, located upstream the jet, and two streamwise streaks on the leeward side, similarly to low-Reynolds-number continuous jets in crossflow. The action of the vortical structures on the flow is clearly visible by inspecting the U_p contour map, since, for a fixed streamwise stration, two peaks can be detected in its spanwise distribution. The spanwise velocity profile become more complex in the transition region.

The effectiveness of the jet actuation can be observed by inspecting the time-averaged boundary layer integral parameters, namely the displacement thickness $\bar{\delta}^*$, the momentum thickness $\bar{\theta}$ and the shape factor $\bar{H} = \bar{\delta}^*/\bar{\theta}$, which are shown in Fig. 5.8. The effectiveness of the jet can be discussed by looking at the shape factor distribution, since its value for turbulent boundary layers is much lower than the one obtained from Blasius' theory for the laminar profile (≈ 1.4 versus 2.59). For all the streamwise distribution in Fig. 5.8 three main regions can be identified while moving downstream from the orifice exit: a transition region, where all the integral parameters grow much faster than a laminar boundary layer. In a following region their growth rate reduces, whereas in the far field the growth rates of the boundary layer parameters increase again, in-

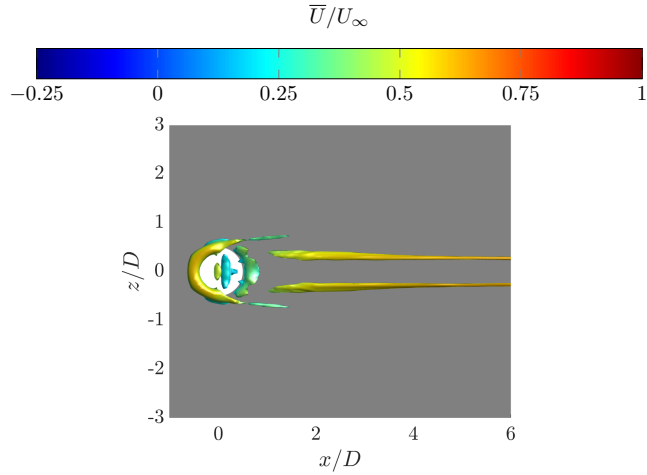


Figure 5.6: Visualization of the time-averaged vortical structures in the near field via $\lambda_2 = -0.01$ isosurfaces, coloured with streamwise time-averaged velocity.

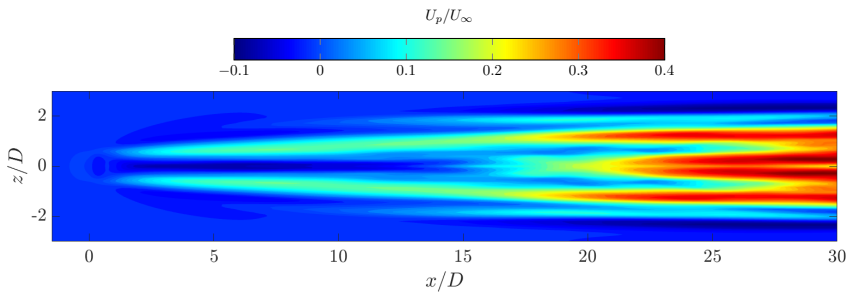


Figure 5.7: Mean streamwise deviation of the controlled flow from the Blasius solution; Case S3, $y/\delta_0^* = 0.8$.

dicating that a turbulent behaviour has been reached. It is worth noting, in fact, that the time-averaged shape factor in the far field is much below the laminar value of 2.6, being comparable with the typical value assumed for turbulent boundary layers of 1.4 (as stated by Schlichting [129]). The same conclusion can be drawn by inspecting the streamwise distribution of the skin friction coefficient, shown in Fig. 5.9. This curve collapse onto the turbulent correlation $\overline{C}_f(x) = 0.455/\log^2(0.06Re_x)$ (cited by White's textbook [130] for turbulent boundary layers), after a transition route from the laminar solutions. It is worthwhile noting that the overshoot in the \overline{C}_f curve is typical of transition due to hairpin vortices. These facts, again,

allow to conclude that a quasi-turbulent state is reached at the end of a domain, therefore the synthetic jet actuator, in this configuration, is able to advance the transition region with respect to the anactuated case.

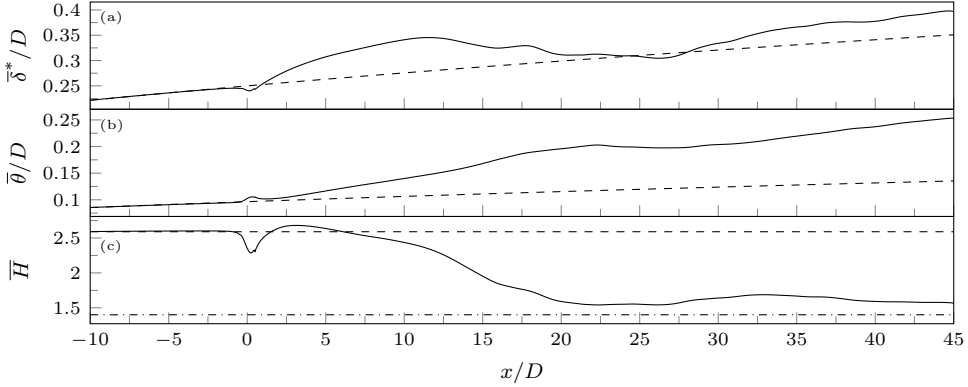


Figure 5.8: Streamwise, time-averaged distributions of the boundary layer integral parameters $\bar{\delta}^*$ (a), $\bar{\theta}$ (b) and \bar{H} (c) in the symmetry plane for Case S3 (continuous line). The laminar solution is depicted with dashed lines for comparison; in (c) also the value $\bar{H} = 1.4$ is shown (dot-dashed line) for reference.

5.3.2 Effect of the actuation frequency

Fig. 5.10 depicts the evolution of the vortex structures in the streamwise direction for Cases S2 and S4.

The topologies of the flow fields are very similar from a qualitative point of view, however two differences can be detected: the spreading rate of the vortices is higher for case S4, whereas the streamwise distance between two consecutive hairpin structures is the smallest (being the biggest for case S2). The effect of the actuation frequency is also clear if time-averaged results are investigated. Fig. 5.11 shows the streamwise distribution of the boundary layer parameters: the strongest deviation from the laminar solution towards a quasi-turbulent flow is observed for the S4 case, which rapidly departs from the laminar solution, as shown by the shape factor diagram. Similar conclusions can be drawn by analyzing the time-averaged distribution of the skin friction coefficient (Fig. 5.12). This finding provides useful information on the capability of the SJ actuation to modify the boundary layer development and enhance its mixing properties.

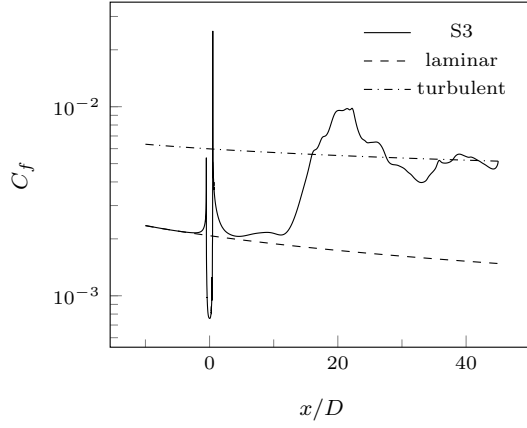


Figure 5.9: Time-averaged distribution of the skin friction coefficient \overline{C}_f along the streamwise direction in the symmetry plane for Case S3. The laminar (Blasius) solution (dashed line) and the turbulent correlation $\overline{C}_f(x) = 0.455/\log^2(0.06Re_x)$ are shown for comparison.

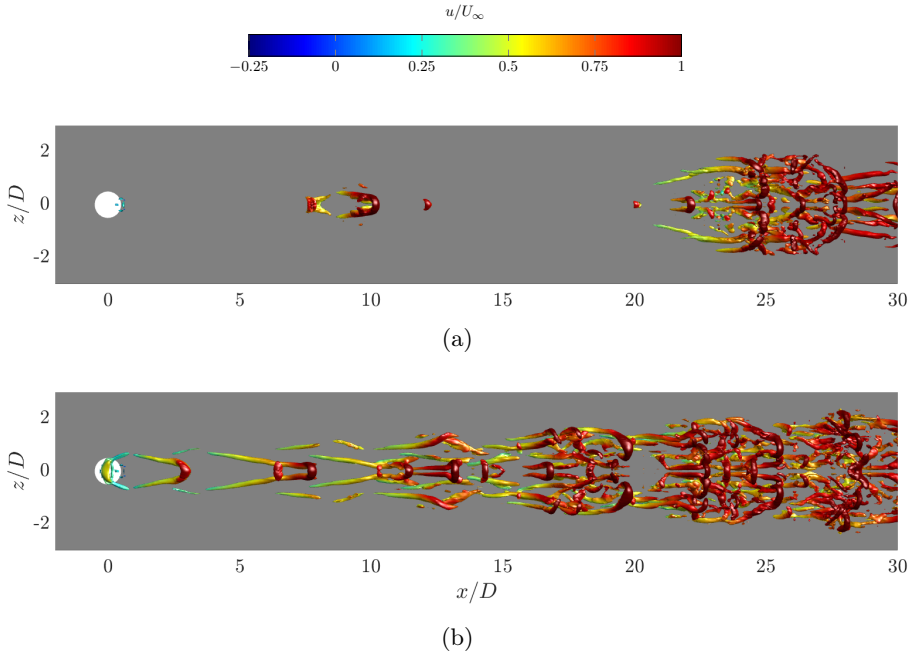


Figure 5.10: Instantaneous view of the vortical structures, highlighted by $\lambda_2 = -0.1$ isosurfaces, and coloured by the instantaneous streamwise velocity. (a) Case S2, (b) case S4, tenth cycle, $t/T = 1$ (end of suction phase).

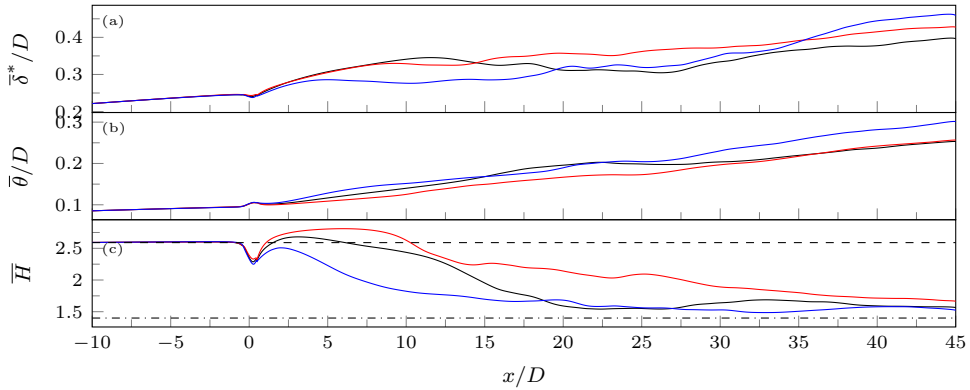


Figure 5.11: Streamwise, time-averaged distribution of the boundary layer integral parameters $\bar{\delta}^*$, $\bar{\theta}$ and \bar{H} in the symmetry plane for Case S2 (red line), S3 (black), S4 (blue). The laminar solution is depicted with dashed lines for comparison; in (c) also the value $\bar{H} = 1.4$ is shown (dot-dashed line) for reference.

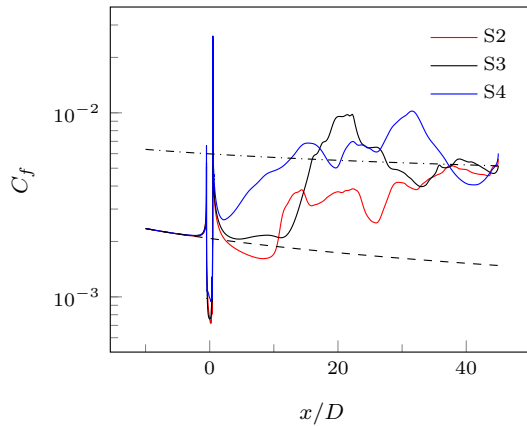


Figure 5.12: Time-averaged distribution of the skin friction coefficient \bar{C}_f along the streamwise direction in the symmetry plane for Case S2 (red line), S3 (black), S4 (blue). The laminar (Blasius) solution (dashed lines) and the turbulent correlation $\bar{C}_f(x) = 0.455 / \log^2(0.06 Re_x)$ are shown for comparison.

5.3.3 Effect of the Reynolds number

Fig. 5.13 depicts the evolution of the vortical structures at the end of the tenth actuation cycle for Cases S1 and S3. It can be seen that reducing the boundary layer Reynolds number below its critical value does not modify the behaviour of the flow. Indeed, the vortical structures are still advected downstream by the crossflow, leading again to a complicated, transitional flow (as shown by the C_f streamwise distribution in Fig. 5.14). The spacing between the vortices, the initial vortex celerity and their spreading rate are slightly different from the baseline case. It can be stated, therefore, that decreasing the Reynolds number below the linear stability threshold (for a Blasius boundary layer) does not change the streamwise development of the flow and its transition to turbulence.

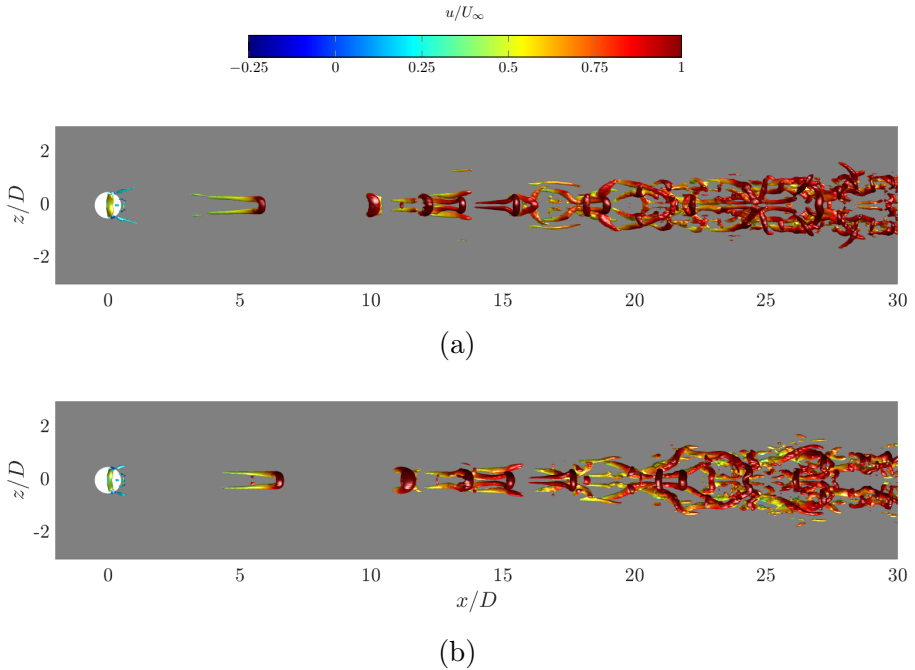


Figure 5.13: Instantaneous view of the vortical structures, highlighted by $\lambda_2 = -0.1$ isosurfaces, and coloured by the instantaneous streamwise velocity. (a) Case S1, (b) case S3, tenth cycle, $t/T = 1$ (end of suction phase).

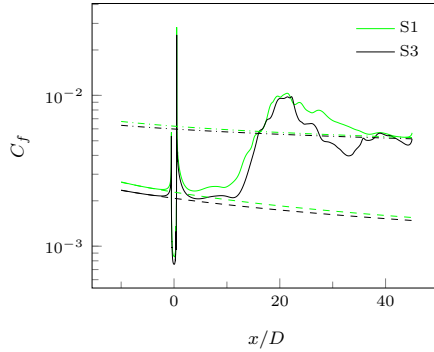


Figure 5.14: Time-averaged distribution of the skin friction coefficient \overline{C}_f along the streamwise direction in the symmetry plane for Case S1 (green line) and S3 (black). The laminar (Blasius) solutions (dashed lines) and the turbulent correlation $\overline{C}_f(x) = 0.455/\log^2(0.06Re_x)$ are shown for comparison.

5.3.4 Effect of the inlet turbulence

An important feature of flow control devices is the robustness to small perturbations of the flow conditions. In the present section the effect of the inlet turbulence on the controlled flow field is investigated. Fig. 5.15 depicts the instantaneous deviation from the Blasius solution for two different values on the inlet turbulence, namely $Tu = 1\%$ and $Tu = 2\%$.

It can be seen that the flow in the near field is practically identical to the one obtained for case S3, both in the hairpin spacings and spreading rate. Conversely, the far-field behaviour is slightly modified by the perturbations, as symmetry-breaking motions appear. Time-averaged integral parameters (not shown herein) reveal that the transitional behaviour of the controlled flow seems to be unaffected by the presence of such perturbations, which means that SJ actuation could be a robust technique to deal with perturbed boundary layers.

5.4 Implication for flow control

The flow field topology generated by the jet-boundary layer interaction perfectly resembles the unsteady flow field generated by an isolated cylindrical roughness immersed in a boundary layer flow. The reader can compare, for instance, Fig. 5.5 with the numerical campaign carried out by Bucci *et al.* [70] for similar crossflow conditions. It is well known nowadays

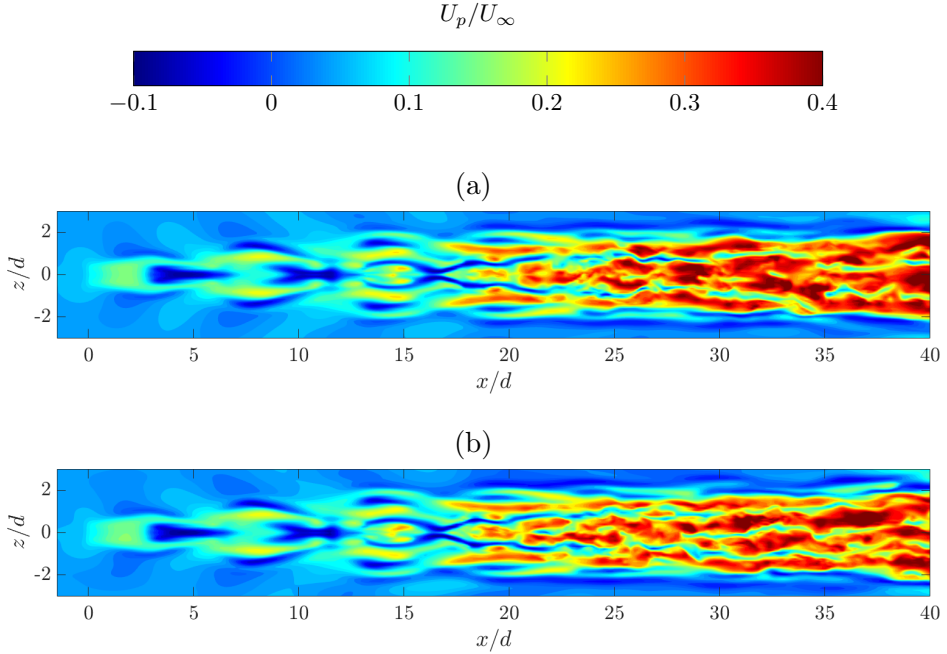


Figure 5.15: Contour map of the instantaneous streamwise deviation of the controlled flow from the Blasius solution; (a) Case S5, (b) case S6, $y/\delta_0^* = 0.8$, tenth cycle, $t/T = 1$ (end of suction phase).

that roughness elements are able to produce streamwise streaks, which, if stable, attenuate the growth of the Tollmien-Schlichting waves and, as a consequence, delay the transition to turbulence. Nonetheless, in many practical situations the streaks generated by the cylindrical element can be unstable themselves, leading to self-sustained hairpin structures and, as a consequence, early transition to turbulence. This result is also well known in literature, for instance by Klebanoff and Tidstrom [131], indeed roughness elements are often used as passive flow control devices to promote transition.

From a flow control perspective, however, the performances of such devices drop in off-design conditions. Indeed, passive flow control devices generally work properly only within a small range of boundary layer Reynolds numbers. Moreover, as shown in Bucci *et al.*, the flow field generated by roughness elements is dramatically modified by small changes in boundary layer inflow conditions. Synthetic jet actuators, on the contrary,

can assure good performances in a wider range of freestream conditions, owing to their flexibility and wide actuation frequency range. In particular, the actuation frequency and applied voltages can be changed during their operation in order to handle different crossflow conditions. The former parameter can be used to modify both the momentum coefficient and the velocity ratio of the control device (since, as shown in Chapter 3, the jet exit velocity and the actuation frequency are interrelated). Moreover, SJ actuators are found to be more robust to inlet perturbances.

In conclusion, the present analysis shows that low-speed SJ actuators can be used as a reliable technique to fix the location of the transition onset on a lifting surface, which is of crucial importance in many industrial applications. Indeed, an increased resistance to separation of the velocity profiles behind the jet exit (which is typically investigated, in the aeronautic field, in terms of reductions of the shape factor H) is achieved for all the controlled cases. This result could partially justify the good performances of synthetic jets in separation control applications, where early transition is often used to reduce the extent of separated regions (as explained in Chapter 1). Their application could be preferred to passive flow control devices, since changes in the BL characteristics can be tackled by changing the actuation frequency and the applied voltage on-the-fly. In particular, in the neighbourhood of the TS characteristic frequency the effect of F^+ seems to be monotonic with the actuation frequency; further analyses must be carried out to find the optimal frequency which maximizes the control efficiency of the device. Once an optimal value of the reduced frequency has been found, a LEM approach can be used to design the proper actuator for the chosen application (for instance, the turbulence control on a wing): the designed actuator, in particular, must fulfil the jet formation criterion shown in Chapter 3, and its cavity volume must be small enough to comply with the available space within the airframe of the vehicle. Finally, as explained in Chapter 4, synthetic jet arrays or multi-orifice actuators should be used in this case, to obtain a homogeneous control along the spanwise direction.

Chapter 6

Conclusions and future work

The present work has been devoted to refine existing models for the design of synthetic jet actuators, to characterize multiple-orifice devices for separation control applications and to investigate the receptivity of a boundary layer to synthetic jet actuation. The research aims at providing a rational procedure for the implementation of piezo-driven and plasma synthetic jet actuators in aerospace and automotive systems. The entire implementation process has been considered, starting from their preliminary design of the device, its manufacturing, its (computational or experimental) characterization, and finally the prediction of the actuator performances in operating conditions. The activity was focused on the control of the transition onset in wall-bounded external flows. However, it can be stated that the present approach, as a principle, could be used to handle different problems, including transition delay on lifting surfaces, mixing enhancement and impinging jets. Moreover, piezo-driven and plasma synthetic jets has been selected as basic technologies for this work, but the results in Chapter 5 can be extended to other AFC systems, including new-generation SJ actuators and pulsed jets.

A major original result obtained in the present work is the fair correspondence between the vortical structures generated by the jet-boundary layer interaction and the one detected in other active and passive systems (as localized roughness and MVGs). Indeed, this fact confirms that low-speed jets could be a promising technique to control transition to turbulence also for low values of the actuation frequency, and provides a alternative approach to the aeroshaping effect for the design of the device. Moreover, low-speed jets can be used in place of passive flow control de-

vices, due to their higher flexibility, robustness to external perturbations and possibility of in-flight corrections.

An important ‘message’ enclosed in this work is that special care must be taken in the simulations of active flow control systems: the application of AFC devices often leads to transitional or turbulent flows, which must be tackled using appropriate computational setups and numerical spatial and temporal schemes. An exhaustive study of the best practises to obtain high-fidelity computational results has been therefore carried out, taking into account both efficiency-to-cost considerations and investigating the parallel performances of the chosen numerical code. It has been obtained that high-order research codes clearly outperforms commercial and multi-purpose codes in all these fields, nonetheless codes based on low-order discretization schemes can be safely used if time-averaged fields are required.

A huge amount of work can be carried out in order to extend the present project. As regards synthetic jets in crossflow, energy methods can be used to gain insights in the ultimate transition to turbulence of the controlled boundary layer, in order to clarify the role of the TS-like waves and the streamwise streaks detected in the time-averaged flow fields. The range of investigated Reynolds number must be increased, in order to understand the influence of the jet position on the flow development. The present investigation allows to state that the jet is effective in advancing the transition region even below the value of $Re_{\delta_0^*}$ predicted by the linear stability position.

An extensive comparison between various active flow control conditions, including synthetic, continuous and pulsed jets, passive turbulators and moving surfaces could be carried out to evaluating the efficiency of such techniques in the hairpin formation. Finally, model reduction techniques and/or global stability analyses will be used to create a reduced-order model of the controlled system. The continuous increase in the available computational power of supercomputers and the recent effort in the numerical modeling of instabilities will allow in a show time to carry out Floquet analyses of three-dimensional flows (where the base flow is assumed to be periodic in time). Such a technique will be groundbreaking in the understanding of pulsed flow fields.

From a computational point of view, it could be interesting to provide more guidelines about the best numerical setup to be used to properly simulate the in-cavity behaviour of the flow. It has been observed that

all simulations are strongly dependent on the inlet condition of the jet, therefore the effects of the compressibility within the orifice neck, of the moving diaphragm and the actuator geometry should be properly taken into account. The same activity should be made also for continuous jets, where the injection strategy deeply modifies the behaviour of the external flows: TriGlobal stability analyses could be performed to properly address this issue. Finally, simulations of plasma synthetic jets in crossflow should be made, and compared with previous experimental results: as for piezo-driven actuators, in a first stage the computations can take advantage of the lumped element model to simplify the computational setup.

Appendix A

The role of critical layer in channel flow stability

The concept of critical layer and its role in the channel flow instability have been widely discussed within the fluid-dynamic stability community. While it was originally conceived as a mathematical technique for the stability investigation of wall-bounded flows (as, for instance, in Tollmien's work [132]), an interesting result, belonging to the energy-based stability analysis, sharply strengthened its physical importance. Indeed, Stuart [133] attempted to explain the generation of the Tollmien-Schlichting waves in channel flows with the aid of the Reynolds-Orr equation. He found that, for a given eigenmode ϕ of the Orr-Sommerfeld operator, it is possible to define a function, $S(z) = (\phi \mathcal{D}\phi^* - \phi^* \mathcal{D}\phi) i/2$ (where \mathcal{D} is used for the wall-normal differentiation and $(\cdot)^*$ for the complex conjugate), which completely characterizes the wall-normal distribution of the production term. The distribution of $S(z)$ function, therefore, can be used to find the flow region which is more effective in the instability process. Indeed, Stuart noted that, if the most unstable mode is introduced into the definition of $S(z)$, this function peaks in the neighbourhood of the critical level (i.e. where the base flow velocity equals the perturbation wave speed), as shown in Fig. A.1.

This result has led to a new critical layer definition, namely the region of flow where viscosity plays an important role in the instability process, and gave birth to a long-standing research line. Indeed, many researchers have tried to quantitatively connect the existence of this region with the generation of Tollmien-Schlichting waves. A few examples of critical-layer-

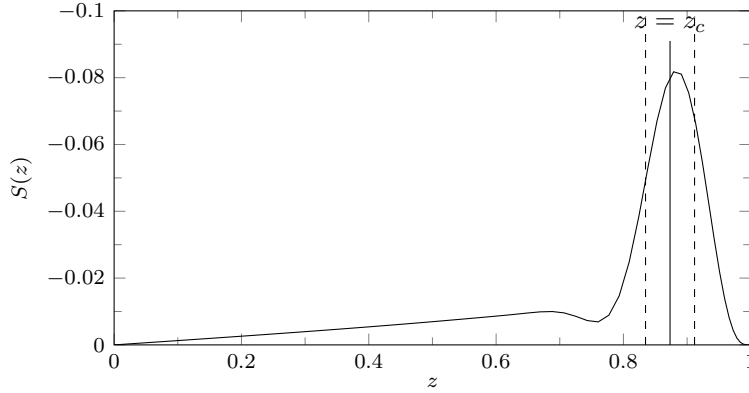


Figure A.1: Distribution of the Stuart function S along the wall-normal z axis for the unstable eigenmode of the OS operator applied to the channel flow instability; $\alpha = 1$, $Re = 10000$. The continuous vertical line corresponds to the critical elevation, while the two dashed lines define the critical layer width.

based models can be found in Baines *et al.*'s work [134] for the Blasius boundary layer, and in Palumbo *et al.* [135] paper for channel and pipe flow stability. Using a simplified linear velocity profile, the former paper first obtained the viscous modes (associated with critical layer structures), finding that these modes are always stable; then these authors proposed a resonance mechanism in which an inviscid disturbance forces the viscous response in place of the no-slip condition at the wall.

The pseudo two-phase model for channel flow instability by Palumbo *et al.* [135] is briefly described in the following. The instability is interpreted in terms of a pseudo two-phase model of the channel, where perturbances are treated as viscous in the wall region, whereas an inviscid model governs their dynamic in the central part of the domain. A fictitious interface is located among them, which is crucial for the interaction between the viscous and the central modes of the channel. The pseudo two-phase model is derived from the so-called Core-Annular Flow (CAF) model, studied by several research groups during the last decades. Such a flow field has been extensively used to explain instability phenomena arising in pipelines. Relevant instability studies of this topic are the works by Orazzo *et al.* [136], and, more recently, by Salin and Talon [137].

Two models have been obtained, starting from the CAF, to separately investigate channel and pipe flow stability. In this Appendix only the

channel one is presented, which is basically a plane version of the CAF: it consists in a two-fluid flow of two immiscible fluids, each one governed by different stability equations. A schematic view of the model is shown in Fig. A.2. The Orr-Sommerfeld equation or one of its asymptotic approximations are enforced within the wall region (which includes the critical layer), such that the viscous behaviour of the flow in the critical layer is correctly captured. On the other hand, the Rayleigh equation is applied in the central region, as the disturbances are treated as inviscid. The governing equations for the wall region, from the Orr-Sommerfeld model to its lowest-order asymptotic expansion (Airy's equation), are summarized in Eqs. (A.1)

$$(\bar{U} - c) (\phi'' - \alpha^2 \phi) - \bar{U}'' \phi = \frac{1}{i\alpha Re} (\phi^{IV} - 2\alpha^2 \phi'' + \alpha^4 \phi) \quad (\text{A.1a})$$

$$(\bar{U} - c) (\phi'' - \alpha^2 \phi) - \bar{U}'' \phi = \frac{1}{i\alpha Re} (\phi^{IV} - 2\alpha^2 \phi'') \quad (\text{A.1b})$$

$$(\bar{U} - c) \phi'' - \bar{U}'' \phi = \frac{1}{i\alpha Re} \phi^{IV} \quad (\text{A.1c})$$

$$(\bar{U} - c) \phi'' = \frac{1}{i\alpha Re} \phi^{IV} \quad (\text{A.1d})$$

whereas the Rayleigh equation is reported in Eq. (A.2)

$$(\bar{U} - c) (\phi'' - \alpha^2 \phi) - \bar{U}'' \phi = 0, \quad (\text{A.2})$$

where $\phi(z)$ is the streamfunction perturbation eigenfunction, $\bar{U}(z)$ the base flow velocity profile (with z being the normal-to-wall spatial coordinate), c the complex eigenvalue, α the dimensionless perturbation wavenumber, Re the Reynolds number, defined in this case in terms of the channel half-height, h , and the maximum base velocity (which lies on the channel symmetry plane).

From a historical perspective, it must be remembered that the asymptotic approximations of orders ε^0 and ε^1 of the OS operator were introduced to correct the inviscid solution in the neighbourhood of the critical elevation. These models, if applied along the entire channel height, always predict a stable behaviour of the flow, as it could be expected since they only include viscous effects. The present model, however, shows that even these approximate operators, if properly adapted, can predict the instability at moderate Reynolds numbers.

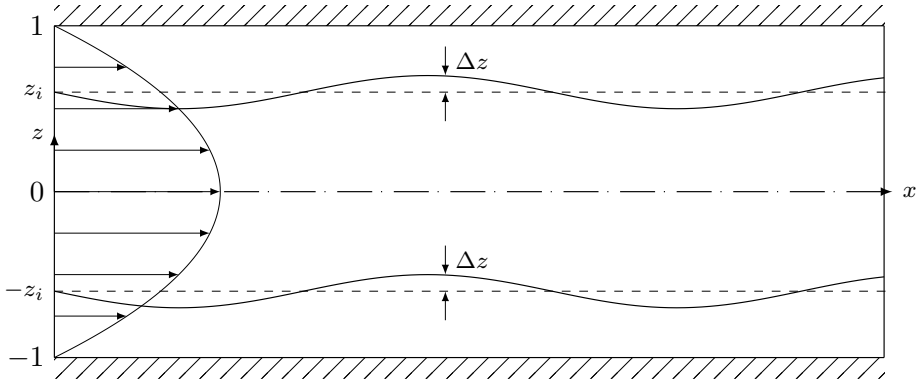


Figure A.2: Sketch of the two-fluid perturbed channel flow, with a generic elevation z_i of the fictitious interface. Even (sinuous) perturbation.

The present analysis is focused only on the even (sinuous) modes of the spectrum (as the most unstable one is sinuous) then only the upper half-channel is analyzed. The wall region and central one are matched through appropriate interface conditions: the continuity of the streamwise velocity perturbation, compatibility conditions and continuity of the pressure field, which read

$$w'_w(z_i) = w'_c(z_i) \quad (\text{A.3a})$$

$$u'_w(z_i) = u'_c(z_i) \quad (\text{A.3b})$$

$$\sigma'_w(z_i) = \sigma'_c(z_i) \quad (\text{A.3c})$$

$$\frac{D\Delta z}{Dt} = w'_{c,w}(z_i) \quad (\text{A.3d})$$

where σ' is the normal stress disturbance at the interface, Δz the interface disturbance amplitude and the subscripts $(\cdot)_w$ and $(\cdot)_c$ are used, respectively, to indicate quantities belonging to the wall and the central sides, respectively. Under the parallel flow assumption, and after enforcing the normal mode ansatz, Eqs. (A.3) can be rearranged. The normal mode

ansatz is introduced in Eqs (A.4)

$$\begin{Bmatrix} u'_{w,c}(x, z, t) \\ w'_{w,c}(x, z, t) \\ \sigma'_{w,c}(x, z, t) \\ \psi_{w,c}(x, z, t) \\ \Delta z(x, t) \end{Bmatrix} = \begin{Bmatrix} \hat{u}_{w,c}(z) \\ \hat{w}_{w,c}(z) \\ \hat{\sigma}_{w,c}(z) \\ \phi_{w,c}(z) \\ \delta \end{Bmatrix} e^{i\alpha(x-ct)} \quad (\text{A.4})$$

whereas the resulting boundary conditions, arising from Eqs. (A.3), are summarized in Eqs. (A.5), in terms of the streamfunction perturbation eigenmodes ϕ and the interface oscillation amplitude δ . Note that only 4 of the 5 equations in Eqs. (A.3) are linearly independent, for this reason the continuity of the wall-normal velocity perturbation has not been enforced (as it is implicitly satisfied if the kinematic condition is imposed).

$$\phi'_w(z_i) = \phi'_c(z_i) \quad (\text{A.5a})$$

$$\phi'''_w(z_i) - 3\alpha^2 \phi'_w(z_i) = 0 \quad (\text{A.5b})$$

$$(\bar{U}(z_i) - c)\delta = -\phi_{c,w}(z_i) \quad (\text{A.5c})$$

The equation system, formed by the governing operators in the wall and the central region, and equipped with the aforementioned boundary conditions, has been solved employing a Chebyshev collocation method in MATLAB environment. The two subdomains $[z_i, 1]$ and $[0, z_i]$ are mapped into the interval $[-1, 1]$, and boundary conditions are implemented in the numerical mode by replacing the extremal rows and columns of the resulting matrix for each subdomain. It is worth noting that the choice of the interface unperturbed height crucially influences the accuracy of the results, since an interface too close to the wall leads to unphysical results. The sensitivity of the model to z_i is shown in the complete paper by Palumbo *et al.* [135]. It can be stated that the optimal position of the interface for all the considered wall approximations of the OS equation is around the position where the base flow velocity is equal to its mean value, namely $z_i = 0.577$.

This velocity value is also approached by the Schensted branch of the OS spectrum for the Poiseuille flow (for $c_i \rightarrow -\infty$), as shown in Fig. A.3. This correspondence is not surprising, since this branch divides the Airy modes of the spectrum (which are wall modes, namely they have a non-vanishing behaviour next to the walls) from the Pekeris one, which is composed of central modes. The reader can find more information about the structure of the temporal spectrum of the OS operator on the seminal work by Mack *et al.* [138]. Finally, no slip conditions are applied at the wall, and a symmetry condition is enforced at the channel axis.

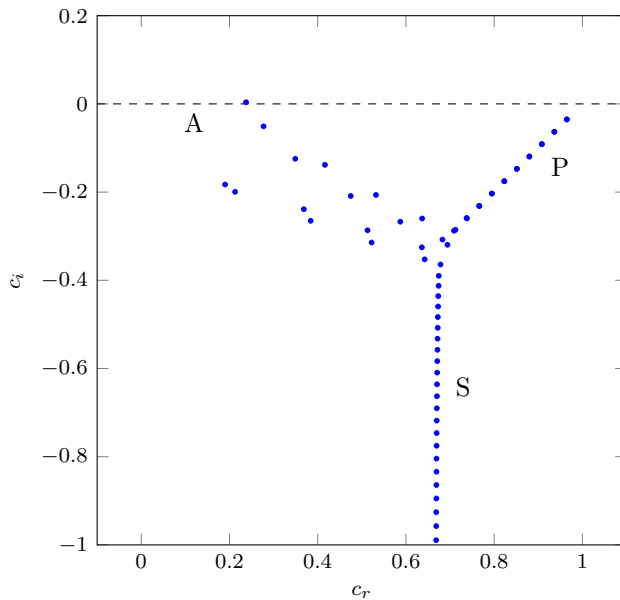


Figure A.3: Orr-Sommerfeld spectrum for channel flow, $\alpha = 1$, $\beta = 0$, $Re = 10000$. 121 Chebyshev points have been used to discretize the normal direction. The Airy (A), Pekeris (P) and Schensted (S) branches are highlighted, following Mack’s work [138].

Some results from the pseudo two-phase mode model are summarized in Fig. A.4 and Table A.1. Fig. A.4 compares the ‘exact’ marginal stability curve (obtained by the complete OS operator) and the output of the pseudo two-phase model. A fair agreement on both the critical Reynolds number and the shape of the marginal curve has been obtained if the OS equation or its highest order approximation are used for the wall re-

gion, whereas a 10% error in the critical Reynolds number is obtained for the ε^1 /Rayleigh approximation. Conversely, the Airy/Rayleigh model is found to be not appropriate to describe the instability of the system, as it predicts instability for every value of Re and α . It is worth noting that the existence of a marginal curve for all cases (except the ε^0 /Rayleigh one) demonstrates that both unstable and stable cases can be obtained by means of this model. Indeed, the same decomposition correctly predicts also the behaviour of pipe flows (not shown herein), which are unconditionally stable, according to the linear theory.

Table A.1: Critical Reynolds number, and corresponding α and c_r values.

Wall region	Inner region	Re_c	α_c	c_r
ε^0	Rayleigh	unstable	–	–
ε^1	Rayleigh	5275	1.11	0.266
ε^2	Rayleigh	5777	1.02	0.264
Orr-Sommerfeld	Rayleigh	5783	1.02	0.264
complete	–	5772	1.02	0.264

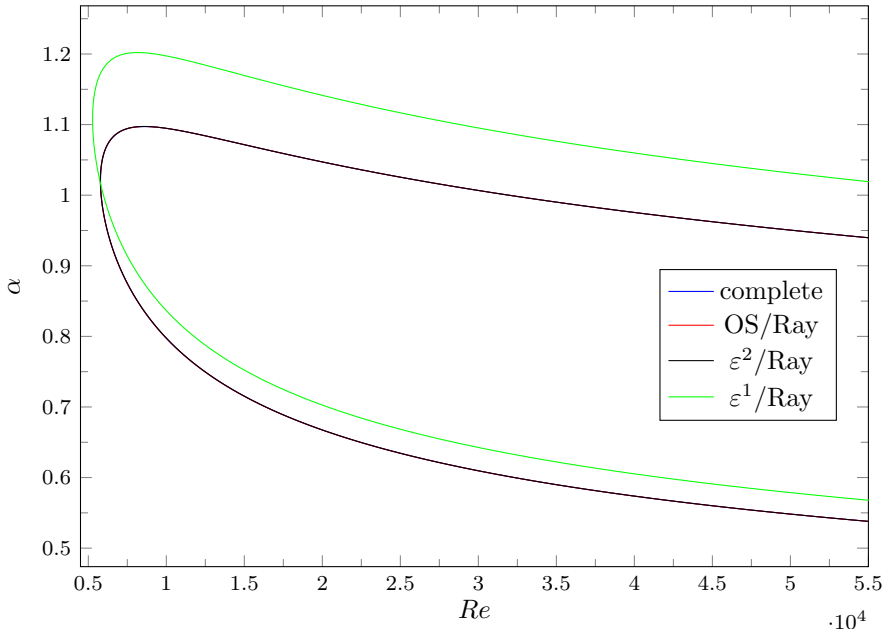


Figure A.4: Marginal stability curve for different wall models.

The most significant result of this analysis is the recognition of two characteristic length scales, which also persist in the turbulent state. The first one is related to the critical layer, and it is of the order of $Re^{-1/3}$, as predicted by the linear theory. However, a second reference length has come out from this investigation. Indeed, while the mechanism leading to instability is located near the wall in the critical layer region, the central region around the flow average velocity (i.e., the outer length scale is of order $\mathcal{O}(h)$) is also deeply involved in the interaction between the central, inviscid zone, and the wall one. This feature is in close agreement with the wall functions driving the full turbulent profile in the nonlinear stage, found by means of the resolvent analysis. The findings arising from the present model could lead to the introduction of a new flow control approach for wall-bounded flows. Indeed, while the study of Baines *et al.* suggests to use compliant walls to modify the no-slip condition at the wall and to suppress instability, the present investigation implies to modify the central region of the channel (around the station where the base flow velocity is equal to $2/3U_{max}$) to counter the instability.

Bibliography

- [1] European Environmental Agency and Eurocontrol. *European Aviation Environmental Report*. 2019.
- [2] CleanSky2 web page. *Web page: <http://www.cleansky.eu>*, 2020.
- [3] P.F. Fischer, J.W. Lottes, and S.G. Kerkemeier. Nek5000 web page. *Web page: <http://nek5000.mcs.anl.gov>*, 2008.
- [4] C. Braud, D. Heitz, G. Arroyo, L. Perret, J. Delville, and J.-P. Bonnet. Low-dimensional analysis, using POD, for two mixing layer–wake interactions. *International journal of heat and fluid flow*, 25(3):351–363, 2004.
- [5] I.H. Abbott and A.E. Von Doenhoff. *Theory of wing sections: including a summary of airfoil data*. Dover Publications, 1959.
- [6] J. Katz. Aerodynamics of race cars. *Annu. Rev. Fluid Mech.*, 38:27–63, 2006.
- [7] S. Ali, C. Habchi, S. Menanteau, T. Lemenand, and J.-L. Harion. Heat transfer and mixing enhancement by free elastic flaps oscillation. *International Journal of Heat and Mass Transfer*, 85:250–264, 2015.
- [8] L. Prandtl. Über flüssigkeitsbewegung bei sehr kleiner reibung. *Verhandl. III, Internat. Math.-Kong., Heidelberg, Teubner, Leipzig, 1904*, pages 484–491, 1904.
- [9] L. Prandtl. The mechanics of viscous fluids. *Aerodynamic theory*, 3:155–162, 1935.

- [10] J.L. Gilarranz, L.W. Traub, and O.K. Rediniotis. A new class of synthetic jet actuators—part II: application to flow separation control. *Journal of fluids engineering*, 127(2):377–387, 2005.
- [11] D. Hlevca, P. Gilliéron, and F. Grasso. Experimental study of the active control applied to the flow past a backward facing ramp. *Experiments in Fluids*, 59(3):39, 2018.
- [12] P. Sujar-Garrido, N. Benard, E. Moreau, and J.P. Bonnet. Dielectric barrier discharge plasma actuator to control turbulent flow downstream of a backward-facing step. *Experiments in Fluids*, 56(4):70, 2015.
- [13] C. Rethmel, J. Little, K. Takashima, A. Sinha, I. Adamovich, and M. Samimy. Flow separation control over an airfoil with nanosecond pulse driven DBD plasma actuators. In *49th AIAA aerospace sciences meeting including the new horizons forum and aerospace exposition*, page 487, 2011.
- [14] M. Gad-el Hak, A. Pollard, and J.-P. Bonnet. *Flow control: fundamentals and practices*, volume 53. Springer Science & Business Media, 2003.
- [15] M.V. Morkovin. Transition in open flow systems—a reassessment. *Bull. Am. Phys. Soc.*, 39:1882, 1994.
- [16] D. Greenblatt and I.J. Wygnanski. The control of flow separation by periodic excitation. *Progress in aerospace Sciences*, 36(7):487–545, 2000.
- [17] G.B. Schubauer and H.K. Skramstad. Laminar-boundary-layer oscillations and transition on a flat plate. naca tech. Technical report, Note, 1948.
- [18] K. Ahuja, R. Whipkey, and G. Jones. Control of turbulent boundary layer flows by sound. In *8th Aeroacoustics Conference*, page 726, 1983.
- [19] K. Ahuja and R. Burrin. Control of flow separation by sound. In *9th Aeroacoustics Conference*, page 2298, 1984.

- [20] P. Krogmann, E. Stanewsky, and P. Thiede. Effects of suction on shock/boundary-layer interaction and shock-induced separation. *Journal of aircraft*, 22(1):37–42, 1985.
- [21] A. Seifert, S. Eliahu, D. Greenblatt, and I. Wygnanski. Use of piezoelectric actuators for airfoil separation control. *AIAA journal*, 36(8):1535–1537, 1998.
- [22] V.J. Modi, J.L.C. Sun, T. Akutsu, P. Lake, K. McMillan, P.G. Swinton, and D. Mullins. Moving-surface boundary-layer control for aircraft operation at high incidence. *Journal of Aircraft*, 18(11):963–968, 1981.
- [23] J. Favier, A. Dauplain, D. Basso, and A. Bottaro. Passive separation control using a self-adaptive hairy coating. *Journal of Fluid Mechanics*, 627:451–483, 2009.
- [24] L.N. Cattafesta III and Sheplak M. Actuators for active flow control. *Annu. Rev. Fluid Mech.*, 43:247–272, 2010.
- [25] R. Mittal and P. Rampunggoon. On the virtual aeroshaping effect of synthetic jets. *Physics of Fluids*, 14(4):1533–1536, 2002.
- [26] K. Grossman, C. Bohdan, and D. VanWie. Sparkjet actuators for flow control. In *41st aerospace sciences meeting and exhibit*, page 57, 2003.
- [27] M. Arena, M. Chiatto, F. Amoroso, R. Pecora, and L. de Luca. Feasibility studies for the installation of plasma synthetic jet actuators on the skin of a morphing wing flap. In *Active and Passive Smart Structures and Integrated Systems XII*, volume 10595, page 105950M. International Society for Optics and Photonics, 2018.
- [28] J. Li and X. Zhang. Active flow control for supersonic aircraft: A novel hybrid synthetic jet actuator. *Sensors and Actuators A: Physical*, 302:111770, 2020.
- [29] G. Chen, G. Krishan, Y. Yang, L. Tang, and B. Mace. Numerical investigation of synthetic jets driven by thermoacoustic standing waves. *International Journal of Heat and Mass Transfer*, 146:118859, 2020.

- [30] B.L. Smith and A. Glezer. The formation and the evolution of synthetic jets. *Physics of Fluids*, 10:2281–2297, 1998.
- [31] A. Hussain and W.C. Reynolds. The mechanics of an organized wave in turbulent shear flow. *Journal of Fluid Mechanics*, 41(2):241–258, 1970.
- [32] A.E. von Doenhoff and A.L. Braslow. The effect of distributed surface roughness on laminar flow. In *Boundary layer and flow control*, pages 657–681. Elsevier, 1961.
- [33] A. Barbagallo, D. Sipp, and P.J. Schmid. Closed-loop control of an open cavity flow using reduced-order models. *Journal of Fluid Mechanics*, 641:1–50, 2009.
- [34] O. Semeraro, S. Bagheri, L. Brandt, and D.S. Henningson. Transition delay in a boundary layer flow using active control. *Journal of Fluid Mechanics*, 731:288–311, 2013.
- [35] D.K. Puckert and U. Rist. Experiments on critical Reynolds number and global instability in roughness-induced laminar–turbulent transition. *Journal of Fluid Mechanics*, 844:878–904, 2018.
- [36] S. Camarri. Flow control design inspired by linear stability analysis. *Acta Mechanica*, 226(4):979–1010, 2015.
- [37] O. Marquet, D. Sipp, and L. Jacquin. Sensitivity analysis and passive control of cylinder flow. *Journal of Fluid Mechanics*, 615:221–252, 2008.
- [38] P.J. Strykowski and K.R. Sreenivasan. On the formation and suppression of vortex ‘shedding’ at low Reynolds numbers. *Journal of Fluid Mechanics*, 218:71–107, 1990.
- [39] P.J. Schmid and D.S. Henningson. *Stability and transition in shear flows*. Springer Science & Business Media, 2012.
- [40] L. Kral, J.F. Donovan, A.B. Cain, and A.W. Cary. Numerical simulation of synthetic jet actuators. *AIAA paper*, 1824:1997, 1997.
- [41] D.P. Rizzetta, M.R. Visbal, and M.J. Stanek. Numerical investigation of synthetic-jet flow fields. *AIAA Journal*, 37(8), 1999.

- [42] C.L. Rumsey, T.B. Gatski, W.L. Sellers, V.N. Vatsa, and S.A. Viken. Summary of the 2004 computational fluid dynamics validation workshop on synthetic jets. *AIAA Journal*, 44(2):194, 2006.
- [43] R.B. Kotapati, R. Mittal, and L.N. Cattafesta III. Numerical study of a transitional synthetic jet in quiescent external flow. *Journal of Fluid Mechanics*, 581:287–321, 2007.
- [44] C.Y. Lee and D.B. Goldstein. Two-dimensional synthetic jet simulation. *AIAA Journal*, 40(3):510–516, 2002.
- [45] S. Menon and J.H. Soo. Simulation of vortex dynamics in three-dimensional synthetic and free jets using the large-eddy lattice Boltzmann method. *Journal of Turbulence*, 5(32):1–4, 2004.
- [46] S Carpy and R Manceau. Turbulence modelling of statistically periodic flows: synthetic jet into quiescent air. *International Journal of Heat and Fluid Flow*, 27(5):756–767, 2006.
- [47] J. Cui and R.K. Agarwal. Three-dimensional computation of a synthetic jet in quiescent air. *AIAA journal*, 44(12):2846, 2006.
- [48] E. Arad, M. Ramasamy, and J.S. Wilson. Flow response of active flow control actuators. *AIAA journal*, 52(5):998–1009, 2014.
- [49] H. Mu, Q. Yan, W. Wei, and P.E. Sullivan. Synthetic jet performance for different axisymmetric cavities analyzed with three-dimensional lattice-Boltzmann method. *AIAA Journal*, 56(6):2499–2505, 2018.
- [50] J. Dandois, E. Garnier, and P. Sagaut. Numerical simulation of active separation control by a synthetic jet. *Journal of Fluid Mechanics*, 574:25–58, 2007.
- [51] S.H. Kim and C. Kim. Separation control on NACA23012 using synthetic jet. *Aerospace Science and Technology*, 13(4-5):172–182, 2009.
- [52] J. Zhou and S. Zhong. Coherent structures produced by the interaction between synthetic jets and a laminar boundary layer and their surface shear stress patterns. *Computers & Fluids*, 39(8):1296–1313, 2010.

- [53] O. Sahni, J. Wood, K.E. Jansen, and M. Amitay. Three-dimensional interactions between a finite-span synthetic jet and a crossflow. *Journal of Fluid Mechanics*, 671:254–287, 2011.
- [54] S. Lardeau and M.A. Leschziner. The interaction of round synthetic jets with a turbulent boundary layer separating from a rounded ramp. *Journal of fluid mechanics*, 683:172–211, 2011.
- [55] X. Wen and H. Tang. On hairpin vortices induced by circular synthetic jets in laminar and turbulent boundary layers. *Computers & Fluids*, 95:1–18, 2014.
- [56] K.E. Jansen, M. Rasquin, J.A. Farnsworth, N. Rathay, M.C. Monastero, and M. Amitay. Interaction of a synthetic jet with separated flow over a vertical tail. *AIAA Journal*, 56(7):2653–2668, 2018.
- [57] J.H. Seo, F. Cadieux, R. Mittal, E. Deem, and L. Cattafesta. Effect of synthetic jet modulation schemes on the reduction of a laminar separation bubble. *Physical Review Fluids*, 3(3):033901, 2018.
- [58] R. Belanger, D.W. Zingg, and P. Lavoie. Vortex structure of a synthetic jet issuing into a turbulent boundary layer from a finite-span rectangular orifice. In *AIAA Scitech 2020 Forum*, page 1815, 2020.
- [59] <http://www.openfoam.org>.
- [60] A.T. Patera. A spectral element method for fluid dynamics: laminar flow in a channel expansion. *Journal of computational Physics*, 54(3):468–488, 1984.
- [61] SU² web page. *Web page*: <http://su2code.github.io/>, 2020.
- [62] T.D. Economou, F. Palacios, S.R. Copeland, T.W. Lukaczyk, and J.J. Alonso. SU2: An open-source suite for multiphysics simulation and design. *Aiaa Journal*, 54(3):828–846, 2015.
- [63] Gerris web page. *Web page*: <http://gfs.sourceforge.net/>, 2020.
- [64] Basilisk web page. *Web page*: <http://basilisk.fr/>, 2020.
- [65] <http://www.nektar.info/>.

- [66] M. Brynjell-Rahkola, A. Hanifi, and D.S. Henningson. On the stability of a Blasius boundary layer subject to localised suction. *Journal of Fluid Mechanics*, 871:717–741, 2019.
- [67] A. Peplinski, P. Schlatter, and D. S. Henningson. Global stability and optimal perturbation for a jet in cross-flow. *European Journal of Mechanics-B/Fluids*, 49:438–447, 2015.
- [68] E. Ezhova, C. Cenedese, and L. Brandt. Interaction between a vertical turbulent jet and a thermocline. *Journal of Physical Oceanography*, 46(11):3415–3437, 2016.
- [69] J.-C. Loiseau, J.-C. Robinet, S. Cherubini, and E. Leriche. Investigation of the roughness-induced transition: global stability analyses and direct numerical simulations. *Journal of Fluid Mechanics*, 760:175–211, 2014.
- [70] M.A. Bucci, D.K. Puckert, C. Andriano, J.-C. Loiseau, S. Cherubini, J.-C. Robinet, and U. Rist. Roughness-induced transition by quasi-resonance of a varicose global mode. *Journal of Fluid Mechanics*, 836:167–191, 2018.
- [71] L. Siconolfi, S. Camarri, and J. Fransson. Stability analysis of boundary layers controlled by miniature vortex generators. *Journal of Fluid Mechanics*, 784:596–618, 2015.
- [72] F. Capuano, A. Palumbo, and L. de Luca. Comparative study of spectral-element and finite-volume solvers for direct numerical simulation of synthetic jets. *Computers & Fluids*, 179:228–237, 2019.
- [73] M.A. Sprague, M. Churchfield, A. Purkayastha, P. Moriarty, and S. Lee. A comparison of Nek5000 and OpenFOAM for the DNS of turbulent channel flow. In *Presentation at Nek5000 Users Meeting*, 2010.
- [74] G.L. Kooij, M.A. Botchev, E. Frederix, B.J. Geurts, S. Horn, D. Lohse, E.P. van der Poel, O. Shishkina, R. Stevens, and R. Verzicco. Comparison of computational codes for direct numerical simulations of turbulent Rayleigh–Bénard convection. *Computers & Fluids*, 166:1–8, 2018.

- [75] C.S. Yao, F.J. Chen, and D. Neuhart. Synthetic jet flowfield database for computational fluid dynamics validation. *AIAA Journal*, 44(12):3153–3157, 2006.
- [76] <http://www.hpc.cineca.it/hardware/marconi>.
- [77] M. Chiatto, F. Capuano, G. Coppola, and L. De Luca. LEM characterization of synthetic jet actuators driven by piezoelectric element: A review. *Sensors (Switzerland)*, 17(6):1–31, 2017.
- [78] H. Zong, M. Chiatto, M. Kotsonis, and L. de Luca. Plasma synthetic jet actuators for active flow control. In *Actuators*, volume 7, page 77. Multidisciplinary Digital Publishing Institute, 2018.
- [79] M. Chiatto and L. de Luca. Numerical and experimental frequency response of plasma synthetic jet actuators. In *55th AIAA Aerospace Sciences Meeting*, page 1884, 2017.
- [80] M. Chiatto, A. Palumbo, and L. de Luca. A calibrated lumped element model for the prediction of psj actuator efficiency performance. *Actuators*, 7(1):1–11, 2018.
- [81] H. Zong, Y. Wu, H. Song, and M. Jia. Efficiency characteristic of plasma synthetic jet actuator driven by pulsed direct-current discharge. *AIAA Journal*, pages 3409–3420, 2016.
- [82] H. Zong, Y. Wu, Y. Li, H. Song, Z. Zhang, and M. Jia. Analytic model and frequency characteristics of plasma synthetic jet actuator. *Physics of Fluids*, 27:1–21, 2015.
- [83] R. Holman, Y. Utturkar, R. Mittal, B.L. Smith, and L. Cattafesta. Formation criterion for synthetic jets. *AIAA journal*, 43(10):2110–2116, 2005.
- [84] V. Timchenko, J. Reizes, E. Leonardi, and G. De Vahl Davis. A criterion for the formation of micro synthetic jets. In *American Society of Mechanical Engineers, Fluids Engineering Division (Publication) FED*, volume 260, pages 197–203, 2004.
- [85] I.M. Milanovic and K.B. Zaman. Synthetic jets in cross-flow. *AIAA journal*, 43(5):929–940, 2005.

- [86] Z. Trávníček, Z. Broučková, and J. Kordík. Formation criterion for axisymmetric synthetic jets at high Stokes numbers. *AIAA Journal*, 50(9):2012–2017, 2012.
- [87] Z. Broučková, P. Šafařík, and Z. Trávníček. A parameter map of synthetic jet regimes based on the Reynolds and Stokes numbers: Commentary on the article by Rimasauskiene et al. *Mechanical Systems and Signal Processing*, 68-69:620–623, 2016.
- [88] R.N. Sharma. Fluid-dynamic-based analytical model for synthetic jet actuation. *AIAA Journal*, 45:1841–1847, 2007.
- [89] Q. Gallas, R. Holman, T. Nishida, B. Carroll, M. Sheplak, and L. Cattafesta. Lumped element modeling of piezoelectric-driven synthetic jet actuators. *AIAA Journal*, 41:240–247, 2003.
- [90] B.L. Smith and G.W. Swift. A comparison between synthetic jets and continuous jets. *Experiments in fluids*, 34(4):467–472, 2003.
- [91] G. Krishnan and K. Mohseni. An experimental and analytical investigation of rectangular synthetic jets. *Journal of Fluids Engineering*, 131(12):121101, 2009.
- [92] M. Chaudhari, B. Puranik, and A. Agrawal. Heat transfer characteristics of synthetic jet impingement cooling. *Int. J. Heat and Mass Transfer*, 53:1057–1069, 2010.
- [93] L.D. Mangate and M.B. Chaudhari. Experimental study on heat transfer characteristics of a heat sink with multiple-orifice synthetic jet. *International Journal of Heat and Mass Transfer*, 103:1181–1190, 2016.
- [94] M.A. Feero, P. Lavoie, and P.E. Sullivan. Influence of cavity shape on synthetic jet performance. *Sensors and Actuators A: Physical*, 223:1–10, 2015.
- [95] J. Kordík and Z. Trávníček. Optimal diameter of nozzles of synthetic jet actuators based on electrodynamic transducers. *Experimental Thermal and Fluid Science*, 86:281 – 294, 2017.
- [96] J.C.R. Hunt, A.A. Wray, and P. Moin. Eddies, streams, and convergence zones in turbulent flows. In *Proceedings of the CTR Summer Program, Stanford, CA*, 1988.

- [97] S. Lee and Y.A. Hassan. Experimental study of flow structures near the merging point of two parallel plane jets using PIV and POD. *International Journal of Heat and Mass Transfer*, 116:871–888, 2018.
- [98] E. Tanaka. The interference of two-dimensional parallel jets: 1st report, experiments on dual jet. *Bulletin of JSME*, 13(56):272–280, 1970.
- [99] E. Tanaka. The interference of two-dimensional parallel jets: 2nd report, experiments on the combined flow of dual jet. *Bulletin of JSME*, 17(109):920–927, 1974.
- [100] T. Okamoto, M. Yagita, Akira Watanabe, and K. Kawamura. Interaction of twin turbulent circular jet. *Bulletin of JSME*, 28(238):617–622, 1985.
- [101] D.R. Miller and E.W. Comings. Force-momentum fields in a dual-jet flow. *Journal of Fluid Mechanics*, 7(2):237–256, 1960.
- [102] Y.F. Lin and M.J. Sheu. Investigation of two plane parallel unventilated jets. *Experiments in Fluids*, 10(1):17–22, 1990.
- [103] A. Laban, S.S. Aleyasin, M.F. Tachie, and M. Koupriyanov. Experimental investigation of nozzle spacing effects on characteristics of round twin free jets. *Journal of Fluids Engineering*, 141(7):071201, 2019.
- [104] R.N. Oskouie, M.F. Tachie, and B.-C. Wang. Effect of nozzle spacing on turbulent interaction of low-aspect-ratio twin rectangular jets. *Flow, Turbulence and Combustion*, pages 1–22, 2019.
- [105] E.A. Anderson and R.E. Spall. Experimental and numerical investigation of two-dimensional parallel jets. *Journal of Fluids Engineering*, 123(2):401–406, 2001.
- [106] B. Zang and T.H. New. On the wake-like vortical arrangement and behaviour associated with twin jets in close proximity. *Experimental Thermal and Fluid Science*, 69:127–140, 2015.
- [107] S.S. Aleyasin and M.F. Tachie. Statistical properties and structural analysis of three-dimensional twin round jets due to variation in

- reynolds number. *International Journal of Heat and Fluid Flow*, 76:215–230, 2019.
- [108] M. Watson, A. J. Jaworski, and N.J. Wood. A study of synthetic jets from rectangular and dual-circular orifices. *Aeronautical Journal*, 107(1073):427–434, 2003.
- [109] M. Watson, A. J. Jaworski, and N. J. Wood. Contribution to the understanding of flow interactions between multiple synthetic jets. *AIAA journal*, 41(4):747–749, 2003.
- [110] H. Riazi and N.A. Ahmed. Numerical investigation on two-orifice synthetic jet actuators of varying orifice spacing and diameter. In *29th AIAA Applied Aerodynamics Conference 2011*, 2011.
- [111] M. Chiatto, F. Capuano, and L. de Luca. Numerical and experimental characterization of a double-orifice synthetic jet actuator. *Meccanica*, 53(11-12):2883–2896, 2018.
- [112] B.L. Smith and A. Glezer. Vectoring of adjacent synthetic jets. *AIAA journal*, 43(10):2117–2124, 2005.
- [113] Z. Luo, Z. Xia, and B. Liu. New generation of synthetic jet actuators. *AIAA Journal*, 44:2418–2419, 2006.
- [114] S. Alimohammadi, E. Fanning, T. Persoons, and D.B. Murray. Characterization of flow vectoring phenomenon in adjacent synthetic jets using CFD and PIV. *Computers & Fluids*, 140:232–246, 2016.
- [115] H. Li, N.K. Anand, and Y.A. Hassan. Computational study of turbulent flow interaction between twin rectangular jets. *International Journal of Heat and Mass Transfer*, 119:752–767, 2018.
- [116] H. Li, N.K. Anand, Y.A. Hassan, and T. Nguyen. Large eddy simulations of the turbulent flows of twin parallel jets. *International Journal of Heat and Mass Transfer*, 129:1263–1273, 2019.
- [117] T. Van Buren and M. Amitay. Comparison between finite-span steady and synthetic jets issued into a quiescent fluid. *Experimental Thermal and Fluid Science*, 75:16–24, 2016.

- [118] M. Jabbal, S. Liddle, J. Potts, and W. Crowther. Development of design methodology for synthetic jet actuator array for flow separation control applications. *Proceedings of the Institution of Mechanical Engineers Part G Journal of Aerospace Engineering*, 227:110–124, 01 2013.
- [119] E. McGlynn, S. Tran, and O. Sahni. Large eddy simulation of flow interactions of segmented synthetic jets on an airfoil. In *47th AIAA Fluid Dynamics Conference*, page 3310, 2017.
- [120] L. Wang, L. Feng, J. Wang, and T. Li. Parameter influence on the evolution of low-aspect-ratio rectangular synthetic jets. *Journal of Visualization*, 21(1):105–115, 2018.
- [121] S. Yavuzkurt. A guide to uncertainty analysis of hot-wire data. *Journal of Fluids Engineering, Transactions of the ASME*, 106(2):181–186, 1984.
- [122] N. Fabbiane, O. Semeraro, S. Bagheri, and D.S. Henningson. Adaptive and model-based control theory applied to convectively unstable flows. *Applied Mechanics Reviews*, 66(6):060801, 2014.
- [123] E. Chatlynne, N. Rumigny, M. Amitay, and A. Glezer. Virtual aero-shaping of a clark-Y airfoil using synthetic jet actuators. In *39th Aerospace Sciences Meeting and Exhibit*, page 732, 2001.
- [124] H. Zong and M. Kotsonis. Effect of velocity ratio on the interaction between plasma synthetic jets and turbulent cross-flow. *Journal of Fluid Mechanics*, 865:928–962, 2019.
- [125] M.V. Morkovin. Critical evaluation of transition from laminar to turbulent shear layers with emphasis on hypersonically traveling bodies. Technical report, AFFDL-TR-68-149, 1969.
- [126] L. Brandt, P. Schlatter, and D.S. Henningson. Transition in boundary layers subject to free-stream turbulence. *Journal of Fluid Mechanics*, 517:167–198, 2004.
- [127] P.S. Iyer and K. Mahesh. A numerical study of shear layer characteristics of low-speed transverse jets. *J. Fluid Mech.*, 790:275–307, 2016.

- [128] J. Jeong and F. Hussain. On the identification of a vortex. *Journal of Fluid Mechanics*, 285:69–94, 1995.
- [129] H. Schlichting and K. Gersten. *Boundary-layer theory*. Springer, 2016.
- [130] F.M. White. *Viscous fluid flow*, volume 3. McGraw-Hill New York, 2006.
- [131] P.S. Klebanoff and K.D. Tidstrom. Mechanism by which a two-dimensional roughness element induces boundary-layer transition. *Physics of Fluids*, 15(7):1173–1188, 1972.
- [132] Walter Tollmien. The production of turbulence. Technical Report NACA-TM-609, 1931.
- [133] J.T. Stuart. *Hydrodynamic stability*. in: Laminar boundary layers, ed. L. Rosenhead, Oxford Clarendon Press, 1963.
- [134] P.G. Baines, S.J. Majumdar, and H. Mitsudera. The mechanics of the Tollmien-Schlichting wave. *Journal of Fluid Mechanics*, 312:107–124, 1996.
- [135] A. Palumbo, M. Chiatto, and L. de Luca. The role of the critical layer in the channel flow transition revisited. *Meccanica*, 54(14):2169–2182, 2019.
- [136] A. Orazzo, G. Coppola, and L. de Luca. Disturbance energy growth in core–annular flow. *Journal of Fluid Mechanics*, 747:44–72, 2014.
- [137] D. Salin and L. Talon. Revisiting the linear stability analysis and absolute—convective transition of two fluid core annular flow. *Journal of Fluid Mechanics*, 865:743–761, 2019.
- [138] L.M. Mack. A numerical study of the temporal eigenvalue spectrum of the Blasius boundary layer. *Journal of Fluid Mechanics*, 73(3):497–520, 1976.